High intensity laser–plasma interactions and their potential for exploring strong-field QED

Inaugural-Dissertation

zur Erlangung des Doktorgrades
der Mathematisch-Naturwissenschaftlichen Fakultät
der Heinrich-Heine-Universität Düsseldorf

vorgelegt von

Christoph Thomas Baumann
aus Mainz

Düsseldorf, März 2020

aus dem Institut für Theoretische Physik I
der Heinrich-Heine-Universität Düsseldorf

Gedruckt mit Genehmigung der
Mathematisch-Naturwissenschaftlichen Fakultät der
Heinrich-Heine-Universität Düsseldorf

Berichterstatter:

1. Prof. Dr. Alexander Pukhov
2. Prof. Dr. Dr. Carsten Müller

Tag der mündlichen Prüfung: 8. Juni 2020

Abstract

The upcoming generation of laser facilities promises extraordinarily strong electromagnetic fields and so opens the door to completely new regimes of light-matter interaction. Special attention is paid on that front to systematic studies on strong-field quantum electrodynamics (QED), where the emergence of a series of novel effects is predicted. Currently, a lot of effort is therefore put into the design of promising experimental campaigns that might be realized in the near future. Plasma, a collective mixture of unbound charges, has gained broad interest in that context, as it offers various opportunities.

The first part of this thesis comprises so-called *QED plasmas* where one is interested in the coupling between collective plasma behavior and QED effects. In particular, the normal radiative-trapping effect is investigated. This effect describes the trapping of radiatively cooled electrons in the nodes of the superimposed electric field transiently formed by two counter-propagating laser pulses. The trapping is subsequently shown to break in sufficiently strong fields due to collective behavior of the generated electron-positron plasma. In a further step, the investigations are generalized to the case of circularly polarized *twisted light*. It is emphasized that the nodes in such configurations form helically-shaped patterns along which electrons can be radiatively trapped. Simultaneously, circularly polarized twisted light is found to enable the laser-driven generation of structured ultra-short (several hundred attoseconds) electron bunches.

The second part of the thesis addresses the conjectured breakdown of perturbative strong-field QED under most extreme conditions. This high-intensity frontier is generally assumed to be far beyond experimental reach due to the ultra-fast radiation loss time of electrons. The thesis is devoted to proving the assumption false by proposing configurations that might allow reaching the fully non-perturbative regime with 100 GeV-class electrons. Three promising setups are introduced in total. These include the collision with a nanometer-sized Mega-Ampere electron beam; an ultra-intense electromagnetic attosecond pulse generated through laser–plasma interaction; and an optical laser pulse whose leading front is cut in the ultra-thin skin layer of a solid-dense plasma. Finally, ways how to identify and differentiate the impact of non-perturbative QED effects from experimentally measured particle spectra are considered.

Zusammenfassung

Die kommende Generation an Laserforschungseinrichtungen verspricht außergewöhnlich starke elektromagnetische Felder und öffnet somit die Tür zu völlig neuen Regimen der Licht-Materie-Wechselwirkung. Besonderes Augenmerk wird dabei auf systematische Studien zur Quantenelektrodynamik (QED) in starken Feldern gelegt, wo das Auftreten einer Reihe neuer Effekte vorausgesagt ist. Deswegen wird momentan viel Aufwand in das Design vielversprechender experimenteller Kampagnen betrieben, die in naher Zukunft realisiert werden könnten. Plasma, ein kollektives Gemisch aus ungebundenen Ladungen, hat in diesem Zusammenhang großes Interesse erlangt, da es verschiedene Möglichkeiten bietet.

Der erste Teil dieser Abschlussarbeit umfasst sogenannte *QED Plasmen*, bei denen man an der Kopplung zwischen kollektivem Plasma-Verhalten und QED-Effekten interessiert ist. Im Speziellen wird der normale Strahlungseinfangeffekt untersucht. Dieser Effekt beschreibt das Einfangen von strahlungsgekühlten Elektronen in den Nullstellen des superponierten elektrischen Feldes, welche durch zwei gegenläufige Laserpulse vorübergehend gebildet werden. Es wird anschließend gezeigt, dass dieses Einfangen in hinreichend starken Feldern aufgrund kollektiven Verhaltens des erzeugten Elektron-Positron-Plasmas zusammenbricht. In einem weiteren Schritt werden die Untersuchungen auf den Fall des zirkular-polarisierten *verdrehten Lichts* verallgemeinert. Es wird hervorgehoben, dass die Nullstellen in solchen Konfigurationen spiralförmige Strukturen bilden, entlang welcher Elektronen strahlungsbedingt gefangen werden können. Gleichzeitig zeigt sich, dass zirkular-polarisiertes verdrehtes Licht die lasergetriebene Erzeugung von strukturierten ultrakurzen (einige hundert Attosekunden) Elektronenbündeln ermöglicht.

Der zweite Teil der Abschlussarbeit adressiert den vermuteten Zusammenbruch der perturbativen Starkfeld-QED unter extremsten Bedingungen. Es wird allgemein geglaubt, dass diese Hochintensitätsgrenze aufgrund der ultraschnellen Strahlungsverlustzeit von Elektronen weit außerhalb des experimentell Möglichen liegt. Die vorliegende Abschlussarbeit ist der Widerlegung dieser Annahme gewidmet, indem Konfigurationen vorgeschlagen werden, die das Erreichen des (völlig) nicht perturbativen Regimes mit 100 GeV Elektronen erlauben könnten. Drei vielversprechende Aufbauten werden insgesamt vorgestellt. Diese beinhalten die Kollision mit einem nanometergroßen Megaampere-Elektronenstrahl; einem ultraintensiven elektromagnetischen Attosekundenpuls, der durch eine Laser-Plasma-Wechselwirkung generiert wird; und einem optischen Laserpuls, dessen vordere Front mittels des Skin-Effektes in einem festkörperdichten Plasma abgeschnitten wird. Abschließend werden Wege durchdacht, wie man den Einfluss nicht perturbativer QED-Effekte aus experimentell gemessenen Teilchenspektren identifizieren und differenzieren kann.

Contents

1 Introduction

With the beginning of the 20th century, Albert Einstein has vastly revolutionized physics. Modern science, but also modern life in general, would not be possible without his brilliant ideas. A simple example is the laser whose guiding principle of stimulated emission of radiation was put forward by Einstein already in 1916 [1]. Though it subsequently took another 40 years for the first laser to be built by Maiman in 1960 [2], lasers quickly became indispensable. This is due to the unique properties provided by their radiation, such as monochromaticity and large coherence, which enable a large variety of uses. For instance, lasers are nowadays standard components in everyday applications such as barcode readers, optical disk drives, printers, medical devices, and many more. Also scientifically, lasers are of major importance for experiments in almost all subdisciplines of physics, including (but not limited to) the formation of a Bose-Einstein condensate which requires laser cooling [3, 4] or the detection of gravitational waves via laser interferometry [5]. Most naturally, however, laser radiation allows studying fundamental light-matter interactions.

Shortly after the first demonstration of a laser, peak intensites of about 10^{10} Wcm^{-2} were available in experiments. The underlying strong fields made it possible to study nonlinear optical effects in atomic systems, resulting in the experimental observation of multiphoton absorption [6] and multiphoton ionization [7]. Moreover, Agostini *et al.* discovered the remarkable effect of above-threshold ionization in the late 1970s [8], where electrons can absorb more photons than necessary in order to be freed from the parent atom. Around the same time, record peak intensities were increased by several orders of magnitude to yield 10^{14-15} Wcm^{-2}. Unfortunately, the progress in achieving higher peak intensities first stagnated at that stage due to damaging the media used for the amplification process.

Only the invention of *chirped pulse amplification* (CPA) by Strickland and Mourou in 1985 [9] solved the obstacle acceptably. Their idea was to first stretch an initially short and relatively weak pulse to become longer. This longer pulse is then amplified in a second step. The stretching has here the advantage that the peak power of the long pulse can be pushed significantly below the damage threshold of the amplifying medium and so does not lead to its demolition. In the last step, the amplified long pulse is again compressed to become short and intense. The CPA technique led to a tremendous increase in record peak intensities in the time since, and simultaneously opened completely new research perspectives.

Constantly growing peak intensities facilitated to go beyond atomic physics in strong fields with the result that broad attention was paid on laser-produced plasmas. In that context, the next fundamental scale to be surpassed was the relativistic one, where electrons reach relativistic velocities ($v \approx c$, where c is the speed of light) due to the interaction with the laser field. The regime is entered at intensities of 10^{18} Wcm^{-2} for optical lasers, which were experimentally available in the mid-1990s. Such relativistic laser–plasma interactions subsequently gained a lot of interest based on the vast number of applications they can be used for. It was suggested by Tajima and Dawson to build laser–plasma accelerators for electrons [10]. There, accelerating electric fields of tens to hundreds GVm^{-1} are achievable [11], which are many orders of magnitude larger than those in conventional accelerators. This obviously allows laser–plasma accelerators to be constructed in a much more compact manner, in this way being particularly interesting from a financial perspective. For instance, the acceleration of electrons up to energies of 8 GeV over cm-scale distances was demonstrated in a recent experiment [12]. Apart from electron acceleration, the interaction of intense laser pulses with solid-dense plasma surfaces can also be used for the generation of high harmonics. Depending on the exact interaction parameters, there are different mechanisms that describe the harmonic generation in detail (see [13] for more information). All regimes, however, provide access to coherent and short-wavelength radiation. This in turn enables the manufacture of attosecond pulses, which have the potential to visualize ultra-fast processes as occurring in atomic and molecular systems with unprecedented temporal resolution [14].

At state-of-the-art research facilities laser–plasma experiments can be performed well above the relativistic threshold, with the possibility of reaching peak intensities up to 2×10^{22} Wcm^{-2} [15, 16]. Correspondingly, the coupled light-matter interaction becomes highly nonlinear and novel phenomena occur. The motion of single electrons in such intense fields, for instance, is still part of active research. This is due to the electron suffering non-negligible radiation losses as a result of the acceleration in the intense field. The back-reaction on the electron is commonly referred to as radiation reaction. Though radiation reaction has been known for a long time in classical electrodynamics [17, 18], its theoretical description from a pure classical perspective still gives rise to a number of inconsistencies, and so is not yet complete. In principle, the inconsistencies can be removed when restricting to the leading-order contribution as found by Landau and Lifschitz [18]. More fundamentally however, they are removed in the more general theory of quantum electrodynamics (QED); but a complete theory is lacking also here as exact expressions can only be given for specific field configurations. The incompleteness of current models is to some extent also reflected in recent experiments performed at the Astra-Gemini laser facility in the United Kingdom. Even though experimental observation of radiation reaction was reported in the collision of an intense laser beam with laser–plasma accelerated electrons [19, 20], neither classical nor QED-based radiation-reaction models did fully explain the measurements in all details. The request for further studies is thus immense, particularly with regard to (planned) facilities like the Extreme Light Infrastructure (ELI) project [21], the Vulcan 10 PW project [22], or the Exawatt Center for Extreme Light Studies (XCELS) [23], where even higher intensities of 10^{23-24} Wcm^{-2} are envisaged. It is beyond question that laser–plasmas in such regimes will be affected by radiation reaction. The more so as radiation reaction can have further impacts on the dynamics than just the direct back-reaction on the electrons. This back-reaction is naturally mediated through the emission of high-energetic photons by the electrons. These photons themselves can *interact* with the strong laser field, potentially leading to their decay into electron-positron pairs. It is exactly these mutual interactions which make laser–plasmas to a promising environment for exploring QED.

The present thesis draws on at this juncture. In particular, it deals with finding configurations in which QED can be investigated by means of laser–plasma interactions. There are rather different ways of how to proceed in that regard. On the one hand, it is possible to directly study the interplay between the main QED effects, namely γ-photon emission and pair production, and the collective plasma behavior. This area is frequently denoted as QED-plasma physics to highlight the interest in the strong coupling. On the other hand, one can also aim at studying QED as a theory itself. One then exploits the laser–plasma interaction in such a way that it helps generating fruitful configurations for QED tests. Both approaches are discussed in the following thesis mostly within the framework of numerical simulations. Eventually, the findings can be relevant for the design of new experiments at the large facilities.

1.1 Outline

The thesis is structured as follows. Chapter 2 starts with an introduction about the theoretical background. It covers general aspects of plasma such as Debye shielding and the dispersion relation for electromagnetic waves. Afterwards, single-electron motion in plane electromagnetic waves is discussed, particularly laying the focus on relativistic intensities. As accelerating charges radiate, it is subsequently addressed when the corresponding radiation losses need to be taken into account. In that regard, chapter 2 finishes with introducing the strong-field QED regime, where novel effects become important like, for instance, γ-photon emission and pair production. Chapter 3 then continues with a comprehensive motivation on the particle-in-cell (PIC) approach used throughout the present thesis for large-scale laser–plasma simulations. It is also explained in that regard how to self-consistently incorporate QED effects into the (classical) PIC scheme. The following main part is divided into the three chapters. In chapter 4 the radiative trapping of electrons in the standing wave of two circularly polarized laser pulses of ultra-high intensity is investigated. Precisely, the studies include the robustness of the trapping effect with increasing laser intensity (see section 4.2), and its behavior with respect to the use of twisted light (see section 4.3). The fully non-perturbative regime of QED, which long has been thought to be out of reach, is addressed in chapter 5. This chapter is divided into three sections. First, it is discussed that the regime can be accessed in the collision of two electron beams with Mega-Ampere currents and nanometer size (see section 5.2). The subsequent sections then explore the feasibility of approaching the regime by means of laser–plasma interactions. In that respect, it is explained how to convert an intense optical laser pulse into an ultra-intense attosecond pulse (see section 5.3), or how to significantly cut the leading front of an ultra-intense optical pulse (see section 5.4). Afterwards, a model for the particle spectra produced in the simulations from chapter 5 is derived in chapter 6. The model purposes at advancing the issue of signatures that allow identifying the fully non-perturbative regime of QED from experimental data. Finally, chapter 7 draws a conclusion.

1.2 Contribution of the author

Chapter 2 is a recapitulation of the literature in order to provide the reader with all information necessary for the understanding of the main results. The same holds for parts of chapter 3, where the numerical PIC method is reviewed. The thesis' author implemented the Monte-Carlo algorithm described in section 3.3.1 (and first published by Elkina *et al.* [24]) into the existing PIC code `VLPL`. Likewise, the author performed the simulations and analysis in to order to verify the correct implementation (see section 3.3.2).

The setup for studying the influence of pair production on the radiative trapping in section 4.2 was conceived by the author. Similarly, the author came up with the idea to study radiative trapping in twisted-light waves. The author performed the simulations and did the data analysis. The simple models in section 4.3 were developed by the author. It was also the author's idea to relate the number of electron patterns to the total angular momentum per laser photon [see equation (4.3.8)].

The concept of the non-perturbative QED collider was suggested by Vitaly Yakimenko (see section 5.2). The proof of concept was supported by PIC simulations with two independent codes. The author conducted `VLPL` simulations (results are given in section 5.2), which were found to be in good agreement with `OSIRIS` simulations performed by Fabrizio Del Gaudio, Thomas Grismayer and Luís O. Silva from the Instituto Superior Técnico in Lisbon, Portugal. For this purpose, the author implemented the field initialization of ultra-relativistic particle beams into `VLPL`. Moreover, the author elaborated the setups proposed in sections 5.3 and 5.4, performed the simulations, and did the data analysis.

In chapter 6, the model to analytically describe the particle spectra was developed by Evgeny Nerush. The author double-checked all the calculations (see also appendix A.3) and performed the simulations.

All figures shown throughout the thesis were produced by the author. It is particularly noted that some previously published figures were reproduced in a slightly different manner to match the thesis design and to avoid copyright infringements. Finally, the entire text was written by the author.

1.3 Publications in peer-review journals

Ideas presented in the thesis at hand have led to the following contributions in peer-review journals:

- C. Baumann and A. Pukhov, *Influence of e^-e^+ creation on the radiative trapping in ultraintense fields of colliding laser pulses*, Physical Review E **94**, 063204 (2016)
- C. Baumann and A. M. Pukhov, *Generation of attosecond electron packets in the interaction of ultraintense Laguerre–Gaussian laser beams with plasma*, Quantum Electronics **47**, 194 (2017)
- C. Baumann and A. Pukhov, *Electron dynamics in twisted light modes of relativistic intensity*, Physics of Plasmas **25**, 083114 (2018)
- V. Yakimenko, S. Meuren, F. Del Gaudio, C. Baumann, A. Fedotov, F. Fiuza, T. Grismayer, M. J. Hogan, A. Pukhov, L. O. Silva, and G. White, *Prospect of Studying Nonperturbative QED with Beam-Beam Collisions*, Physical Review Letters **122**, 190404 (2019)
- C. Baumann, E. N. Nerush, A. Pukhov and I. Yu. Kostyukov, *Probing non-perturbative QED with electron-laser collisions*, Scientific Reports **9**, 9407 (2019)
- C. Baumann and A. Pukhov, *Laser-solid interaction and its potential for probing radiative corrections in strong-field quantum electrodynamics*, Plasma Physics and Controlled Fusion **61**, 074010 (2019)

2 Theoretical background

The following chapter is devoted to giving a comprehensive introduction into the physical framework considered within the thesis at hand. For this purpose, it starts with an introduction on plasma and its characterizing properties (see section 2.1). It follows a discussion about the motion of single electrons in electromagnetic fields of relativistic strength (see section 2.3). The reader is then guided to the question when radiation losses become meaningful and have to be taken care of in the electron dynamics (see section 2.4). The final part introduces the theoretical basics regarding a quantum treatment of radiation losses and the creation of electron-positron pairs. The material presented in the first part of the chapter (see sections 2.1-2.4) is mainly adapted from standard textbooks and reviews about plasma physics [25–27]. Further references are given where needed.

2.1 What is plasma?

In general, plasma is an ionized gas of negatively and positively charged particles. In addition to solids, liquids, and gases, plasma is often referred to as the fourth state of matter. On earth, only a small portion of matter is naturally in the plasma state. This is totally different on astronomical scales, where plasma is assumed to make up more than 99 percent of ordinary matter. Plasma is therefore of great interest for the understanding of the universe. Physically, plasma is characterized by the complex interaction between a vast number of moving charges with their generated electromagnetic fields. These in turn can affect the motion of the charges themselves. In fact, it is that self-consistent interplay which gives rise to collective behavior and which results in unique properties of plasma.

2.1.1 Debye shielding

Though plasma is a mixture of unbound charged particles, it behaves quasineutral on distances that are large with respect to the Debye length. Physically speaking, the quasineutrality means that the plasma shields the electrostatic field of arbitrary charge fluctuations. In order to understand that and to get an expression for the Debye length, one starts with an arbitrary test charge q, which is placed into a homogeneous electron-proton plasma of finite temperature. The presence of the test charge will lead to a redistribution of charged particles inside the plasma. Namely, charged particles with the same sign as q will be repelled, while charged particles with the opposite sign will be attracted by the test charge. The resulting electrostatic potential is determined by Poisson's equation

$$\Delta\phi = -4\pi\Big(q\delta(\mathbf{x}) + e(n_p - n_e)\Big), \tag{2.1.1}$$

where $\delta(\mathbf{x})$ is Dirac's delta function describing the test charge at the origin, e is the elementary charge, and n_e and n_p are the ensued electron and proton density, respectively. In thermodynamic equilibrium, it makes sense to model the electrons in the potential ϕ according to a Boltzmann distribution,

$$n_e = n_0 \exp\left(\frac{e\phi}{k_B\theta_e}\right). \tag{2.1.2}$$

Here, n_0 is the density of the unperturbed plasma, k_B is Boltzmann's constant, and θ_e is the electron temperature. It is further reasonable to assume the ions to be immobile on the typical timescales of laser–plasma interactions. The proton density is thus equal to $n_p = n_0$. Assuming the perturbation induced by the test charge to be small, $e\phi/(k_B\theta_e) \ll 1$, one can readily Taylor expand the exponential in equation (2.1.2) up to linear order in ϕ. Together with the expression for proton density, one can insert the approximated electron density into equation (2.1.1). Eventually, one arrives at

$$\left(\Delta - \frac{1}{\lambda_D^2}\right)\phi = -4\pi q\delta(\mathbf{x}), \tag{2.1.3}$$

with λ_D representing the Debye length defined through

$$\lambda_D = \sqrt{\frac{k_B\theta_e}{4\pi n_0 e^2}}. \tag{2.1.4}$$

Equation (2.1.3) can be easily solved in Fourier space with subsequent back-transformation into real space. In doing so, one finds the potential to be

$$\phi = \frac{q}{r}\exp\left(-\frac{r}{\lambda_D}\right). \tag{2.1.5}$$

On the basis of equation (2.1.5), it is now clear that the potential of a point charge inside a plasma is effectively shielded and falls off much faster than the naked Coulomb potential for $r \gtrsim \lambda_D$. The plasma is thus almost free of large single-particle fields. It is particularly that property that allows the plasma to show collective behavior as the details of charge fluctuations are only important inside the Debye sphere $r \lesssim \lambda_D$. Simultaneously, it means that the plasma dimensions must be large in comparison with the Debye length, $L \gg \lambda_D$. The above derivation, especially the use of the Boltzmann distribution for the electron density, further requires the number of particles participating in the Debye shielding to be large. This is ensured when the number of particles in a sphere with radius λ_D is large, which defines the so-called plasma parameter N_D,

$$N_D = \frac{4}{3}\pi\lambda_D^3 n_0 \gg 1. \tag{2.1.6}$$

The discussion continues with the introduction of the plasma frequency.

2.1.2 Plasma frequency

The plasma was shown to shield local charge fluctuations over spatial scales defined by the Debye length. The plasma frequency describes the corresponding timescale. In particular, it gives the frequency of charge density oscillations induced to maintain the quasineutrality of the plasma. It can easily be obtained with the help of the thermal velocity of the electrons. Non-relativistically, this is defined as

$$v_{\theta_e} = \sqrt{\frac{k_B \theta_e}{m_e}}, \tag{2.1.7}$$

where m_e is the electron mass. The characteristic frequency to balance any charge fluctuation is then given by the ratio of the characteristic electron velocity to the characteristic length,

$$\omega_{pe} = \frac{v_{\theta_e}}{\lambda_D} = \sqrt{\frac{4\pi n_0 e^2}{m_e}}. \tag{2.1.8}$$

As will be shown now, these collective electron oscillations strongly alter the propagation of electromagnetic waves with respect to the vacuum case.

2.2 Propagation of light waves in plasma

As discussed in the preceding section, a plasma can be seen as a heap of freely-moving charged particles. It is clear that an impinging electromagnetic wave leads to a distortion of the plasma. The plasma tries to compensate these local charge fluctuations with the result that the wave drives collective plasma oscillations. These in turn modify the dispersion relation of electromagnetic waves in comparison with the vacuum case. A detailed analysis shows that the dispersion relation of light waves in a background plasma is modified to

$$\omega^2 = \omega_{pe}^2 + c^2 k^2, \tag{2.2.1}$$

where ω is the angular frequency of the light wave, k its wave number and c is the speed of light. Equation (2.2.1) has meaningful consequences. The propagation of light waves through media requires a finite wave number $k > 0$. In a background plasma this will only be possible if the frequency ω_0 of a specific light wave is greater than the electron plasma frequency, $\omega_0 > \omega_{pe}$. This can be understood in a very simple physical picture. If the frequency of light is too large, $\omega_0 > \omega_{pe}$, the plasma electrons cannot respond on the fast timescale determined by the wave. The plasma is therefore only distorted marginally. Consequently, the light wave can propagate into and through the plasma. This changes profoundly for $\omega_0 < \omega_{pe}$. There, electrons can respond almost instantaneously with the result that the light-driven electron currents reflect the incoming light wave. Mathematically, this is encoded in the wave number k becoming imaginary for frequencies below the plasma frequency. The imaginary k leads to an exponentially decreasing wave amplitude, $\propto e^{-x/l_s}$, characterized by the length scale l_s. This characteristic length l_s is also known as skin depth and describes how deep the light wave can penetrate into the plasma. In terms of figures, one finds

$$l_s = \frac{c}{\sqrt{\omega_{pe}^2 - \omega_0^2}} \approx \frac{c}{\omega_{pe}}. \tag{2.2.2}$$

The last approximation often suffices for a rough estimate of the penetration depth in solid-dense targets, whose plasma frequencies are usually much larger than frequencies of optical laser waves.

Recapitulatory one can judge the transparency properties of a plasma by comparing the plasma frequency with the angular frequency of the light wave. In many situations, however, this is unhandy because one first has to evaluate the plasma frequency from the target's electron density, which one typically has on hand. It is thus very common to introduce the so-called critical density n_{cr} as the density up to which a light wave with frequency ω_0 can propagate. It can be calculated by demanding that ω_0 and ω_{pe} coincide at the critical density, which yields the symbolic expression

$$n_{\mathrm{cr}} = \frac{m_e \omega_0^2}{4\pi e^2} = \frac{1.12 \times 10^{21}}{(\lambda_0/\ \mu\mathrm{m})^2}\ \mathrm{cm}^{-3}. \tag{2.2.3}$$

In that notation plasmas with higher/lower densities, $n_e \gtrless n_{\mathrm{cr}}$, are opaque/transparent for light with frequency ω_0. In that sense one often uses the wording over-dense/under-dense plasma targets.

In the case that the light wave is of relativistic strength, electrons quickly reach large Lorentz factors γ_e. This is taken care of when one inserts the dynamical electron mass $\gamma_e m_e$ into the expressions for the plasma frequency and the critical density (2.2.3). In the relativistic case, the same light wave can thus propagate into denser plasmas as a result of the increased inertia of the electrons. When relativistic effects become important is shown in the next section.

2.3 Electron dynamics in electromagnetic waves

The section discusses the motion of electrons in external electromagnetic waves. The first part is restricted to the relatively simple case of plane waves. The second part generalizes the discussion to more realistic situations, where the waves have a transverse profile. In this context, the concept of the so-called ponderomotive force will be introduced.

2.3.1 Plane electromagnetic waves

The motion of single electrons in an external electromagnetic field can be deduced solely from the vector potential $\mathbf{A}$. This can be written as

$$\mathbf{A}(\eta) = \mathrm{Re}\left\{A_0 f(\eta)\, e^{i\eta}\mathbf{e}\right\}, \tag{2.3.1}$$

where $\eta = \omega_0 t - k_0 x$ is the phase of the wave with central frequency ω_0 and wave number $k_0 = \omega_0/c$ that is propagating along the positive x-axis, $f(\eta)$ is an arbitrary shape function that accounts for the finite duration of the wave, A_0 determines the amplitude, and $\mathbf{e}$ is the polarization vector. As known from classical electrodynamics, the polarization vector is perpendicular to the propagation axis of the wave, $\mathbf{e} \perp \hat{\mathbf{e}}_x$. The electron motion in such a configuration is often considered in the Hamilton formalism, which has the advantage that all symmetries of the problem are striking. Relativistically, the corresponding Hamiltonian reads

$$H = m_e c^2 \underbrace{\sqrt{1 + \frac{\left(\mathbf{P} + \frac{e}{c}\mathbf{A}(\eta)\right)^2}{(m_e c)^2}}}_{=\gamma_e}\ . \tag{2.3.2}$$

Here, $\mathbf{P}$ is the canonical momentum of the electron and γ_e its Lorentz factor. One can directly see that the Hamiltonian depends only on $\mathbf{P}$ and η, $H = H(\mathbf{P}, \eta)$, and hence is independent of the transverse coordinates y and z. Consequently, the transverse canonical momentum is a constant of motion and thus conserved during the interaction,

$$\mathbf{P}_\perp = \text{constant}. \tag{2.3.3}$$

The simple dependency of H on η gives another constant of motion, which can be constructed from Hamilton's equations of motion $\mathrm{d}H/\mathrm{d}t = \partial H/\partial t = \omega_0\, \partial H/\partial \eta$ and $\mathrm{d}P_x/\mathrm{d}t = -\partial H/\partial x = k_0\, \partial H/\partial \eta$. Combining the two equations shows readily that

$$H - cP_x = \text{constant}. \tag{2.3.4}$$

Then, equations (2.3.3) and (2.3.4) allow the determination of the electron's kinetic momentum $\mathbf{p} = \mathbf{P} + (e/c)\,\mathbf{A}$ and kinetic energy $E_{\text{kin}} = (\gamma_e - 1)\, m_e c^2$. Under the assumption the electron was at rest before the interaction with the plane wave pulse and noting that the vector potential is transverse, one finds

$$\begin{aligned} \frac{p_x}{m_e c} &= \frac{1}{2}\frac{e^2\mathbf{A}^2}{m_e^2 c^4}, \\ \frac{\mathbf{p}_\perp}{m_e c} &= \frac{e\mathbf{A}}{m_e c^2}, \\ \frac{E_{\text{kin}}}{m_e c^2} &= \frac{1}{2}\frac{e^2\mathbf{A}^2}{m_e^2 c^4}. \end{aligned} \tag{2.3.5}$$

One can see that both the longitudinal kinetic momentum and the kinetic energy scale with the square of the vector potential. The transverse kinetic momentum, in contrast to that, scales only linearly with the vector potential. The most interesting fact, however, is that all quantities can be characterized by a single normalized parameter, the so-called dimensionless vector potential[1]

$$a_0 = \frac{eA_0}{m_e c^2}. \tag{2.3.6}$$

From equations (2.3.5) and (2.3.6), it is evident that the electron reaches the relativistic regime as soon as a_0 approaches unity. Occasionally, the dimensionless parameter is also introduced in terms of the normalized electric field $a_0 = eE_0/(m_e c\omega_0)$, which allows a simple interpretation. The electric field E_0 accelerates the electron to the energy $a_0 m_e c^2$ over the distance of a reduced wavelength $\lambda_0/(2\pi)$. Clearly, a_0 can be also set in relation with the peak intensity of the wave via

$$I_0 = 1.37 \times \zeta \times \left(\frac{a_0}{\lambda_0/\mu\text{m}}\right)^2 \times 10^{18}\ \text{Wcm}^{-2}, \tag{2.3.7}$$

where ζ distinguishes between linear and circular polarization. It is $\zeta = 1$ for a linearly polarized wave and $\zeta = 2$ for a circularly polarized wave.

Notably, the exact electron trajectory can be found analytically when introducing the proper time $\tau = t - x(t)/c$. Nonetheless, a detailed discussion on the electron trajectory for the case of linear and circular polarization would be too extended at this juncture, but is given in many textbooks (see, for instance, references [25–27]). It should be just pointed out that equation (2.3.5) already

[1] It is emphasized that A_0 sets the scale for the field strength. The shape function $f(\eta)$ is of order unity.

gives several interesting insights. On the one hand, it can be seen that the electron oscillates synchronously with the vector potential in the transverse direction. On the other hand, the electron is always pushed in the propagation direction of the wave as $p_x \geq 0$. The longitudinal push is in principle also present in the non-relativistic case but becomes negligible with respect to the dominant transverse motion since $a_0 \ll 1$. Non-relativistically, the motion thus becomes purely transverse. Note also that in the end the electron will come to rest again no matter if $a_0 \gg 1$ or $a_0 \ll 1$ as the wave has a finite duration $f(\eta \to \infty) = 0$.

2.3.2 Focused electromagnetic waves

In most realistic situations strong laser waves are far away from being plane waves. A tight focusing to spots on the µm level is necessary in order to make peak intensities of the order of 10^{22} Wcm^{-2} (or higher) experimentally practicable. Such tightly focused waves are thus characterized by a spatially inhomogeneous profile in the transverse direction. This in turn directly implies a symmetry breaking and so the non-conservation of the transverse canonical momentum [see equation (2.3.3)]. Already this simple argument shows that the electron motion in tightly focused waves can be strongly altered with respect to the plane-wave case. Unfortunately, exact analytical solutions for the electron motion cannot be given in general. Qualitative insights into the electron motion can be gained anyway. This is normally achieved by exploiting the different scales responsible for the electron motion [28]. Usually, there is a short time scale induced by the rapid laser oscillations $\left(\sim \omega_0^{-1}\right)$ and a longer time scale resulting from the envelope profile which is assumed to vary much slower. Separating both scales and averaging over the rapid oscillations in the equation of motion yields an effective force that determines the motion on the long time scale,

$$\mathbf{F}_{\text{pond}} = -m_e c^2 \nabla \bar{\gamma}_e, \tag{2.3.8}$$

where $\bar{\gamma}_e$ is the averaged Lorentz factor of the electron. The force is called ponderomotive force. It is directed such that electrons are pushed into regions where they have a lower Lorentz factor. By recalling equation (2.3.5), one can see that this is physically synonymous to the fact that electrons are pushed into regions of low intensities.

2.4 Radiation losses

So far, the dynamics of single electrons in external electromagnetic fields of relativistic strength was considered. However, it is well-known from classical electrodynamics that accelerating charges emit radiation. This radiation in turn causes the charge to lose energy and momentum, which is usually not included in the Lorentz force. In most cases, this is not problematic per se as the radiation losses are negligible. In order to estimate when this evaluation changes, one can use the relativistic Larmor formula [17, 29]

$$P = \frac{2}{3} \frac{e^2}{m_e^2 c^3} \left(\gamma_e^2 \mathbf{F}_\perp^2 + \mathbf{F}_\parallel^2\right). \tag{2.4.1}$$

The formula describes the power radiated off by electrons[2] with energy $\varepsilon_e = \gamma_e m_e c^2$ moving in an electromagnetic field characterized through the force $\mathbf{F} = \mathbf{F}_\parallel + \mathbf{F}_\perp$, where $\mathbf{F}_\parallel$ and $\mathbf{F}_\perp$ denote

[2]It is noted that the following discussion can be adopted one-to-one also to positrons.

the contributions of the force acting parallel and perpendicular to the electron's momentum $\mathbf{p}$, respectively. One can easily show that equation (2.4.1) can be recast into the form

$$P = \frac{2}{3}\frac{m_e c^2}{\tau_C}\alpha\chi_e^2, \tag{2.4.2}$$

where $\tau_C = \hbar/\left(m_e c^2\right) \simeq 1.3\times 10^{-21}$ s is the Compton time, $\alpha = e^2/(\hbar c) \simeq 1/137$ is the fine-structure constant, $\hbar$ is Planck's constant, and

$$\chi_e = \frac{\hbar}{m_e^2 c^3}\sqrt{\gamma_e^2\,\mathbf{F}_\perp^2 + \mathbf{F}_\parallel^2} \tag{2.4.3}$$

is a dimensionless and Lorentz-invariant parameter, whose physical meaning will be discussed shortly. Generally speaking, it becomes important to include radiation losses into the dynamics as soon as they approach the same order of magnitude as the energy gain due to the external field. If one assumes the characteristic time scale of the field to be ω_0, one can estimate the energy change as $\mathrm{d}\varepsilon_e/\mathrm{d}t \simeq \omega_0\gamma_e m_e c^2$. Setting this in relation to equation (2.4.2) yields

$$\frac{2}{3}\alpha\chi_e^2 \simeq \gamma_e\,\omega_0\tau_C, \tag{2.4.4}$$

which defines the classical radiation-dominated regime [30]. For electrons with $\gamma_e \sim 1000$ that counter-propagate to an electromagnetic wave, radiation losses get important when the normalized field strength approaches $a_0 \sim 150$. So, it corresponds to a high-intensity effect. Technically, these losses are typically modeled with the help of a friction force (see section 3.2). The supplement 'classical' additionally requires the parameter χ_e to be much smaller than unity, $\chi_e \ll 1$. This can be motivated with the characteristic energy of the emitted radiation. Considering, for instance, the radiation emitted in the case of pure transverse fields $\mathbf{F}_\parallel = 0$ and $\mathbf{F}_\perp \neq 0$, which is occasionally combined under the term synchrotron radiation. There, the spectrum of the emitted radiation is defined by the characteristic energy [18]

$$\varepsilon_c = \frac{3}{2}\chi_e\varepsilon_e. \tag{2.4.5}$$

Apparently, equation (2.4.5) predicts unphysical behavior when $\chi_e \gtrsim 1$, since the characteristic energy carried away by the radiation exceeds the energy of the emitter. That is a lack in the classical theory and so demands an amendment in the regime $\chi_e \gtrsim 1$. A further hint is also given in χ_e itself, because of the proportionality to Planck's constant[3]. One can therefore regard χ_e as a measure of how important a fully quantum mechanical description in terms of QED—the fundamental quantum theory describing the interaction of charged particles with electromagnetic fields—is. The more general approach leads to the regime of strong-field QED which will be discussed next.

2.5 Strong-field QED

The parameter χ_e was shown to parameterize the need for a full quantum mechanical treatment. It is therefore known as the *quantum nonlinearity parameter*. Its physical origin becomes evident

[3] Please note that the radiated power P [see equations (2.4.1) and (2.4.2)] is a purely classical quantity as it is in total independent of $\hbar$.

when rewriting the expression for χ_e in equation (2.4.3) through electric field $\mathbf{E}$ and magnetic field $\mathbf{B}$. In doing so, one has [31]

$$\chi_e = \frac{\gamma_e \sqrt{(\mathbf{E} + \boldsymbol{\beta} \times \mathbf{B})^2 - (\boldsymbol{\beta} \cdot \mathbf{E})^2}}{E_{\text{crit}}} = \frac{E_{\text{rest}}}{E_{\text{crit}}}. \tag{2.5.1}$$

Here, $\boldsymbol{\beta} = \mathbf{p}/(\gamma_e m_e c)$ is the normalized velocity of the electron and $E_{\text{crit}} = m_e^2 c^3/(e\hbar) \simeq 1.3 \times 10^{16}\ \text{Vcm}^{-1}$ is the critical field of QED [32–34], which can perform work of $m_e c^2$ over a reduced Compton wavelength $\lambda\!\!\!^{-}_C = \hbar/(m_e c)$. In the last step, the numerator in equation (2.5.1) was identified as the magnitude of the electric field seen by the electron in its own rest frame. The meaning of χ_e is striking in that notation, and it becomes also clear why a quantum treatment is necessary when $\chi_e \gtrsim 1$. Effectively, the electron sees in its own rest frame an electric field of the order of the QED critical field. As a consequence, one enters the regime of strong-field QED, where (nonlinear) quantum effects become important. Which effects are particularly of interest and what approximations are used will be explained in the following.

2.5.1 Locally constant field approximation and constant-crossed fields

As discussed in the previous section, the classical regime of radiation losses has shortcomings when the parameter χ_e approaches unity. These unphysical issues can be tackled by considering the photon emission process in the framework of QED. The quantum theory provides scattering cross sections, which describe the transition from an initial state in the infinite past to a final state in the infinite future; and these scattering cross sections determine the probability for the process to occur. In general, the details of the calculation depend on the geometry of the interaction like, for instance, the spatio-temporal structure of the field and the particle's energy-momentum. However, if the formation length l_f for the QED process is much smaller than the characteristic length scale of the electromagnetic field variation,

$$l_f \ll \frac{|\mathbf{E}^2|}{|\nabla\, \mathbf{E}^2|}, \tag{2.5.2}$$

then the details of the global field structure will be secondary. This follows from the fact the particle sees locally a constant field. It is thus sufficient to calculate the QED cross section for constant electromagnetic background fields, which may reduce the calculus significantly. The corresponding approximation is called *locally constant field approximation* and is an essential ingredient for high-intensity laser-matter modeling. To make that clear, consider the case of ultra-intense optical fields, $a_0 \gg 1$ (such fields are basically studied in this thesis). There, the formation length scales as $l_f \sim \lambda_0/a_0 \ll \lambda_0$ [35, 36]. One sees the formation length to be always much smaller than any field-related length scale that is naturally restricted to λ_0. Thus, the QED cross sections depend only on the local electromagnetic fields at the particle position.

Unfortunately, one can still think of a vast number of different constant electromagnetic fields. So, the calculation of the transition rate in general will require knowledge about the local shapes of $\mathbf{E}$ and $\mathbf{B}$. Relativistically, the fields are characterized through the electromagnetic field tensor $F_{\mu\nu}$. On the other hand, the particle is described by its four-momentum p^ν. To ensure Lorentz invariance, the QED transition formulas now can only depend on the Lorentz invariants formed by p^ν and $F_{\mu\nu}$ [37]. These invariants are explicitly given by

$$\begin{aligned}
\chi &= \frac{\sqrt{\left(-F_{\mu\nu}p^\nu\right)^2}}{m_e c E_{\text{crit}}}, \\
f &= -\frac{F_{\mu\nu}F^{\mu\nu}}{2E_{\text{crit}}^2} = \frac{\mathbf{E}^2 - \mathbf{B}^2}{E_{\text{crit}}^2}, \\
g &= \frac{\varepsilon_{\mu\nu\alpha\beta}F_{\mu\nu}F^{\alpha\beta}}{8E_{\text{crit}}^2} = \frac{\mathbf{E}\cdot\mathbf{B}}{E_{\text{crit}}^2}.
\end{aligned} \tag{2.5.3}$$

Here, χ is the previously defined quantum nonlinearity parameter [see equations (2.4.3) and (2.5.1)] in Lorentz-invariant notation[4], and f, g are two dimensionless Lorentz-invariants characterizing the electromagnetic field. The QED transition rate of a process in an arbitrarily constant field can then be written as a function of χ, f, and g only, $W = W(\chi, f, g)$. Importantly, following Nikishov and Ritus [37], one can neglect the invariants f, g, so that one can approximate the QED transition rate through $W = W(\chi, 0, 0)$. The approximation is justified as long as one has $f, g \ll 1$ and $f, g \ll \chi^2$, implying weak fields with respect to the critical field E_{crit} and ultra-relativistic particles, respectively. Obviously, this has the advantage that all systems in which χ is the same will give the same result, and that one can do the calculations where it is simplest. The most common choices are the static magnetic field [38, 39] and the constant-crossed field [37]. In the latter, the electric and the magnetic field are equal in magnitude $\left(\mathbf{E}^2 = \mathbf{B}^2\right)$ and perpendicular to each other ($\mathbf{E}\cdot\mathbf{B} = 0$), resulting in $f = g = 0$. The constant-crossed case is particularly interesting since each electromagnetic field is very close to a plane wave in the rest frame of ultra-relativistic particles [35]. Within the locally constant field approximation the plane wave can then be regarded as a constant-crossed field.

2.5.2 Nonlinear Compton scattering

In the context of the radiation by an accelerating electron, the main quantum effect is the recoil on the electron caused by the emission of a single high-energy photon. This process is often referred to as *nonlinear Compton scattering*[5], but it is also known under *quantum synchrotron radiation* or *quantum radiation reaction*. Formally, it can be expressed as

$$e^- + n\gamma_l \to e^- + \gamma, \tag{2.5.4}$$

where the ultra-relativistic electron is stimulated to emit the high-energy photon γ due to the interaction with n photons γ_l from the strong background field. Historically, the process is well understood in the framework of QED, and the calculation of the corresponding scattering cross section is possible for specific field structures. For the prominent case of constant-crossed fields, one finds that the differential photon emission rate is given by [37, 40]

$$\frac{\mathrm{d}W_{\text{rad}}}{\mathrm{d}\varepsilon_\gamma} = -\frac{\alpha m_e c^2}{\tau_C \varepsilon_e^2}\left[\int_x^\infty \mathrm{d}u\,\mathrm{Ai}\,(u) + \left(\frac{2}{x} + \chi_\gamma\sqrt{x}\right)\mathrm{Ai}'(x)\right], \tag{2.5.5}$$

[4] To clarify: The parameter χ can be defined for electrons, positrons, and photons. In the following, χ will only refer to a specific particle species, if an index is given (e for electrons and positrons, and γ for photons). Otherwise, χ is not restricted to one species.

[5] Note that the process is labeled as Compton and not as inverse Compton scattering, although energy is transferred from an ultra-relativistic electron to a photon.

where $x = [\chi_\gamma/(\chi_e\chi_e')]^{2/3}$, $\mathrm{Ai}(\cdot)$ and $\mathrm{Ai}'(\cdot)$ are the Airy function and its derivative, respectively. Equation (2.5.5) describes the transition from an electron with initial energy ε_e and quantum parameter χ_e to an electron with energy ε_e' (χ_e') after the emission of a high-energy photon with energy ε_γ (χ_γ). The recoil on the electron demands $\chi_e' = \chi_e - \chi_\gamma$, and since the emitted photon energy cannot exceed the energy of the emitting electron, $\chi_e' > 0$ holds ($\chi_\gamma < \chi_e$). Integrating over all possible photon energies $0 < \varepsilon_\gamma < \varepsilon_e$ yields the total photon emission rate,

$$W_{\mathrm{rad}} = \frac{\alpha m_e c^2}{3\sqrt{3}\pi\tau_C\varepsilon_e}\int_0^\infty \mathrm{d}u\,\frac{5u^2+7u+5}{(1+u)^3}K_{2/3}\left(\frac{2u}{3\chi_e}\right). \tag{2.5.6}$$

Here, $K_{2/3}(\cdot)$ is the modified Bessel function of the second kind. Though the integral expression in equation (2.5.6) cannot be solved in terms of any standard algebraic function, it is possible to find asymptotic scalings for the total photon emission rate in the limiting cases of small ($\chi_e \ll 1$) and large ($\chi_e \gg 1$) values of the quantum nonlinearity parameter. The calculation leads to

$$W_{\mathrm{rad}} \simeq \frac{m_e c^2}{\tau_C\varepsilon_e}\begin{cases}1.44\,\alpha\chi_e & \text{for } \chi_e \ll 1,\\ 1.46\,\alpha\chi_e^{2/3} & \text{for } \chi_e \gg 1.\end{cases} \tag{2.5.7}$$

Physically speaking, the inverse of the total photon emission rate in equations (2.5.6) and (2.5.7) can be interpreted as a measure for the characteristic time elapsing between the emission of two independent photons by the ultra-relativistic electron, $t_{\mathrm{rad}} \sim W_{\mathrm{rad}}^{-1}$. In similar fashion, one can find an expression for the total power emitted by the electron,

$$P = \frac{\alpha m_e c^2}{3\sqrt{3}\pi\tau_C}\int_0^\infty \mathrm{d}u\,u\,\frac{4u^2+5u+4}{(1+u)^4}K_{2/3}\left(\frac{2u}{3\chi_e}\right). \tag{2.5.8}$$

Concentrating again on the limits $\chi_e \ll 1$ and $\chi_e \gg 1$, the total power equals

$$P \simeq \frac{m_e c^2}{\tau_C}\begin{cases}\frac{2}{3}\,\alpha\chi_e^2 & \text{for } \chi_e \ll 1,\\ 0.37\,\alpha\chi_e^{2/3} & \text{for } \chi_e \gg 1.\end{cases} \tag{2.5.9}$$

Obviously, the full quantum mechanical treatment matches the classical result in the limit $\chi_e \ll 1$ [see equation (2.4.2)], and so delivers the χ_e^2 scaling. In the opposite limit, however, one can see that the scaling of the total power is reduced. This is a consequence of the fact that the energy of the photon cannot exceed the energy of the emitting electron.

2.5.3 Multi-photon Breit-Wheeler pair production

The emission of high-energy photons has further implications than only the recoil on the electron. In a strong background field, these photons can decay into electron-positron pairs. Frequently, the process is called *multi-photon Breit-Wheeler* pair production [41], which has no classical counterpart. In constant-crossed fields, the energy distribution per unit time of an electron created according to the Breit-Wheeler process reads [37, 40]

$$\frac{\mathrm{d}W_{\mathrm{pair}}}{\mathrm{d}\varepsilon_{e^-}} = \frac{\alpha m_e c^2}{\tau_C\varepsilon_\gamma^2}\left[\int_x^\infty \mathrm{d}u\,\mathrm{Ai}(u) + \left(\frac{2}{x} - \chi_\gamma\sqrt{x}\right)\mathrm{Ai}'(x)\right]. \tag{2.5.10}$$

The definition of the variable x remains unchanged, though the meaning of χ_γ, χ_e and χ_e' has to be modified. Since now the high-energy photon γ initiates the process, its energy determines the dynamics. This means that for the created electron $\chi_e < \chi_\gamma$ holds. Accordingly, one has to redefine χ_e' as $\chi_e' = \chi_\gamma - \chi_e > 0$, which now describes the created positron. Importantly, equation (2.5.10) is symmetric under the commutation of electron and positron $\chi_e \leftrightarrow \chi_e'$. Integrating finally equation (2.5.10) over all possible electron energies $0 < \varepsilon_e < \varepsilon_\gamma$ yields the total pair-creation rate,

$$W_{\text{pair}} = \frac{\alpha m_e c^2}{3\sqrt{3}\pi\tau_C\varepsilon_\gamma}\int_0^1 \mathrm{d}u\,\frac{9-u^2}{1-u^2}\,K_{2/3}\left(\frac{8}{3(1-u^2)\chi_\gamma}\right). \tag{2.5.11}$$

As for photon emission, equation (2.5.11) allows finding an asymptotic scaling behavior,

$$W_{\text{pair}} \simeq \frac{m_e c^2}{\tau_C\varepsilon_\gamma}\begin{cases}0.23\,\alpha\chi_\gamma\exp[-8/(3\chi_\gamma)] & \text{for } \chi_\gamma \ll 1,\\ 0.38\,\alpha\chi_\gamma^{2/3} & \text{for } \chi_\gamma \gg 1.\end{cases} \tag{2.5.12}$$

For large values $\chi_\gamma \gg 1$, the scaling is similar to that of the total photon emission rate and differs only by a numerical factor of the order unity. Considering in contrast small values $\chi_\gamma \ll 1$, one observes a rather different behavior, and one can see that pair creation is exponentially suppressed. This underlines the fact that pair creation describes a threshold process, and hence the decay of photons with energy $\varepsilon_\gamma \lesssim 2m_e c^2$ into electron-positron pairs is very unlikely. Note also that the total pair-creation rate in equations (2.5.11) and (2.5.12) describes the characteristic life time of a hard photon, before it decays into an electron-positron pair.

3 Numerical modeling of high field laser–plasma interactions

This chapter gives an introduction in the numerical algorithm that will be used throughout the present thesis. It begins with a brief review about the particle-in-cell method, which is a widely spread numerical approach in order to gain deep insights into relativistic laser–plasma interactions. The subsequent sections focus on how this approach needs to be modified at extremely high intensities. In this regard, it will be explained how synchrotron radiation can be implemented in the classical (see section 3.2) and quantum limit (see section 3.3). Section 3.3 will additionally discuss how the Breit-Wheeler pair production process can be included into the numerical codes. Finally, the implementation of the QED module into the code `VLPL` will be benchmarked in the last part of the chapter (see subsection 3.3.2).

3.1 Introduction of the particle-in-cell method

As soon as one studies plasma, one usually has to deal with a large number of charged particles. This can be easily understood when considering a typical laser–plasma interaction in which a homogeneous plasma with density $\sim 10 n_{\mathrm{cr}}$ interacts with a laser of wavelength $\sim \lambda_0 = 1\ \mu\mathrm{m}$ in a cube of volume $\sim \lambda_0^3$. There, the total number of electrons is already of the order of 10^{10}. This huge number makes a tracking of the individual particles impracticable from a computational point of view. A statistical description in the phase space is therefore much more common. If inter-particle correlations are small, then the system can be well resolved by a single-particle distribution function $f_\mu(\mathbf{x},\mathbf{p},t)$ for each particle species μ. For ultra-relativistic particles mainly treated within this thesis (see the subsequent chapters), the time evolution of $f_\mu(\mathbf{x},\mathbf{p},t)$ under the influence of collective but arbitrary electromagnetic fields is governed by the collisionless Boltzmann-Vlasov equation

$$\frac{\partial f_\mu}{\partial t} + \frac{\mathbf{p}}{\gamma m_\mu}\nabla_{\mathbf{x}} f_\mu + \frac{q_\mu}{m_\mu}\left(\mathbf{E} + \frac{\mathbf{p}}{\gamma m_\mu c}\times\mathbf{B}\right)\nabla_{\mathbf{p}} f_\mu = 0. \tag{3.1.1}$$

Here, $\nabla_{\mathbf{x}}$ and $\nabla_{\mathbf{p}}$ represent the Nabla operator acting on the position and momentum space, and m_μ, q_μ and γ are the particle's mass, charge and Lorentz factor. The motion of charged particles as described by equation (3.1.1) leads to modifications in the charge distribution ρ and to currents $\mathbf{j}$, which in turn act as a source for new electromagnetic fields in Maxwell's equations,

$$\operatorname{div}\mathbf{E} = 4\pi\rho, \qquad \operatorname{div}\mathbf{B} = 0, \tag{3.1.2}$$

$$\frac{\partial \mathbf{E}}{\partial t} = c\,\operatorname{rot}\mathbf{B} - 4\pi\mathbf{j}, \quad \text{and} \quad \frac{\partial \mathbf{B}}{\partial t} = -c\,\operatorname{rot}\mathbf{E}. \tag{3.1.3}$$

The simultaneous solution of equation (3.1.1) and Maxwell's equations allows a description of the plasma in a self-consistent manner. Analytically, this is a rough challenge and almost

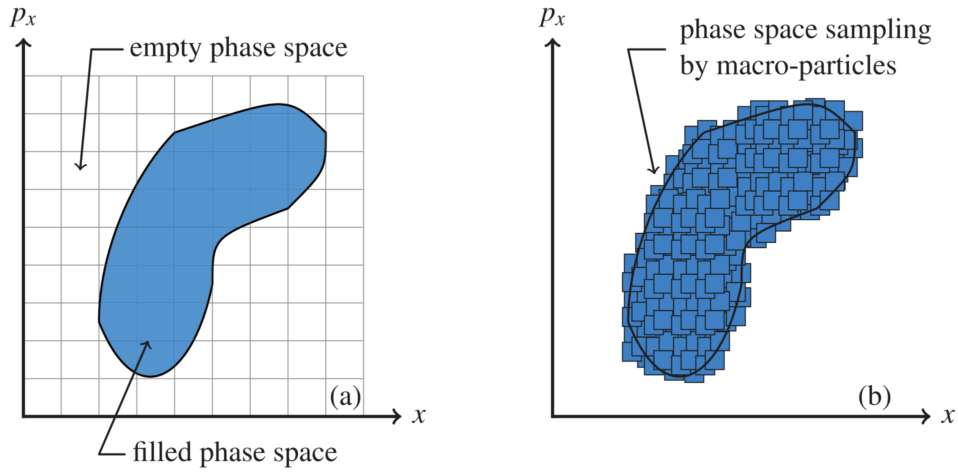

Figure 3.1.1: (a) Typical shape of the particle distribution function $f_\mu(x, p_x, t)$ in a two-dimensional phase space (x, p_x) at time t. Only the colored area is occupied by particles. (b) Sampling of the distribution function $f_\mu(x, p_x, t)$ by macro-particles.

impossible to tackle in the vast number of situations. From a numerical point of view, in contrast, a solution can be straightforwardly enforced by discretizing the phase space as well as Maxwell's equations on an Eulerian grid on which the equations are solved subsequently. In fact, this ansatz is pursued by several people (see, for example, [42–45] and the references therein). These Vlasov-Maxwell codes, however, require a lot of computational resources even in relatively simple problems. To make this clear, a look at the plot in figure 3.1.1(a) may help. There, one can see the shape of an arbitrary particle distribution function $f_\mu(x, p_x, t)$ in a two-dimensional phase space (x, p_x). It is important to notice that only the colored area is meant to be filled with particles at time t, whereas the rest of the phase space is empty. At later times, the distribution of particles may change and particles may occupy regions of the phase space that are empty for now. Hence, it has to be ensured at any time that the discretized phase space gathers all the areas in which the distribution function may be non-zero over the entire simulation time. Basically, this can be fulfilled by making the grid large enough. It should be clear that this procedure naturally includes a lot of empty and/or unappealing phase space areas. These have to be processed anyway, so unnecessarily wasting computational resources. Moreover, even systems that can be well described by a single spatial coordinate typically require more than one momentum dimension to capture the particle motion properly. In this way, one has to cover even larger phase space volumes, making a solution of the coupled Vlasov-Maxwell system even more computationally demanding.

At this point, the particle-in-cell (PIC) method offers an interesting and efficient alternative. First pioneering works in that direction were conducted by Buneman already in the late 1950s [46] and by Dawson in the early 1960s [47]. Later, these works were advanced by Hockney and Eastwood [48] as well as by Birdsall and Langdon [49] to develop the PIC method. The idea behind the method is in principle rather simple and intuitive. The focus is laid on the distribution function itself instead of considering a huge phase space volume. This is realized by sampling the distribution function through *finite phase-fluid elements* as exemplarily indicated in figure 3.1.1(b). Figuratively speaking, the n-th finite phase-fluid element merges particles from a small phase space volume into a single phase-fluid element characterized through its center position $\mathbf{x}_n$ and momentum $\mathbf{p}_n$. Importantly, $\mathbf{x}_n$ and $\mathbf{p}_n$ do not necessarily need to be arranged on an Eulerian grid, but can be continuous instead. It is then possible to express the entire distribution function as a sum over all phase-fluid elements N_μ,

$$f_\mu(\mathbf{x},\mathbf{p},t) \simeq \sum_n^{N_\mu} w_n S(\mathbf{x}-\mathbf{x}_n,\mathbf{p}-\mathbf{p}_n). \tag{3.1.4}$$

Here, the weight w_n is a measure for the number of particles unified in the n-th phase-fluid element and $S(\mathbf{x},\mathbf{p})$ stands for a function giving information about the shape of the merged phase space volume. In the context of PIC, the shape is commonly taken to be box-like in space and delta-like in the momenta,

$$S(\mathbf{x}-\mathbf{x}_n,\mathbf{p}-\mathbf{p}_n) = \delta(\mathbf{p}-\mathbf{p}_n)\prod_{i=1}^{3}\Theta\left(\frac{\Delta x_i}{2}-|x_i-x_{n,i}|\right), \tag{3.1.5}$$

with $\delta(\cdot)$ and $\Theta(\cdot)$ being the Dirac delta and the Heaviside step function, respectively. It is also noted that the phase-fluid elements are called (numerical) macro-particles in the language of PIC as they substitute a certain number real physical particles. Notably, each macro-particle n needs to propagate along the characteristics of the Boltzmann-Vlasov equation (3.1.1) in order to ensure the correct evolution of the distribution function in the phase space. Recalling equation (3.1.1), one finds that the characteristics are given by

$$\begin{aligned} \frac{\mathrm{d}\mathbf{x}_n}{\mathrm{d}t} &= \frac{\mathbf{p}_n}{\gamma_n m_\mu}, \\ \frac{\mathrm{d}\mathbf{p}_n}{\mathrm{d}t} &= q_\mu\left(\mathbf{E}+\frac{\mathbf{p}_n}{\gamma_n m_\mu c}\times\mathbf{B}\right). \end{aligned} \tag{3.1.6}$$

These are exactly the relativistic equations of motion for a particle with momentum $\mathbf{p}_n$ and position $\mathbf{x}_n$ which is subjected to an electromagnetic field. More importantly, a macro-particle follows the same trajectory as a single particle because their charge-to-mass ratio is the same. As before in the Vlasov case, the current induced by the motion of the macro-particles allows a self-consistent description of the plasma when it is used for the temporal evolution of the electromagnetic fields in Maxwell's equations (3.1.2)-(3.1.3). The numerical current must necessarily fulfill the continuity condition,

$$\partial_t\rho + \operatorname{div}\mathbf{j} = 0. \tag{3.1.7}$$

Under such circumstances it is enough to take care of the explicitly time-containing update equations (3.1.3)—also known as Faraday's and Ampère's law—because equations (3.1.2) will automatically remain fulfilled if they are in the beginning of the simulation[1]. Unfortunately, there is no way to circumvent the numerical solution of Maxwell's update equations (3.1.3) on the grid. How this can be done in detail goes beyond the scope of this brief introduction. It should just be mentioned here that the literature contains a series of different Maxwell solvers, starting with the famous method by Yee [50] over pseudo-spectral approaches in Fourier space [51] to (near-)dispersionless solvers [52, 53]. Despite, the main advantage of the PIC modeling lies in the fact that the mesh needed for the Maxwell solver does not cover more than three dimensions as one only has to discretize the real space. The more so as it is generally easier to estimate which part of the real space will be filled with plasma, in this way allowing the mesh

[1] One can easily show this by taking the divergence of Faraday's and Ampère's law (3.1.2) and using the continuity equation (3.1.7).

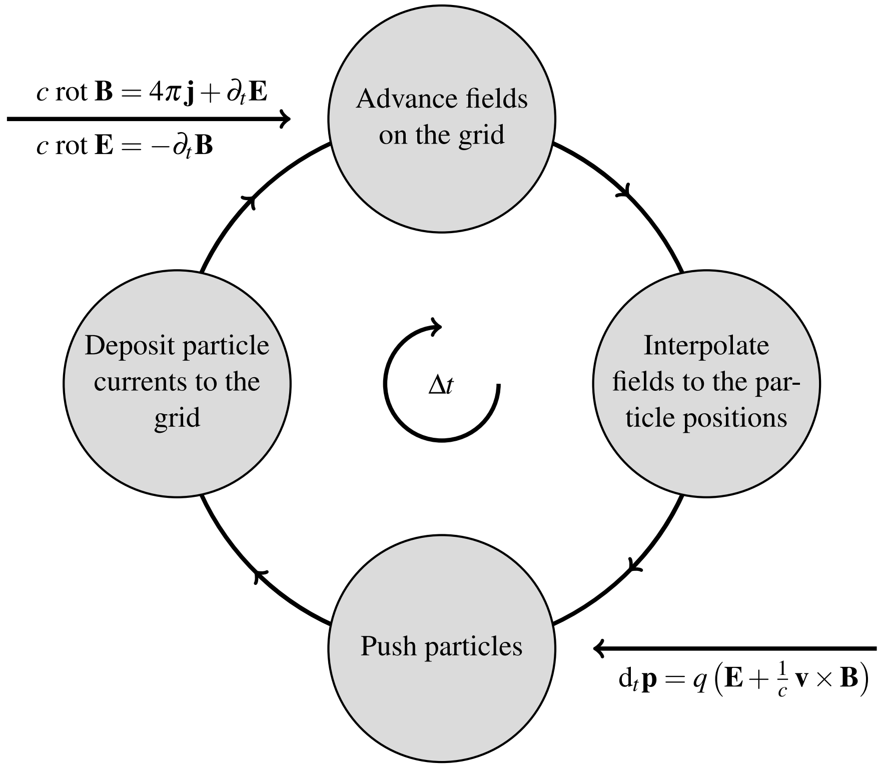

Figure 3.1.2: Schematic illustration of a standard loop in a PIC code describing the time evolution over one time step Δt.

volume to be as small as possible. This leads to a significant reduction with respect to a six-dimensional grid needed in Vlasov codes and makes simulations of physical problems also in fully three-dimensional geometries feasible. Closely linked to that, there is a vast number of PIC codes used in the community like, for instance, `VLPL` [52, 54], `OSIRIS` [55], `VORPAL` [56], `PICADOR` [57], `EPOCH` [58], and `SMILEI` [59], to list just a few.

Recapitulatory, the PIC method samples the plasma by a finite number of representative macro-particles which are pushed according to the relativistic equations of motion. The motion of the macro-particles then acts as a source term in Maxwell's equations which are finally solved on a grid. After the initialization at the beginning of each simulation, figure 3.1.2 shows the scheme that nicely summarizes a characteristic time step conducted by a PIC code. The scheme can be divided into four main blocks:

- Field interpolation: Since the fields are only known on fixed grid points, they must be interpolated to the continuous particle positions $\mathbf{x}_n$ in order to capture the correct motion.
- Particle pushing: The particles are then pushed with the interpolated force. This can be done with different particle pushers. The most common ones are the pushers introduced by Boris [60] and Vay [61]. The standard pusher implemented in `VLPL` can be found in [53, 54].
- Current deposition: After the particle pushing, one interpolates the generated current to the grid on which the fields are known.
- Advance fields: Finally, the fields can be advanced with the grid currents.

The procedure is repeated until the desired interaction time is elapsed. Numerically, the simulation will show a stable evolution as long as several stability conditions are satisfied. First, the Courant-Friedrichs-Lewy condition sets the spatial grid steps in relation to the time step Δt [62]. One has stable behavior when

$$c\Delta t < \frac{1}{\sqrt{\frac{1}{(\Delta x)^2} + \frac{1}{(\Delta y)^2} + \frac{1}{(\Delta z)^2}}}. \tag{3.1.8}$$

Physically, this means that information cannot be mediated faster than at the speed of light. Second, the time step must resolve the fastest oscillation in the system. In laser-solid interactions this is typically the electron plasma period $T_{pe} = 2\pi/\omega_{pe}$. And last, one should be aware that the Debye length is spatially resolved in order to avoid numerical heating effects [49]. This is a major constraint in PIC codes that are momentum conserving. There, the numerical heating will cause energy conservation to be violated. On the other hand, unphysical grid heating is inherently suppressed in energy conserving PIC codes such as `VLPL`.

If all stability criteria are met, a standard PIC code will allow the (numerical) investigation of basic laser–plasma interactions. The method described so far, however, needs to be extended at higher laser intensities as new phenomena may occur. These include radiation losses of ultra-relativistic particles and QED effects, like the generation of γ-rays and electron-positron pairs. How particularly these new phenomena can be addressed with PIC codes will be explained in the following sections.

3.2 Classical radiation reaction in PIC codes

Beyond the standard applicability range of the PIC method, it is also possible to extend its range to account for ionization, binary collisions and QED events. Especially the latter becomes increasingly vital in the interaction of high-intensity laser radiation with matter as proposed by the next generation of laser facilities. One of the first regimes that will be in reach is the classical radiation-dominated regime (see section 2.4), where electrons suffer significant radiation losses so causing a back-reaction on the electron motion. Though it seems at first glance that the back-reaction is inherently included in the self-consistent PIC modeling, this is not the case. The reason here is the frequency of the emitted radiation. It scales like $\omega_c = 3\chi\varepsilon_e/(2\hbar)$, where ω_c is the critical frequency of classical synchrotron radiation [18], and generally covers frequencies up to the (hard) x-ray level. However, due to the time discretization in PIC codes, the maximum frequency $\omega_{\max}$ that can be numerically resolved is determined by the time step Δt, $\omega_{\max} \sim \pi/\Delta t$. Resolving (hard) x-ray frequencies on the grid would thus require extremely small time steps, which is impracticable from a computational point of view. Luckily, the electromagnetic spectrum of *low*-frequency (induced by particle currents on the grid) and *high*-frequency radiation (induced by radiation losses) is asymmetric and well separated from each other (see, for instance, figures 1 and 2 in [63]). This enables the detachment of the high-frequency part from the grid, with the result that high frequencies are treated as particle-like photons. The emission of such a high-frequency photon then causes a recoil on the emitting electron. Though the recoil induced by the emission of a single photon is low in the classical regime ($\chi \ll 1$), the electron emits a large number of photons which means that the cumulative recoil can have a finite impact on the dynamics [30]. Technically, one therefore introduces—additionally to the usual Lorentz force $\mathbf{F}_L$—a continuous friction force $\mathbf{F}_{\text{rad}}$ mediating the back-reaction,

$$\frac{\mathrm{d}\mathbf{p}}{\mathrm{d}t} = \mathbf{F}_L + \mathbf{F}_{\text{rad}}. \tag{3.2.1}$$

This is known as radiation reaction and the force $\mathbf{F}_{\text{rad}}$ is thus also referred to as radiation reaction force. The first model that considered relativistic radiation reaction in a self-consistent way was given by the Lorentz-Abraham-Dirac (LAD) equation [64]. Although derived from Maxwell's equations and the relativistic equation of motion, the LAD model will give rise to a number of physical problems such as *runaway* solutions even if no external field is present. In the literature one can therefore find a couple of approximations to the LAD equation that are used to circumvent these issues and to simulate radiation reaction in numerical codes [65]. The most common ones are the approximations by Landau and Lifschitz [18] and by Sokolov [66], both of which are used in many studies [67–71].

The implementation of the classical radiation reaction module in the code `VLPL` [72] follows the same idea as the aforementioned approaches. The time-averaged dissipated power caused by the friction force $\mathbf{F}_{\text{rad}}$ is equal to the total emitted power P by the relativistic particle [29],

$$P = \frac{2e^2}{3m_e^2c^3}\gamma^2\left[\left(\frac{\mathrm{d}\mathbf{p}}{\mathrm{d}t}\right)^2 - \frac{1}{c^2}\left(\frac{\mathrm{d}\varepsilon}{\mathrm{d}t}\right)^2\right]. \tag{3.2.2}$$

Note that the changes in the momentum vector and in the energy are caused by the driving force and not by the friction force. Evaluating equation (3.2.2) for the case of longitudinal $\mathrm{d}\mathbf{p}/\mathrm{d}t \parallel \mathbf{p}$ and transverse $\mathrm{d}\mathbf{p}/\mathrm{d}t \perp \mathbf{p}$ accelerating fields, one easily finds the relations

$$P_\parallel = \frac{2e^2}{3m_e^2c^3}\left[\left(\frac{\mathrm{d}\mathbf{p}}{\mathrm{d}t}\right)_\parallel\right]^2 \quad \text{and} \quad P_\perp = \frac{2e^2}{3m_e^2c^3}\gamma^2\left[\left(\frac{\mathrm{d}\mathbf{p}}{\mathrm{d}t}\right)_\perp\right]^2. \tag{3.2.3}$$

One can see that the radiation due to longitudinal accelerating fields is reduced by a factor γ^2 in comparison with an acceleration in the transverse direction, and so can be neglected since one is only interested in ultra-relativistic particles, $\gamma \gg 1$. This results in a synchrotron-like case in which the radiation is emitted into a cone with opening angle of $\theta \approx 1/\gamma \ll 1$ around the particle's propagation direction. Accordingly, it is convenient to assume that the friction force acts only opposite to the particle's direction of motion,

$$\mathbf{F}_{\text{rad}} = -\frac{P_\perp}{c}\,\hat{\mathbf{e}}_{\mathbf{p}}. \tag{3.2.4}$$

In a small time interval Δt, this friction force induces a momentum change of $\Delta p_{\text{rad}} = |\mathbf{F}_{\text{rad}}\Delta t|$, which can be easily recast into the form

$$\begin{aligned}\Delta p_{\text{rad}} &= \left(\frac{4}{9}\,\alpha\,\frac{|\Delta\mathbf{p}_\perp|}{m_e c}\right)\hbar k_c \\ &= N_{\text{photons}}\,\hbar k_c.\end{aligned} \tag{3.2.5}$$

The equation can be understood such that in each time interval Δt the particle emits N_{photons} photons with a characteristic momentum of $\hbar k_c$. This momentum is connected with the critical frequency ω_c via $\omega_c = ck_c$, and can be calculated from

$$\hbar k_c = \frac{3}{2}\frac{\hbar}{m_e c^2}\frac{|\Delta\mathbf{p}_\perp|}{\Delta t}\gamma^2. \tag{3.2.6}$$

The momentum change in equation (3.2.5) can be straight-forwardly integrated into the typical PIC loop and the corresponding calculation is performed after the normal Lorentz force push (see figure 3.1.2). Moreover, the number of emitted photons N_{photons} and the characteristic momentum [see equation (3.2.6)] are stored along the particle trajectory to enable further analysis of the emitted photon spectrum.

When the quantum nonlinearity parameter approaches and exceeds unity, $\chi \gtrsim 1$, a classical description of the radiation losses is no longer applicable. This can be nicely seen in equations (3.2.5) and (3.2.6), where the critical momentum (or frequency) appears and so defines the energy-momentum scale of the emitted radiation. Physically speaking, it means that the classical theory predicts characteristic photon energies $\hbar\omega_c$ that exceed at $\chi \gtrsim 1$ the energy of the emitting particle ε_e. The inconsistent behavior implies a fundamental change at $\chi \sim 1$ and is solved by QED. The easiest way of including such quantum corrections from a technical perspective is the multiplication of the radiation reaction force with a quantum correction factor $g(\chi)$, which is occasionally done [73]. This approach, however, relies on the radiation losses to be continuous and smooth. Obviously, it cannot capture any substantial recoil on the electron in a single emission nor the stochastic nature of the emission event. The following section explains how such QED events are implemented into the PIC code `VLPL`.

3.3 Implementation of QED processes into PIC codes

The next generation of laser facilities like ELI or XCELS will provide light-matter experiments that will enable studies in the onset of the QED regime. In order to study these conditions also in numerical simulations, the standard PIC approach has been extended to include the QED processes of nonlinear Compton scattering and Breit-Wheeler pair production in a self-consistent way. As a consequence, a couple of QED-PIC codes have been developed in the recent decade [55, 58, 63, 74]. Though not all codes use the same numerical algorithms, the basic numerical concept is always the same. The QED events are implemented by means of a Monte-Carlo algorithm. This routine enables the modeling of the probabilistic nature of quantum events and is added as an additional step to the standard PIC loop. The following section is dedicated to explain in detail how the QED events are incorporated into standard PIC codes, considering particularly the code `VLPL`. Please note that the `VLPL` implementation follows the alternative version of the Monte-Carlo algorithm first introduced by Elkina *et al*. [24].

3.3.1 Description of the Monte-Carlo algorithm

In `VLPL` the Monte-Carlo algorithm is executed right after the momenta of the particles are pushed according to the Lorentz force. The algorithm can thereby be divided into two independent subroutines. The first subroutine treats the emission of high-energetic photons by ultra-relativistic particles, frequently termed as the nonlinear Compton scattering process. The emitting particle can be either an electron or a positron and is assigned the index e. The decision whether such a parent particle emits a photon or not is made as follows. In a first step, one generates a uniformly distributed random number $r_1 \in [0,1]$. The random number r_1 defines the energy and the momentum of the photon that is considered to be emitted,

$$\varepsilon_\gamma = r_1\, \varepsilon_e^{\text{kin}} \qquad \text{and} \qquad \mathbf{p}_\gamma = \frac{\varepsilon_\gamma}{c}\, \hat{\mathbf{p}}_e. \tag{3.3.1}$$

Here $\varepsilon_e^{\mathrm{kin}} = (\gamma_e - 1)\, m_e c^2$ stands for the (kinetic) energy of the emitting particle and $\hat{\mathbf{p}}_e$ is the unit vector corresponding to the particle momentum, $|\hat{\mathbf{p}}_e| = 1$. Equation (3.3.1) states that the photon momentum is assumed to be parallel to the momentum of the emitting particle. The reason for that is the narrow angle into which the radiation is emitted in the ultra-relativistic case (see section 3.2). In the second step, one calculates the quantum nonlinearity parameter for the emitting particle as well as for the photon. In the calculation one uses the electromagnetic fields at the local position of the particles. The probability, which is supposed to characterize the process locally within a PIC time step Δt, is subsequently modeled as

$$\mathscr{P}_\gamma = \frac{\mathrm{d}W_{\mathrm{rad}}}{\mathrm{d}\varepsilon_\gamma}\, \varepsilon_e\, \Delta t. \tag{3.3.2}$$

Combined with a second uniformly distributed random number $r_2 \in [0,1]$, equation (3.3.2) is finally applied to decide whether the process takes place or not. Only if $r_2 < \mathscr{P}_\gamma$, a photon will be emitted. From the computational point of view this is done by adding the photon as a new macro-particle to the simulation domain instead of discretizing it on the grid. The particle-like behavior is necessary because the maximum frequency that can be resolved by the grid is orders of magnitude below the typical energy of the QED-photon, $\omega_{\max} = \pi/\Delta t \ll \varepsilon_\gamma/\hbar$. The macro-photon, in the following just referred to as photon, has the same position and weight as the parent particle[2], and its momentum is given by equation (3.3.1). The momentum remains constant[3] over the simulation since photons are electrically neutral and therefore move ballistically. Beyond, the parent particle experiences a recoil to ensure the conservation of momentum at the emission location. The momentum of the parent particle has to be modified accordingly,

$$\mathbf{p}_e' = \mathbf{p}_e - \mathbf{p}_\gamma. \tag{3.3.3}$$

At this point it should be stressed that the Monte-Carlo routine conserves the momentum, but not the energy. The corresponding error in the energy can be easily estimated under the assumption of ultra-relativistic particles before and after the emission [76]. The calculation yields

$$\begin{aligned} \Delta\varepsilon =&\ \varepsilon_e' + \varepsilon_\gamma - \varepsilon_e \\ \simeq&\ \frac{m_e c^2}{2}\left(\frac{1}{\gamma_e'} - \frac{1}{\gamma_e}\right). \end{aligned} \tag{3.3.4}$$

The equation indicates that the algorithm increases the energy as $\gamma_e' < \gamma_e$. The reason behind this is that the algorithm does neither consider energy nor momentum from the classical background field at the vertex. Equation (3.3.4) also states that the energy increase is small in the limit of ultra-relativistic particles where $\varepsilon_e, \varepsilon_e' \gg m_e c^2$, and so can be neglected, especially with respect to energies of the order of $a_0 m_e c^2 \gg m_e c^2$ that are characteristic for ultra-intense laser-plasma interactions. The above subroutine is subsequently applied to all electrons and positrons in the simulation.

The second subroutine considers the decay of a high-energetic γ-photon into an electron-positron pair and works similar to the case of the photon emission module explained above. A uniformly distributed random number $\tilde{r}_1 \in [0,1]$ is again decisive for choosing the energy-momentum of

[2]Recently, Lécz and Andreev suggested the use of sub-macro-particle weights by running the QED routine more than once per parent macro-particle. This should enhance the statistics even for low numbers of initial macro-particles per cell [75].

[3]At least as long as the photon does not decay into an electron-positron pair.

the electron,

$$\mathbf{p}_{e^-} = \tilde{r}_1 \, \mathbf{p}_\gamma \qquad \text{and} \qquad \varepsilon_{e^-} = m_e c^2 \sqrt{1 + \left(\frac{\mathbf{p}_{e^-}}{m_e c}\right)^2}\,. \tag{3.3.5}$$

Afterwards, one calculates the quantum nonlinearity parameter for the decaying photon as well as for the electron at the current location. In the case of Breit-Wheeler pair production, the probability for the decay of the photon is then sampled according to

$$\mathscr{P}_{e^+e^-} = \frac{\mathrm{d}W_{\text{pair}}}{\mathrm{d}\varepsilon_{e^-}} \, \varepsilon_\gamma \, \Delta t\,. \tag{3.3.6}$$

It is assumed that the photon decays into an electron-positron pair when $\tilde{r}_2 < \mathscr{P}_{e^+e^-}$, with $\tilde{r}_2$ being a second uniformly distributed random number in the range $[0,1]$. Numerically, a successful decay is modeled by removing the photon macro-particle from the simulation domain and simultaneously adding an electron and a positron macro-particle. The macro-particle weight of electrons and positrons is equal to the weight of the decaying photon macro-particle. The momentum of the electron is given by equation (3.3.5), and the positron's momentum follows from the conservation of momentum at the vertex, $\mathbf{p}_{e^+} = \mathbf{p}_{e^-} - \mathbf{p}_\gamma$. Afterwards, the subroutine is applied to all particle-like photons in the simulation.

3.3.2 Testing the QED algorithm

In order to check the correct implementation of the QED module into the code `VLPL`, a couple of benchmark tests are performed, and the following section presents the results.

The first test series is dedicated to confirming the characteristic radiation time of an electron t_{rad} as predicted by equation (2.5.6), and is adopted from Kostyukov *et al.* [77]. For this purpose, the interaction of an ultra-relativistic electron propagating transversely to a strong and homogeneous magnetic background field is investigated. To calculate t_{rad}, the simulation stops as soon as the electron emits a photon and the elapsed time $\tilde{t}_{\text{rad}}$ is taken as a measure for t_{rad}. As a matter of fact, the characteristic radiation time describes a quantum process and should thus be seen as a mean value averaged over an ensemble of identical systems. As a consequence, the numerically calculated radiation time $t_{\text{rad}}^{\text{sim}}$ is determined as the unweighted mean of $\tilde{t}_{\text{rad}}$ over $N = 1000$ independent simulation runs. Table 3.3.1 lists the results for different initial electron energies ε_{e^-} and different magnetic fields B. One can see that the theoretically predicted value $t_{\text{rad}}^{\text{theo}}$ is always in the tolerance interval $\sigma_{\text{rad}}^{\text{sim}}$ (error on the mean value) of the simulated value $t_{\text{rad}}^{\text{sim}}$. This indicates reasonable agreement between theory and simulation.

A similar test is also performed to calculate the characteristic life time of a hard photon, which is subjected to a strong and homogeneous magnetic background field $\left(\mathbf{p}_\gamma \perp \mathbf{B}\right)$. As in the previous case, the simulation stops as soon as the photon decays into an electron-positron pair. The results are averaged over $N = 1000$ independent runs and can be found in table 3.3.2 for different initial photon energies ε_γ and different magnetic field strengths B. One can see that both the numerically calculated time $t_{\text{pair}}^{\text{sim}}$ and theoretically predicted time $t_{\text{pair}}^{\text{theo}}$ are in good agreement, since $t_{\text{pair}}^{\text{theo}}$ remains in the tolerance interval $\sigma_{\text{pair}}^{\text{sim}}$ (error on the mean value) of $t_{\text{pair}}^{\text{sim}}$.

By means of the above benchmarks both QED subroutines are tested separately and hence independently. It is therefore important to test in addition the interplay of the modules. The idea for

χ_e	ε_{e^-} $\left[m_e c^2\right]$	B $\left[10^9\,\mathrm{G}\right]$	$t_{\mathrm{rad}}^{\mathrm{theo}}$ [fs]	$t_{\mathrm{rad}}^{\mathrm{sim}}$ [fs]	$\sigma_{\mathrm{rad}}^{\mathrm{sim}}$ [fs]
0.3	10^3	13	0.48	0.50	0.02
0.3	10^4	1.3	4.84	4.99	0.16
3	10^4	13	0.72	0.72	0.02
3	10^5	1.3	7.17	7.05	0.22
30	10^5	13	1.33	1.29	0.04
30	10^6	1.3	13.33	13.31	0.44
300	10^5	130	0.28	0.28	0.01

Table 3.3.1: The table shows the numerically and analytically calculated characteristic photon emission time for different parameters. The results are averaged over 1000 individual simulation runs. In this context, $\sigma_{\mathrm{rad}}^{\mathrm{sim}}$ denotes the error on the mean value $t_{\mathrm{rad}}^{\mathrm{sim}}$.

χ_γ	ε_γ $\left[m_e c^2\right]$	B $\left[10^9\,\mathrm{G}\right]$	$t_{\mathrm{pair}}^{\mathrm{theo}}$ [fs]	$t_{\mathrm{pair}}^{\mathrm{sim}}$ [fs]	$\sigma_{\mathrm{pair}}^{\mathrm{sim}}$ [fs]
3	10^3	130	0.81	0.79	0.02
6	10^4	26	2.94	2.96	0.09
6	10^5	2.6	29.39	29.07	0.91
30	10^4	130	0.60	0.59	0.02
120	10^4	520	0.21	0.20	0.01
300	10^5	130	1.09	1.12	0.04

Table 3.3.2: The table shows the numerically and analytically calculated characteristic photon decay time in an electron-positron pair for different parameters. The results are averaged over 1000 individual runs. In this context, $\sigma_{\mathrm{pair}}^{\mathrm{sim}}$ denotes the error on the mean value $t_{\mathrm{pair}}^{\mathrm{sim}}$.

an adequate study testing that interplay was introduced by Anguelov and Vankov in 1999 [79], and nowadays their work is used in many codes as a reference [24, 63, 77, 80]. In particular, the idea is to investigate the time evolution of a QED cascade which gets initiated by a single energetic particle in a strong background field. For the benchmark shown here, the cascade is initiated by a single electron with initial Lorentz factor $\gamma_e = 2 \times 10^5$ that is subjected to a homogeneous and perpendicular magnetic field of strength $B = 0.2\,E_{\mathrm{crit}}$. The black curve in figure 3.3.1 depicts the time evolution of the cascade as obtained from the `VLPL` implementation. More precisely, the figure shows the number of all charged particles with energies larger than $10^{-3}\,\gamma_e m_e c^2$ as a function of time[4]. Note also that the data are averaged over $N = 1000$ independent runs to reduce the statistical noise. Apart from the `VLPL` results, figure 3.3.1 also presents the data from Elkina *et al.* [24] in gray. One can clearly see that they are in reasonable agreement. The slight deviation for large times can be ascribed to the fact that not exactly the same algorithm was used to generate the data. Elkina *et al.* developed two algorithms in their

[4]The normalization time t_{rad} corresponds to the previously defined radiation time. It refers to the initial electron and is equal to the inverse of the strong-field limit $\chi_e \gg 1$ in equation (2.5.7).

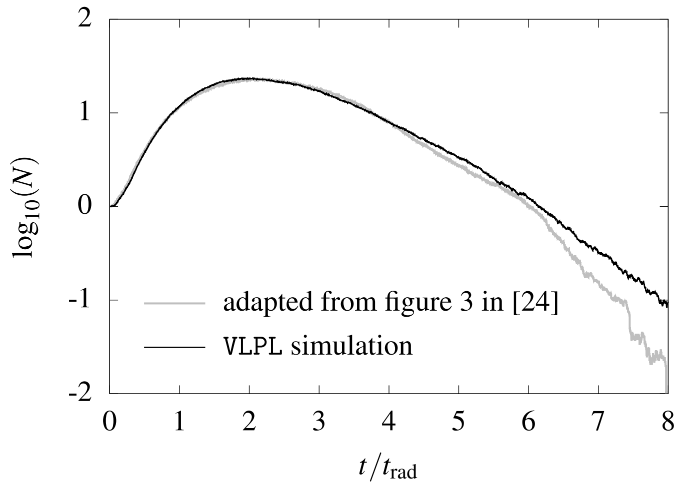

Figure 3.3.1: The figure shows a benchmark of the VLPL implementation (black solid line) against the code by Elkina *et al.* [24] (gray solid line). Particularly, the temporal evolution of a QED cascade is depicted by plotting the number of particles with a Lorentz factor exceeding 200. A single electron with Lorentz factor $\gamma_e = 2 \times 10^5$ moving perpendicular to a homogeneous magnetic background field ($B = 0.2\,E_{\mathrm{crit}}$) initiated the cascade. The plot profile is averaged over 1000 independent simulation runs. Figure published in [78], © 2016 American Physical Society, reproduced with permission, all rights reserved.

work [24]; one is called the proper event generator and the other alternative event generator. The alternative version is implemented in VLPL, since it is quicker and more efficient from the computational perspective. The data provided by Nina Elkina, however, show results for the proper event generator[5].

Following [63], a final test is performed by checking the power per unit energy $\mathrm{d}P/\mathrm{d}\varepsilon_\gamma$ emitted by an electron. This has the advantage that one can additionally check the energy distribution of the emitted photons. In particular, the test is done for an electron with $\gamma_e = 100$ in a transverse magnetic background field. The field strength is such that $\chi_e = 1$. Analytically, the expression for $\mathrm{d}P/\mathrm{d}\varepsilon_\gamma$ can be obtained by multiplying the differential photon emission rate [see equation (2.5.5)] with ε_γ [40]. Figure 3.3.2 compares the exact result for $\mathrm{d}P/\mathrm{d}\varepsilon_\gamma$ (gray solid line) with the results from the VLPL implementation (black solid line). The VLPL result is thereby obtained as follows. One runs the Monte-Carlo algorithm for a single electron ($\gamma_e = 100$, $\chi_e = 1$) and registers the energy of the photon if emission takes place. The procedure is repeated N_{runs} times. After that, one sorts the emitted photons according to their energy in equidistant bins of size $\Delta\varepsilon_\gamma$. The number of photons in bin number i, which belongs to energy $\varepsilon_{\gamma,i} = i\Delta\varepsilon_\gamma$, is denoted with N_i. In average, the spectral power can then be calculated from

$$\left.\frac{\mathrm{d}P}{\mathrm{d}\varepsilon_\gamma}\right|_{\varepsilon_{\gamma,i}} = \frac{1}{N_{\mathrm{runs}}} \frac{N_i\,\varepsilon_{\gamma,i}}{\Delta\varepsilon_\gamma \Delta t}, \tag{3.3.7}$$

where Δt is the time step used in the simulation. Taking a close look at figure 3.3.2, one can directly see that the VLPL result is in very good agreement with the exact expression.

[5] Similar deviations are also observed in other implementations (see, for instance, figure 10 in [63]).

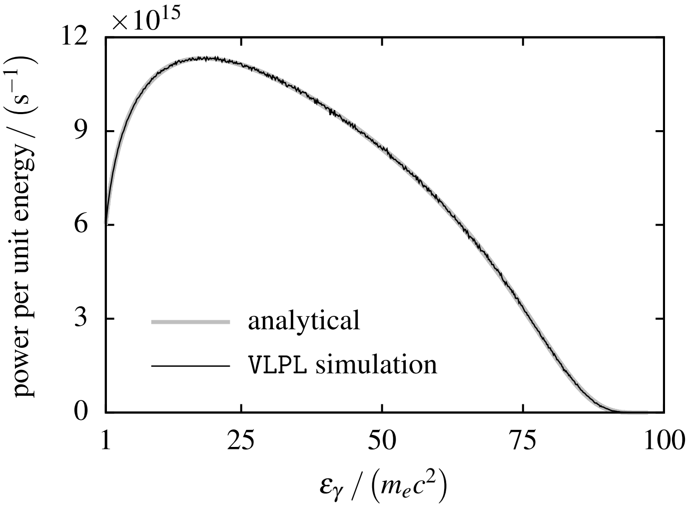

Figure 3.3.2: Results of the power per unit energy emitted by an electron with $\gamma_e = 100$ and $\chi_e = 1$ obtained from the Nikishov–Ritus theory [equation (2.5.5) multiplied by ε_γ, gray solid line] and from simulations with the `VLPL` implementation of the QED algorithm (black solid line). It is noted that the `VLPL` result is averaged over 10^7 independent runs.

In conclusion, all tests showed that one can accurately reproduce the physics in the QED regime with the PIC code `VLPL`. The following part of the thesis is therefore dedicated to actual laser–plasma simulations in regimes, where these QED effects are important.

4 Radiative trapping in standing waves of two colliding laser pulses

After the comprehensive introduction into the numerical framework used throughout the thesis at hand, the following part aims at discussing the physical problems that can be addressed with just these methods. First, it will be shown that in the standing wave generated by two colliding ultra-intense laser pulses, radiation loss effects change the electron dynamics in a plasma profoundly. It becomes possible that electrons get trapped in the electric nodes of the standing wave, so forming periodic structures. At even higher intensities, the pair production process becomes more and more impactful. In fact, it will turn out that at some point the process will be so effective that the generated electron-positron plasma alters the entire dynamics completely. It will be demonstrated that it comes to a break of the standing wave structure of the two colliding laser pulses, and correspondingly to the break of the radiative-trapping effect.
In the second part of the chapter at hand, the setup will be modified slightly. Higher-order laser modes will be used instead of usual Gaussian laser modes. The modes of interest have a more complex transverse profile and carry orbital angular momentum. They are therefore also known as twisted light. As it will be shown later, this leads to surprising changes in the electron dynamics such as radiative trapping along helical lines. It will be also pointed out that one can drive electron structures having durations on the attosecond timescale. Depending on the explicit laser parameters, these structures can be either disk-like electron bunches or helical electron beams. The main features will be finally described within a semi-analytical model.

4.1 Introduction

Basically, the importance of QED effects like quantum radiation reaction or multi-photon Breit-Wheeler pair production is described by the key parameter χ, which sets the field seen by a particle in its own rest frame in relation to the critical field of QED [see equation (2.5.1)]. It means that not only the field strength in the laboratory frame is important, but also the geometry of the interaction plays a crucial role. The easiest example is an ultra-relativistic electron with Lorentz factor γ_e propagating in the same direction as an ultra-intense laser pulse with electric field amplitude E_L. There, $\chi_e \simeq 1/(2\gamma_e)(E_L/E_{\mathrm{QED}})$ is relatively low. In the opposite case of counter-propagation, $\chi_e \simeq 2\gamma_e(E_L/E_{\mathrm{QED}})$ is much larger which is why head-on collisions of a laser beam with ultra-relativistic electrons are preferred in general. In addition to laser-electron collisions, the interaction of two [81] or even more colliding [82, 83] laser pulses with a target is investigated frequently. Such configurations have the advantage that particles always have a non-zero scattering angle with at least one laser pulse, with the result that QED effects are strongly enhanced. In this regard, these setups favor the development of QED cascades [84, 85] which in turn cause strong absorption of the initial laser energy by the generated electron-positron-photon plasma [74, 86]. It has also been shown that the collision of multiple

laser pulses lowers the threshold for pair production from vacuum [87]. Besides the enhancement of QED effects, the standing-wave structure emerging from the superposition of two (or multiple) counter-propagating waves allows the trapping of electrons at sufficiently high intensities induced by their radiation losses. Here, two different cases are usually distinguished[1]. First, one talks about normal radiative trapping when the particles get trapped in the spatially fixed nodes of the electric field [90]. This is possible in the standing wave generated by two laser beams when they are either linearly polarized along the same axis [91] or circularly polarized with opposite handedness [92]. Second, particles can also get trapped in the anti-nodes of the electric field, which is referred to as anomalous radiative trapping [93]. At this point, it should be stressed that, in contrast to normal radiative trapping, the anomalous trapping can only be observed in the case of linear polarization [94]. The origins for both trapping mechanisms have been studied recently. It has been found that normal radiative trapping is caused by the emergence of attractors in the particles' phase space as a consequence of radiation reaction [95, 96]. On the other hand, it has been suggested that anomalous radiative trapping is attributed to particles tending to move in a radiation-free direction [97].
In the following sections, the normal radiative trapping will be considered in more detail. In particular, special focus will be put on the questions how the electron-positron pairs created within the interaction and the spatial profiles of the colliding laser pulses affect the radiative trapping.

4.2 Influence of pair production on the radiative trapping

As mentioned in the introductory part, normal radiative trapping can be observed for linearly as well as for circularly polarized colliding laser waves. From here on, the radiative trapping will be illuminated in more detail for the latter. This, however, requires both waves to have opposite handedness since only in that case the standing wave can exhibit a spatially fixed node in the electric field. Therefore, the wave propagating in the positive x-direction has left-handed orientation and the other wave has right-handed orientation. It is noted that in the present thesis the handedness of a wave is defined from the point of view of the receiver. In this definition, the handedness coincides with the orientation of the screw formed in space by the electric (magnetic) field vector at a fixed moment in time. Then, neglecting in a first attempt any variations transverse to the propagation axis x, the carrier waves can be modeled by the following vector potentials

$$\begin{aligned} \mathbf{A}_1 &= A_0 \left[\cos\left(\omega_0 t - k_0 x\right)\hat{\mathbf{e}}_y + \sin\left(\omega_0 t - k_0 x\right)\hat{\mathbf{e}}_z\right], \\ \mathbf{A}_2 &= A_0 \left[\cos\left(\omega_0 t + k_0 x\right)\hat{\mathbf{e}}_y + \sin\left(\omega_0 t + k_0 x\right)\hat{\mathbf{e}}_z\right]. \end{aligned} \tag{4.2.1}$$

Here, k_0 and ω_0 are the wave number and angular frequency referring to a wavelength of $\lambda_0 = 1\ \mu\text{m}$, and A_0 is the amplitude. In the simulations discussed in the following, normalized peak values, $a_0 = eA_0/\left(m_e c^2\right)$, between $200/\sqrt{2}$ and $1500/\sqrt{2}$ are assumed, corresponding to peak intensities ranging from $I = 5.5 \times 10^{22}\ \text{Wcm}^{-2}$ to $I = 3.1 \times 10^{24}\ \text{Wcm}^{-2}$. Additionally, the waves in equation (4.2.1) are multiplied with a Gaussian time envelope of $e^{-(x-ct)^2/(2\tau^2)}$, where τ is chosen such that the pulses have a full-width-at-half-maximum duration of 20 fs. The two pulses illuminate a one-micron thick foil made of aluminum with initial electron density $n_e = 50 n_{\text{cr}}$ from both sides at normal incidence. The density is lower than the solid density

[1] For the sake of completeness, trapping of particles induced by radiation reaction has also been observed in the case of a traveling wave [88, 89].

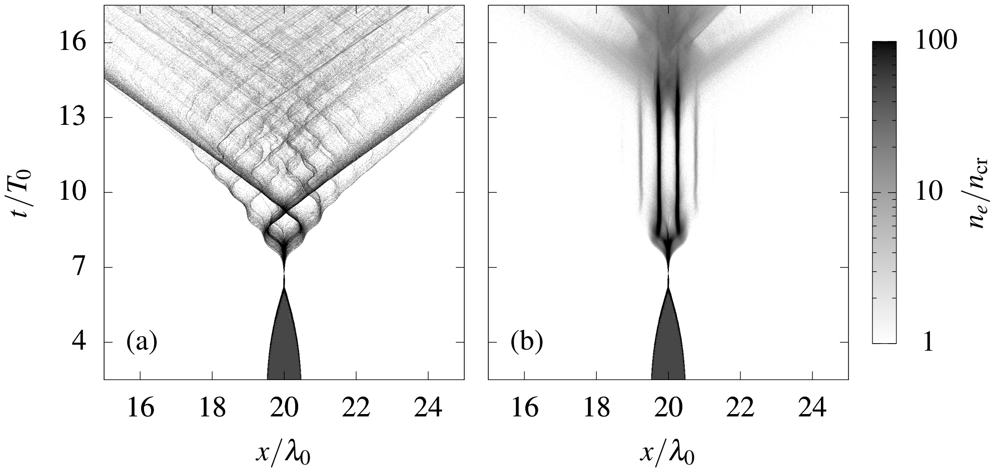

Figure 4.2.1: Space-time distribution of the electron density (a) without and (b) with taking into account QED effects for irradiating laser pulses with $a_0 = 500/\sqrt{2}$. Note that only densities above n_{cr} are plotted and that the color bar uses a logarithmic scale. Data published in [78].

of aluminum and can thus be fabricated, for instance, from aluminum foams. In actual fact, the exact ion species is of second rank as long as the ion mass-to-charge ratio is roughly two times that of protons[2]. This is the case for almost each fully ionized low-Z material as which (fully ionized) the target is assumed in the beginning. Physically, this is justified since the intensities of the two laser pulses are clearly above the barrier-suppression-ionization threshold of $I_{BSI} = 6.6 \times 10^{20}$ Wcm^{-2} for the most tightly bound electrons in aluminum [98].

From a numerical point of view, the simulation box has a dimension of $40\lambda_0$ along x with a cell size of $\Delta_x = \lambda_0/1000$. Initially, the plasma fills the area $19.5 < x/\lambda_0 < 20.5$ and gets represented by 100 macro-particles per species and cell. Both laser pulses are shifted such that they reach the center position $x_0 = 20\lambda_0$ at time $t = 10T_0$.

The effect of the radiative trapping is illustrated in figure 4.2.1, where one can see space-time distributions of the electron density; in one case without[3] [see figure 4.2.1(a)] and in the other case with accounting for QED effects [see figure 4.2.1(b)]. The other parameters are the same in both simulations, especially the dimensionless field amplitude of the irradiating laser pulses which is here $a_0 = 500/\sqrt{2}$. In the beginning, one can see that the inclusion of QED effects does not alter the dynamics drastically. In both cases, the interaction of the incident laser pulses with the plasma causes a piston-like push of the electrons, which leads to a symmetric compression of the foil from both sides. It is clear that at this stage QED effects are less important as the quantum parameter χ is low. This is basically due to electrons moving in the same direction as their driving laser pulse, so geometrically suppressing χ. The compression continues until the ponderomotive pressure exerted by the laser pulses is balanced by the pressure of the hot plasma. In the end, the foil is approximately compressed by a factor 100 to a width of $\lambda_0/100$ at time $t \approx 6.75T_0$, simultaneously increasing the density by the same factor. Until now, the electrons

[2] Additional simulations with protons give similar results. In conclusion, the results are not too sensitive with respect to the ion mass-to-charge ratio.

[3] It means that neither classical nor quantum radiation reaction is considered. Particles are solely pushed by the Lorentz force. Pair production is also not treated.

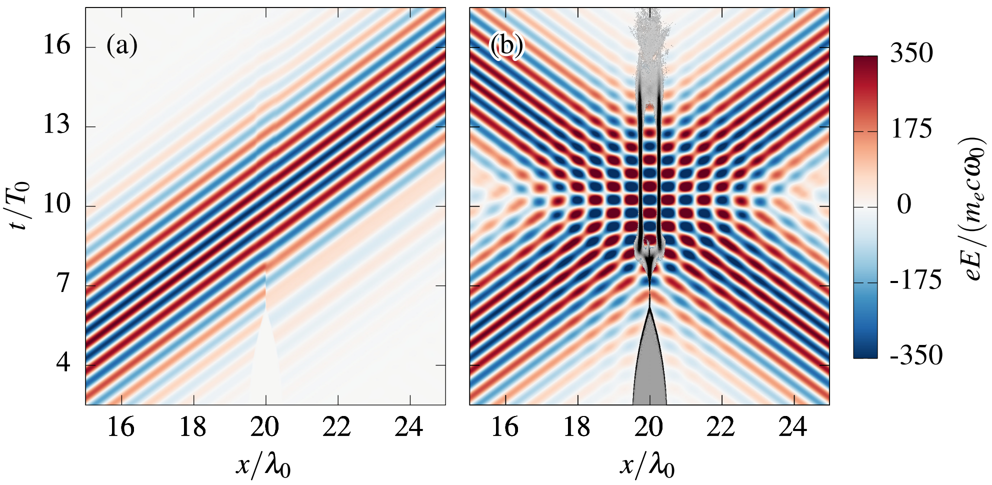

Figure 4.2.2: Space-time distribution of (a) the right-moving field component E_r [see the definition in equation (4.2.2)] and (b) the y-component of the electric field for the case where $a_0 = 500/\sqrt{2}$. In (b), the black part shows the electron density which exceeds $10n_{\mathrm{cr}}$ plotted on a linear color scale. Data published in [78].

have gained energies in the MeV range during the interaction with the laser pulses so that they are ultra-relativistic and rather inert. As a result, they cannot follow the driving wave oscillation, so that the plasma becomes relativistically transparent for the incident radiation. This can be nicely seen in a right-moving field component which is defined as

$$E_r = \frac{E_y + B_z}{2}, \tag{4.2.2}$$

and which can be found in figure 4.2.2(a). It can be retrieved that the plasma is opaque and reflects a large part of the incident radiation in the piston-like stage. During the subsequent stage of balance, one can observe that the fields on the left and on the right of the plasma equalize more and more and finally match at time $t \approx 7.5T_0$. Physically speaking, it means that the plasma becomes transmissive and, as consequence of this transparency, it emerges a transient standing wave [see figure 4.2.2(b)]. Based on equation (4.2.1) and supported by figure 4.2.2(b)[4], the standing wave exhibits nodes and anti-nodes in the electric field symmetrically around x_0 at

$$\frac{\xi_n - x_0}{\lambda_0} = \pm\frac{2n+1}{4} \quad \text{and} \quad \frac{\zeta_n - x_0}{\lambda_0} = \pm\frac{n}{2}, \tag{4.2.3}$$

respectively (n is an integer larger than or equal zero). In the case of the magnetic field, nodes and anti-nodes are swapped with respect to the electric field. The emergence of the transient standing wave, however, changes the plasma dynamics profoundly. For the pure classical simulation [see figure 4.2.1(a)], it seems that the ponderomotive pressure is no longer sufficient to confine the plasma and electrons are expelled from the center. It develops a dense jet of electrons on both sides of the former foil and these electrons co-move with the laser pulses outwards. The simulation with QED effects, in contrast, shows a different behavior [see figure 4.2.1(b)]. Although also showing a break of the strong confinement in the center, the electrons are afterwards not expelled far. On their way out of the center, the electrons collide with a counter-propagating laser pulse in a nearly head-on geometry. This enhances the χ parameter with the result that

[4] The z-component of the electric field reveals the same structure like E_y in figures 4.2.2(a) and (b).

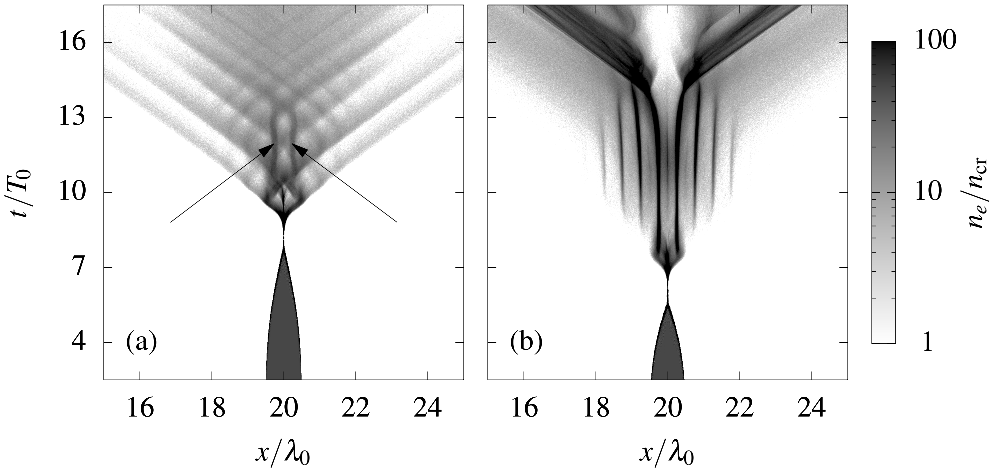

Figure 4.2.3: Space-time distribution of the electron density for irradiating laser pulses with dimensionless field amplitudes of (a) $a_0 = 200/\sqrt{2}$ and (b) $a_0 = 800/\sqrt{2}$. The two arrows in (a) are meant to highlight the fraction of trapped electrons. Only densities above n_{cr} are again shown [see figure 4.2.1]. Data published in [78].

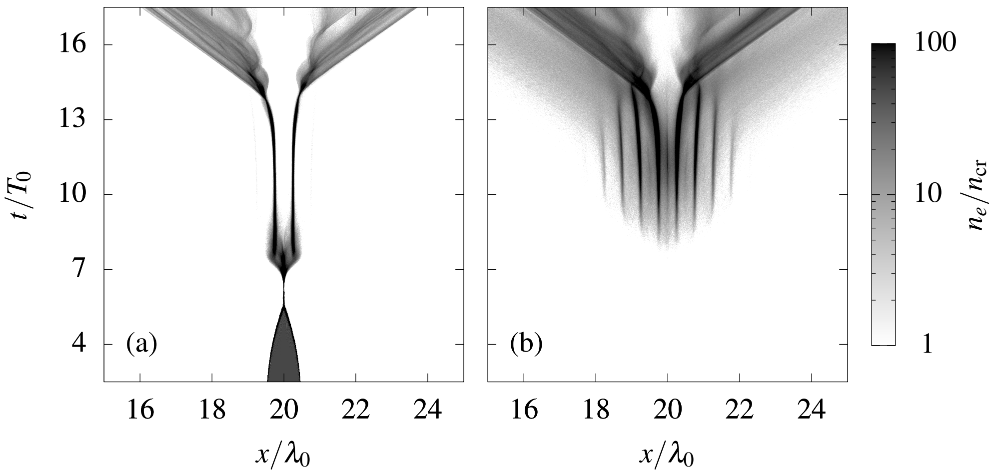

Figure 4.2.4: Space-time distribution of the electron density for irradiating laser pulses with dimensionless field amplitude of $a_0 = 800/\sqrt{2}$. More precisely, (a) shows the electrons from the foil and (b) the electrons resulting from Breit-Wheeler pair production. Data published in [78].

electrons suffer significant radiation losses. In fact, the radiation losses lead to the trapping of electrons in the nodes of the electric field which is emphasized in figure 4.2.2(b). The majority of electrons is trapped in the closest nodes of the electric field at $\pm\lambda_0/4$ to the center x_0, and only some electrons reach the trapping centers at $\pm 3\lambda_0/4$. The trapping is stable for almost six laser periods and stops approximately with the end of the laser pulse at time $t = 14.5T_0$. It is noted that 0.04 pairs per primary foil electron are produced for a normalized field amplitude of $a_0 = 500/\sqrt{2}$ at time $t = 15T_0$, implying that pair production is not of major importance for the temporal evolution of the system.

In order to study how this radiative trapping depends on the intensity and to find out when the production of electron-positron pairs becomes essential, further simulations with varying amplitudes are conducted. Figure 4.2.3 therefore presents the space-time distributions of the electron density for amplitudes of (a) $a_0 = 200/\sqrt{2}$ and (b) $a_0 = 800/\sqrt{2}$. First, one can see that the initial piston-like inwards push is comparable for all considered amplitudes. At this stage, differences can only be observed in the speed at which the foil is compressed. Higher intensities leads to a faster compression as one would expect intuitively. At later times, however, the dynamics is different. To concretize, the low-intensity simulation, $a_0 = 200/\sqrt{2}$, is reminiscent of a mixture of the simulations in figure 4.2.1(a) and (b) because it shows classical as well as QED features. For instance, one can see the formation of electron jets that are periodically expelled from the center. On the other side, there is already a fraction of electrons that is spatially confined in the zeroes of the electric field due to radiative trapping which is stressed by the two arrows in figure 4.2.3(a).

The high-intensity simulation, $a_0 = 800/\sqrt{2}$, shows much more pronounced patterns than could be observed in figure 4.2.1(b) for a dimensionless amplitude of $a_0 = 500/\sqrt{2}$. Here, even the fourth node of the electric field at $\pm 7\lambda_0/4$ around the center x_0 traps electrons very effectively. In the space between two adjacent nodes, in contrast to the case $a_0 = 500/\sqrt{2}$, the electron density does not drop to values of about zero and is rather smeared out. In addition, it is particularly worth mentioning that the density peaks in the middle of two nodes, which coincides with an anti-node of the electric field. These modifications in the laser–plasma dynamics can be ascribed to the increasing weight of the pair production process on the interaction. To demonstrate this, figure 4.2.4 shows the same simulation as figure 4.2.3(b), but makes a distinction between electrons from the foil [see figure 4.2.4(a)] and electrons originated from the Breit-Wheeler process [see figure 4.2.4(b)]. Already at first sight it is obvious that the density distributions for both *electron species* differ. For electrons originating from the foil the trapping resembles the case of $a_0 = 500/\sqrt{2}$ because these electrons are predominantly trapped in the closest node at $\pm\lambda_0/4$ to the center x_0. The number of trapped electrons in the next trapping node is visibly lower than before. This is related to the higher photon emission rate in the stronger field, which in turn reduces the radiation-free path and so results in a faster trapping of the foil electrons. Just the opposite can be seen in the distribution of the Breit-Wheeler electrons which mirrors the multifaceted patterns from figure 4.2.3(b) and so allows explaining their origin. The photons emitted by the foil electrons move ballistically through the standing-wave structure. If they are subjected to a sufficiently strong field, $\chi_\gamma \gtrsim 1$, they can decay into an electron-positron pair. Predominantly, this happens in the vicinity of maxima of the standing wave [92], which conforms to anti-nodes of either the electric or the magnetic field. In this sense, the density peak at the electric anti-node does not describe a proper radiative trapping by all means, but rather represents a point of efficient pair production. After their birth, electrons and positrons also suffer radiation losses in the standing wave with the result that they become trapped in the nodes of the electric field. On the way to the trapping node they contribute—together with pairs being created apart from the field maxima—to the aforementioned smearing effect of the particle density. Moreover, a closer look at the data exposes that the pair-electron density reaches the same order of magnitude as the foil-electron density in the most pronounced trapping center at $\pm\lambda_0/4$ and greatly exceeds it elsewhere. Simultaneously, the number of pairs per primary foil electron is enhanced considerably to 3.39 at time $t = 15T_0$. One can thus infer that the production of pairs gets increasingly dominant and will govern the temporal evolution of the entire system at some point. Indeed, this can be already observed in the same simulation run and is demonstrated by figure 4.2.5 which again shows the right-moving field component defined in equation (4.2.2). One can see that at about $t \approx 13T_0$ there is a change in the behavior of the E_r-field starting from the two electric

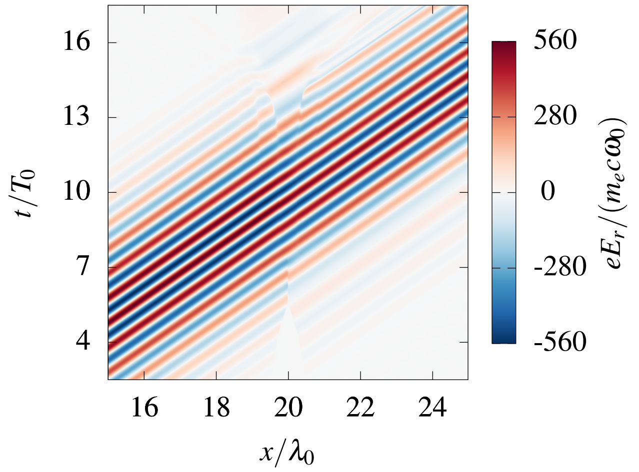

Figure 4.2.5: Space-time distribution of the right-moving field component E_r [see equation (4.2.2)] for irradiating laser pulses with dimensionless field amplitudes of $a_0 = 800/\sqrt{2}$. Data published in [78].

nodes at $\pm\lambda_0/4$ from x_0. Physically speaking, the reason for the change is the surpassing of the relativistically critical density by the combination of foil electrons and electron-positron plasma, which drastically alters the transparency properties and re-establishes the opacity of the plasma. Correspondingly, it comes to a break of the standing-wave structure before the end of the laser pulses. At the same time, the break of the standing wave is equivalent to the end of radiative trapping. This is confirmed by figures 4.2.4(a) and (b), where one can see that the electrons are deflected from the nodes after time $t \approx 13T_0$ and so earlier than for $a_0 = 500/\sqrt{2}$ [see figure 4.2.1(b)]. Additional simulations also suggest that the break of radiative trapping is shifted forwards in time when considering higher intensities. Lastly, the interpretation is also underlined by figure 4.2.6 which shows a simulation for $a_0 = 800/\sqrt{2}$ but without accounting for pair production. On that condition, the radiative trapping remains stable over the whole duration of the laser pulses. To conclude briefly, if one is particularly interested in studying the radiative trapping effect, one should consider moderate intensities where the trapping is most likely stable and not ruined by Breit-Wheeler pair production.

4.2.1 Multi-dimensional effects

In order to exclude that multi-dimensional effects impinge on the main physical conclusion drawn in the last section, two-dimensional simulations are presented subsequently. In these, the parameters like the dimension of the simulation box and grid steps are slightly adjusted such that the simulations become computationally practicable. To be exact, the box is $20\lambda_0$ long in the x-direction and also $20\lambda_0$ wide in the y-direction. The grid step is enlarged to $\Delta_x = \lambda_0/100$ along x, while it is laterally set to $\Delta_y = \lambda_0/20$. The target is still one micron thick and has a density of $50n_{\mathrm{cr}}$, but is now positioned around $x_0 = 10\lambda_0$. Dimensionless field amplitudes of $a_0 = 500/\sqrt{2}$ and $a_0 = 1200/\sqrt{2}$ are considered for the irradiating laser pulses. In the former case, the number of particles per cell and per species resolving the foil is again 100, while it is reduced to 5 in the latter. Transversely, the laser beams are characterized by a beam waist parameter of $w_0 = 2.5\lambda_0$, corresponding to a full width at half maximum spot size radius of 4.2 µm. The initial positions

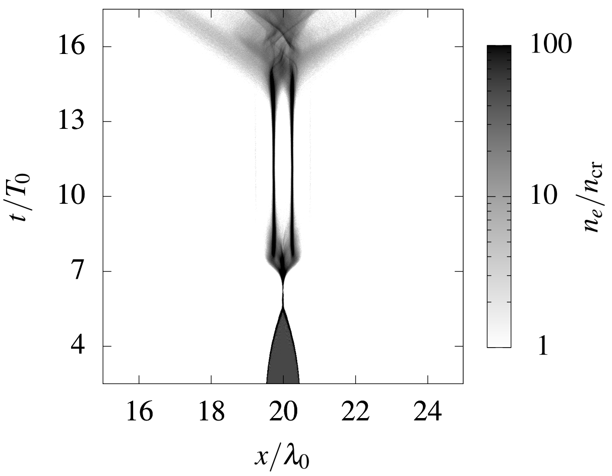

Figure 4.2.6: Space-time distribution of the electron density for irradiating laser pulses with dimensionless field amplitude of $a_0 = 800/\sqrt{2}$ when pair production is not taken into account. Data published in [78].

of the laser pulses are shifted such that they reach x_0 after ten or fifteen laser periods for the cases $a_0 = 500/\sqrt{2}$ and $a_0 = 1200/\sqrt{2}$, respectively.

Figure 4.2.7 shows a cross-section of the spatial distribution of [(a), (b)] the electron density and [(c), (d)] the B_z-field[5]. It should be further stressed that here the ordinate indeed stands for the transverse position and not for the time as in the last section and that the plots visualize a fixed moment in time, namely $1.18T_0$ (left column) and $1.6T_0$ (right column) after the peak intensities reached the center x_0. The plots on the left refer to the low-intensity case and the plots on the right to the high-intensity case. At first sight, figure 4.2.7(a) resembles the patterns obtained in the one-dimensional geometry for $a_0 = 500/\sqrt{2}$. Within the area of the focal spot, $|y| \lesssim w_0$, one can clearly see that most of the electrons are concentrated at $\pm\lambda_0/4$ around x_0, and only a minor part reaches $\pm 3\lambda_0/4$. In between, electrons are almost absent. The positions of the electron concentration coincide with the nodes of the electric field or with anti-nodes in terms of the magnetic field. This can be easily proven by a comparison with the B_z-field in figure 4.2.7(c). One can thus draw the first conclusion that multi-dimensionality does not alter the main properties of radiative trapping in a critical way.
Continuing with the high-intensity case, the density distribution of the foil electrons demonstrates that the behavior of the system undergoes a change [see figure 4.2.7(b)]. In principle, the foil electrons are mainly located in the nodes at $\pm\lambda_0/4$ to x_0. But it can be seen that for $|y| \lesssim 1.5\lambda_0$ these electrons are pushed inwards. The reason for that can be deduced from the z-component of the magnetic field which clearly reveals that the plasma is opaque in the center [see figure 4.2.7(d)]. The opacity of the plasma causes a break of the standing-wave structure which in turn leads to a piston-like push of the trapped electrons in the propagation direction of the driving laser pulse. In contrast, it seems as if the radiative trapping remains stable for $|y| \gtrsim 1.5\lambda_0$. This can be attributed to the transverse Gaussian profile of the laser beam. For larger y, the field is weaker than in the center with the result that pair production is less efficient. As a consequence, the relativistically critical density is not yet approached and the plasma remains

[5]It is noted that B_z is also divided by a_0 which simplifies the use of a single color bar scale for the two different cases.

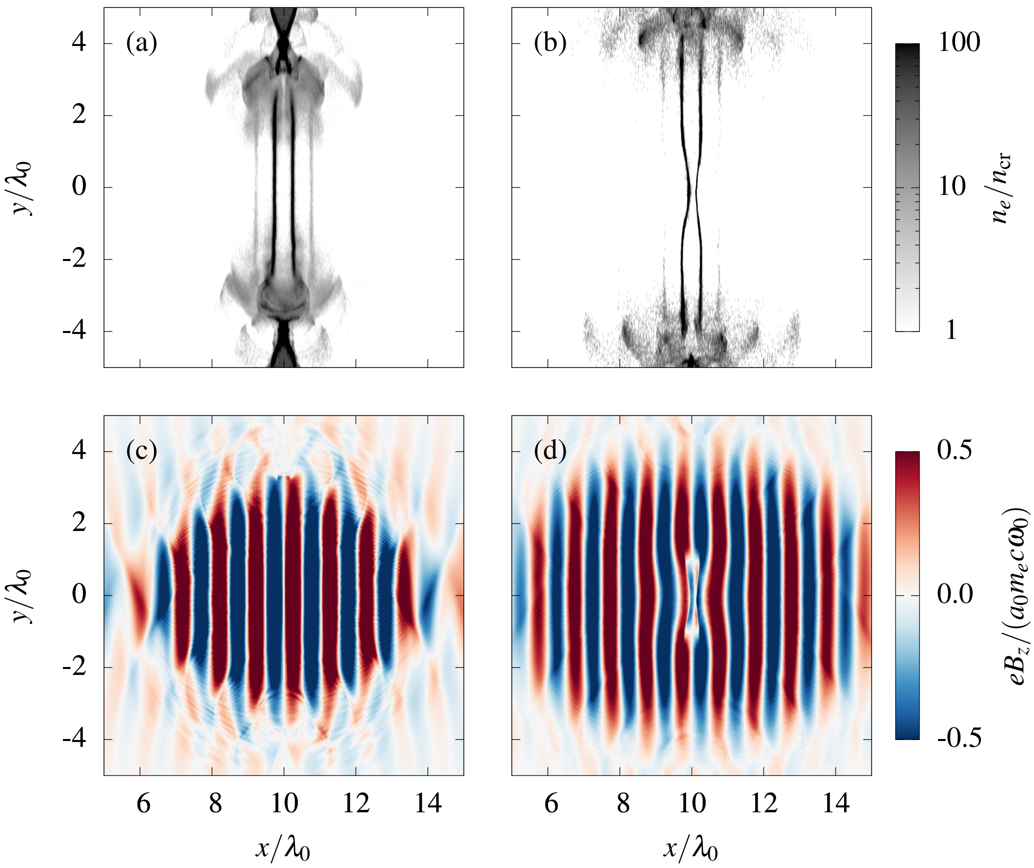

Figure 4.2.7: Results from two-dimensional simulations for the [(a), (b)] electron distribution and [(c), (d)] the magnetic B_z-field. The results in [(a), (c)] and [(b), (c)] belong to dimensionless field amplitudes of $a_0 = 500/\sqrt{2}$ and $a_0 = 1200/\sqrt{2}$, respectively. For reasons of visibility and comparability, it is noted that (b) shows only the distribution of foil electrons and that B_z is additionally divided by a_0. The data display the system $1.18T_0$ [(a), (c)] and $1.6T_0$ [(b), (d)] after the peak of each laser pulse reached the center position. Data published in [78].

transparent. In that sense, the standing wave and so the radiative trapping can be maintained for a longer time. The larger amplitude of the laser with respect to figure 4.2.7(a) additionally allows the trapping of electrons at larger lateral positions.

Recalling that the breakdown of radiative trapping sets in at an amplitude of approximately $a_0 = 800/\sqrt{2}$ in the one-dimensional geometry, it is shifted to higher amplitudes in the two-dimensional case. This can be easily understood when considering again the transverse profile of the laser beams. Though not leaving the trapping center longitudinally, electrons and positrons likely experience a ponderomotive push along the y-axis. Hence, the density in the trapping center does not rise as fast as in the one-dimensional case, in this way leading to a higher threshold intensity. Eventually, one can conclude that the break of radiative trapping is not affected by the multi-dimensional geometry, but on the other hand the intensity at which the break occurs has to be adjusted slightly.

4.3 Radiative trapping in the collision of twisted light pulses

The preceding section dealt with radiative trapping and its dependence on the pair production process. It was shown that above a certain threshold intensity the pairs are generated in such an enormous number that the plasma becomes opaque, causing the break of the standing wave and so of the radiative trapping. The following section picks up again on the radiative trapping, but illuminates it with particular regard to exotic properties of the irradiating laser pulses. These will be modeled as Laguerre–Gaussian beams which denote higher-order solutions to the paraxial wave equation in cylindrical coordinates. Fascinating about Laguerre–Gaussian modes is that they are supposed to carry a well-defined orbital angular momentum, which was first realized by Allen *et al.* almost three decades ago [99]. Since then, light carrying orbital angular momentum—sometimes also labeled with the prefix *twisted* or *vortex*—has gained a lot of interest in many areas of physics due to its potential for a wide range of applications. These applications cover the fields of optical microscopy [100, 101], optical manipulation on the micron scale [102, 103], quantum information [104, 105] and many more [106]. Usually, these applications work out at non-relativistic intensities. In fact, it is not standard practice in laboratories around the globe to provide twisted light with relativistic intensities. So far, there are only a couple of works that address appropriate mechanisms to change that. These include Raman amplification in plasma [107], the so-called light fan scheme [108], plasma surface holograms [109] and plasma volume holograms [110]. Fortunately, first demonstrations in experiments have been reported just recently [111, 112], which pave the way for twisted light–matter interactions in the relativistic regime. There, it is expected that twisted light enables the acceleration of hollow electron beams in laser-driven wakefields [113–115], of ions in ponderomotive beat waves [116], and even allows the laser-driven wakefield acceleration of positrons [117]. Twisted light also affects the generation of high harmonics in under- and over-dense plasma [118–120], preserves the spin polarization of wakefield-accelerated electrons [121], and is already considered in the QED regime [122, 123] with promising applications for the generation of twisted γ-rays [122–126].

The following section continues with a QED-relevant regime. The main setup remains unchanged with reference to section 4.2, now just assuming the collision of twisted light pulses. However, the fact that twisted light pulses carry orbital angular momentum requires simulations in a fully three-dimensional geometry. Numerically, the simulation box has a size of $20\lambda_0$ in the x-direction and $25\lambda_0$ in both transverse directions, divided into smaller cells of size $\Delta_x = 0.05\lambda_0$ and $\Delta_{y,z} = 0.075\lambda_0$. The one-micron thick foil is again located around $x_0 = 10\lambda_0$ while filling transversely the entire space. The initial electron density of the foil is still $50n_{\mathrm{cr}}$ and the ions now have a mass-to-charge ratio that is exactly two times that of protons. In the simulations, 10 macro-particles per cell and per species are used to resolve the target. The twisted light, which is impinging at normal incidence onto the foil's surface, is modeled as a circularly polarized Laguerre–Gaussian mode. Using cylindrical coordinates with x along the cylinder axis, $r = \sqrt{y^2+z^2}$ and $\varphi = \arctan(z/y)$, the transverse electric field profile can be written as [127]

$$\begin{aligned}\mathbf{E}_\perp = \pm\, & E_0 C_p^{|m|} \frac{w_0}{w(x)} \left(\frac{\sqrt{2}r}{w(x)}\right)^{|m|} L_p^{|m|}\left(\frac{2r^2}{w^2(x)}\right) \exp\left(-\frac{r^2}{w^2(x)} - \frac{(x-ct)^2}{2\tau^2}\right) \\ & \times \left[\sin\left(\omega_0 t \mp k_0 x \mp m\varphi + \phi_p^{|m|}(r,\,x)\right)\hat{\mathbf{e}}_y \mp s\cos\left(\omega_0 t \mp k_0 x \mp m\varphi + \phi_p^{|m|}(r,\,x)\right)\hat{\mathbf{e}}_z\right].\end{aligned} \tag{4.3.1}$$

Here, $C_p^{|m|}$ is a mode-dependent normalization constant defined such that E_0 describes the peak field, p is a natural number counting the zeros of the generalized Laguerre polynomial $L_p^{|m|}$, and

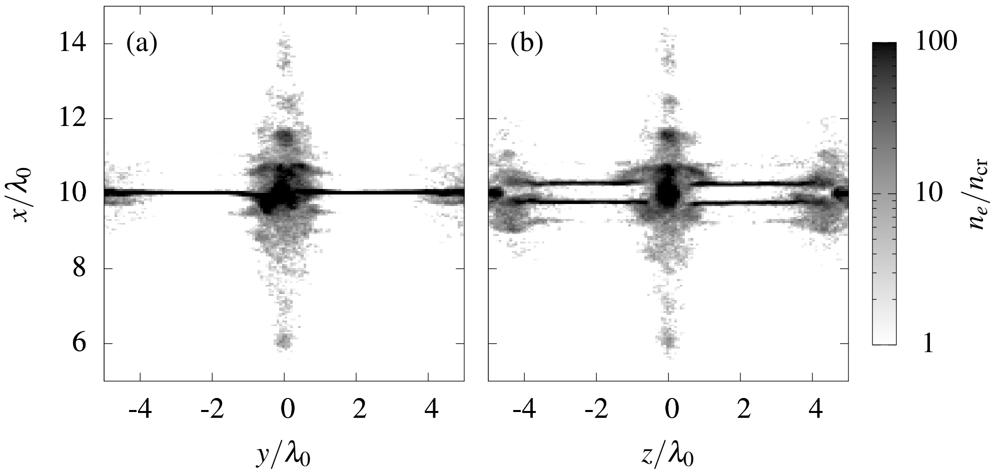

Figure 4.3.1: Electron distributions in the xy- and xz-plane at time $t = 10T_0$ for two colliding twisted light pulses ($a_0 = 500$) both with $m = -1$ but different handedness $s = +1$ (right-moving) and $s = -1$ (left-moving). Please note that, in contrast to figure 4.2.7, the longitudinal axis x is shown along the ordinate. Data published in [129].

$\phi_p^{|m|}$ is a space-dependent phase given by

$$\phi_p^{|m|}(r,\, x) = -\frac{k_0 r^2}{2R(x)} + (2p + |m| + 1)\arctan\left(\frac{2x}{k_0 w_0^2}\right). \tag{4.3.2}$$

The detailed shapes of the beam waist $w(x)$ and radius of curvature $R(x)$ are not of further interest, but can be found in [127]. It is also stressed that the different signs in equation (4.3.1) distiguish between right- and left-moving waves. In particular, the upper and lower sign represent the right- and left-moving wave in that order[6]. Moreover, m is an integer often called azimuthal index and s characterizes the handedness ($s = +1$ for left-handed and $s = -1$ for right-handed orientation). At this point, it is interesting to note that the azimuthal index m and the handedness s are closely related to the angular momentum of light. It is generally established that such a mode can be understood as a collection of photons each carrying an orbital angular momentum of $m\hbar$ and a spin angular momentum of $s\hbar$ along their direction of motion [128] (see also appendix A.2 for more information). Returning to the simulation parameters, both twisted light pulses have mode indices of $p = 0$ and $m = -1$[7]. The handednesses of the right- and left-moving pulse are $s = +1$ and $s = -1$, respectively. As previously, the full width at half maximum duration of the pulses is 20 fs and they have a minimal beam waist parameter of $w_0 = 2.5\lambda_0$ at the focus $x_0 = 10\lambda_0$. The peak intensity is $I = 6.86 \times 10^{23}$ Wcm^{-2} which is equal to a dimensionless field amplitude of 500. Section 4.2.1 showed that the threshold at which pair production alters the dynamics decisively is shifted to higher intensities in higher dimensions. The pair production module is therefore not included in the following simulations.

[6] This is the way the fields are modeled in the simulations.

[7] Modes with $p = 0$ and $m \neq 0$ are also referred to as donut modes because the field is zero on axis and non-zero off axis, making the (time-averaged) field distribution look like a donut.

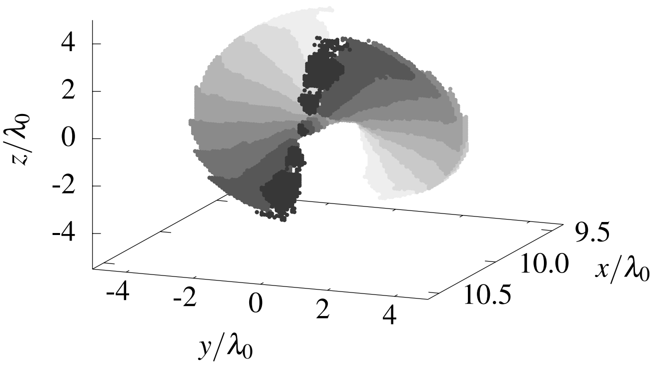

Figure 4.3.2: The plot shows the cells in the domain $9.75 < x/\lambda_0 < 10.25$ and $r/\lambda_0 < 4$ in which the electron density exceeds $150n_{\mathrm{cr}}$ at time $t = 10T_0$. The shading is meant to improve the visibility of the pattern and is performed according to the x-value of each cell. More precisely, darker shades of gray refer to larger values of x. See figure 4.3.1 for more information about the simulation parameters.

4.3.1 Impact of twisted light modes on the standing-wave structure

The initial stage of the interaction is almost identical to the previous case of non-twisted pulses. After the piston-like push in the beginning, the target becomes relativistically transparent for the incident laser pulses. In the subsequent stage, however, modifications can be observed in the interaction. Figure 4.3.1 shows the simulation results for the electron density in the xy- [see figure 4.3.1(a)] and xz-plane [see figure 4.3.1(b)] at time $t = 10T_0$. Already at first glance, one can see different patterns in the electron density distribution as compared with non-twisted pulses. First, one can observe in both cross sections that electrons accumulate at small lateral positions. This is due to the transverse field structure of a twisted beam which, in marked contrast to Gaussian beams, approaches zero in the center. As a consequence of this field minimum, electrons undergo a ponderomotive push to the center. Second, radiative trapping can still be identified in the electron distribution. Notably, the positions of the trapping centers in the xy- and xz-plane differ clearly from each other. While the electrons are trapped at $x = 10\lambda_0$ in the xy-plane [see figure 4.3.1(a)], they are mostly found at $x = 9.75\lambda_0$ and $x = 10.25\lambda_0$ in the xz-plane [see figure 4.3.1(b)]. In particular, the trapping position $x = 10\lambda_0$ in the xy-plane appears new. The asymmetry between the trapping in the xy- and xz-plane indicates that twisted beams generate a much more complex and multifaceted standing-wave pattern. In order to understand the trapping pattern in detail, figure 4.3.2 shows the distribution of cells in the volume $9.75 < x/\lambda_0 < 10.25$ and $r/\lambda_0 < 4$ in which the electron density exceeds $150n_{\mathrm{cr}}$ at time $t = 10T_0$ as a three-dimensional plot. The data are colored according to the x-position of the cells, namely darker shades of gray belong to larger values of x. At first glance, the distribution of cells looks like a ship's propeller. On closer consideration, one can indeed see that the cells are arranged on short sections of two distinct spirals. These spirals have right-handed orientation and their length is approximately $\lambda_0/2$. This suggests that in the present case of two counter-propagating twisted beams, both characterized by the same azimuthal index $m = -1$ but opposite handedness, the zeros of the electric field form a helical pattern. To check this, one starts with equation (4.3.1). There, particularly the oscillation term in the bottom line is responsible for the shape of the standing wave. For the y-components of the electric field, the contributing terms are given by

$$E_{y,1} \propto \sin(\omega_0 t - k_0 x + \varphi) \quad \text{and} \quad E_{y,2} \propto -\sin(\omega_0 t + k_0 x - \varphi). \tag{4.3.3}$$

The indices 1 and 2 label the right- and left-moving wave, respectively, and the proportionality factor is the same for waves 1 and 2. For completeness, it corresponds to the first line of equation (4.3.1) with the substitution $p = 0$ and $|m| = 1$. It is further noted that the additional phase from equation (4.3.1) is neglected because it is expected to be small in the vicinity of the focus, and thus is only of second rank for the structure of the standing wave. Then, the total electric field along y is the superposition of $E_{y,1}$ and $E_{y,2}$, which in the end can be expressed as

$$E_{y,1+2} \propto -2\cos(\omega_0 t)\sin(k_0 x - \varphi) \tag{4.3.4}$$

when using the addition theorems for trigonometric functions. By analogy, one finds for the z-component

$$\begin{aligned} E_{z,1+2} &\propto -\cos(\omega_0 t - k_0 x + \varphi) + \cos(\omega_0 t + k_0 x - \varphi) \\ &\propto -2\sin(\omega_0 t)\sin(k_0 x - \varphi). \end{aligned} \tag{4.3.5}$$

A subsequent comparison between equations (4.3.4) and (4.3.5) reveals that the total electric field has time-independent nodes which coincide with the zeros of $\sin(k_0 x - \varphi)$. Correspondingly, the argument has to be either 0 or π, yielding the two different solutions

$$k_0 x = \varphi \quad \text{and} \quad k_0 x = \varphi + \pi. \tag{4.3.6}$$

Manifestly, equation (4.3.6) describes two different spirals both having right-handed orientation as one can easily reconstruct. This is in agreement with the observations made in figure 4.3.2. The calculation regarding equation (4.3.6) also shows that the orientation of the helices is a direct consequence of the sign of the azimuthal index, so that one would expect left-handed spirals in the case of two twisted beams with $m = +1$. Apart from the aforementioned, one can deduce from equation (4.3.6) that the electric field is zero at $x = 10\lambda_0$ under azimuth angles of $\varphi = 0$ and $\varphi = \pi$, or at $x = (10 \pm 0.25)\lambda_0$ under azimuth angles of $\varphi = \pm\pi/2$. Fortunately, this yields the trapping centers observed in figure 4.3.1 from which follows that key features can be understood within a very simple model.

Simultaneously, it arises the question how changing, for instance, the sign of the azimuthal index of only one twisted beam modifies the radiative trapping. In doing so for the left-moving beam, the new superimposed total electric field is given by

$$\begin{aligned} E_{y,1+2} &\propto \sin(\omega_0 t - k_0 x + \varphi) - \sin(\omega_0 t + k_0 x + \varphi) \\ &\propto -2\cos(\omega_0 t + \varphi)\sin(k_0 x), \\ E_{z,1+2} &\propto -\cos(\omega_0 t - k_0 x + \varphi) + \cos(\omega_0 t + k_0 x + \varphi) \\ &\propto -2\sin(\omega_0 t + \varphi)\sin(k_0 x). \end{aligned} \tag{4.3.7}$$

One can see that under such circumstances the spatial structure of the electric nodes is more reminiscent of the trapping with non-twisted beams as one does not expect a trapping along a helical line. Instead, it is predicted that electrons are trapped around $x = 10\lambda_0$ for all azimuth angles φ. Eventually, this prediction is supported by a simulation of two counter-propagating twisted beams with opposite azimuthal indices (and opposite handedness) as can be seen in figures 4.3.3(a) and (b). One can see that the electrons are trapped at the same x-position in the xy- and xz-plane which is also in agreement with equation (4.3.7).

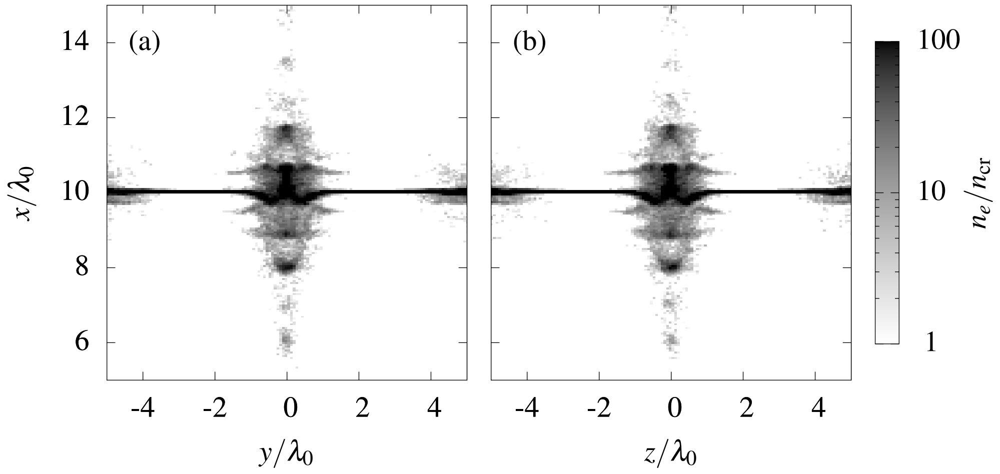

Figure 4.3.3: Electron distributions in the xy- and xz-plane at time $t = 10T_0$ for two colliding twisted light pulses ($a_0 = 500$) with $m = -1$ and handedness $s = +1$ (right-moving) and $m = +1$, $s = -1$ (left-moving). Data published in [129].

To conclude briefly, the structure of the trapping can be strongly modified by the presence of twisted beams. It was shown that helical trapping centers become possible. This, however, is only expected in the case of two counter-propagating twisted beams with the same azimuthal index m. In contrast, if the two colliding twisted beams have different azimuthal indices, the trapping is similar to non-twisted beams[8].

4.3.2 Generation of ultra-short electron patterns

The following subsection builds on two recent publications [129, 130] and has the intention to show that the setup can also be used to drive ultra-short electron patterns. These ultra-short patterns can either be disk-like electron bunches or helical electron beams. The emergence of these patterns is finally explained within a simple model.

The discussion starts with a look at figure 4.3.4 which shows the same simulation like figure 4.3.1 but four laser periods later in time[9]. One can see that the trapping of electrons already starts to dissolve because the end of the laser pulse duration is reached. The more interesting effect, however, can be observed for small lateral positions, $z/\lambda_0 < 2$. Here, electrons are released in regular distances from both sides of the target. At this point it is particularly noteworthy that the distribution of electrons during that release is different for electrons on the left and right of the target. While electrons are arranged on a single line on the right, they form two different lines on the left. Moreover, it seems as if these released electrons move in positive (on the right) and negative (on the left) x-direction. To get a clearer impression of the electron patterns, figure 4.3.5 gives a visualization of them in the three-dimensional space. To be more exact, figure 4.3.5(a) focuses on the electrons on the right by plotting all grid cells in the volume $10.5 < x/\lambda_0 < 15.5$

[8] More generally, one can observe helical nodes as soon as $m_1 + m_2 \neq 0$, where 1 and 2 subscript the two counter-propagating beams.

[9] As a reminder, the right-moving pulse has parameters $m = -1$ and $s = +1$, while the left-moving pulse has $m = -1$ and $s = -1$.

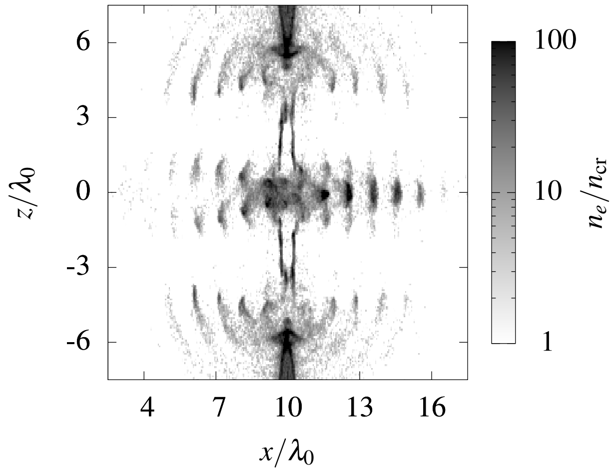

Figure 4.3.4: Electron distributions in the xz-plane at time $t = 14T_0$ for two colliding twisted light pulses ($a_0 = 500$) both with $m = -1$ but different handedness $s = +1$ (right-moving) and $s = -1$ (left-moving). Data published in [129].

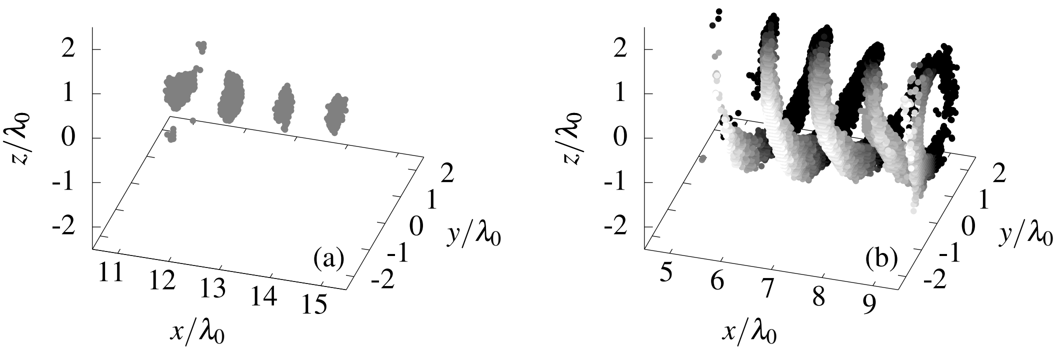

Figure 4.3.5: The plots show the cells in the volume (a) $11 < x/\lambda_0 < 15$ and $r/\lambda_0 < 1.5$, (b) $4.5 < x/\lambda_0 < 9.5$ and $0.75 < r/\lambda_0 < 1.5$ in which the electron density exceeds (a) $50n_{\mathrm{cr}}$, (b) $10n_{\mathrm{cr}}$ at time $t = 14T_0$. The shading in (b) is meant to improve the visibility of the pattern and is performed according to the y-value of each cell. Darker shades of gray refer to larger values of y. See figure 4.3.4 for more information about the simulation parameters. Data published in [129].

and $r/\lambda_0 < 1.5$ which host electrons densities above $50n_{\mathrm{cr}}$. Under these conditions, it becomes evident that a train of disk-like electron bunches is released from the target. The bunches are thereby well-separated longitudinally with a regular spacing of one laser wavelength λ_0 (see also figure 4.3.6) and tightly compressed in the transverse direction. In particular the clear longitudinal separation in combination with the spacing of λ_0 suggests that all the bunches have a length significantly shorter than λ_0. In fact, a longitudinal cut of the electron density through the center of the bunches depicts that the bunches have full width at half maximum lengths down to approximately $\lambda_0/4$ (see figure 4.3.6). Expressed in terms of time, the electron bunches have an

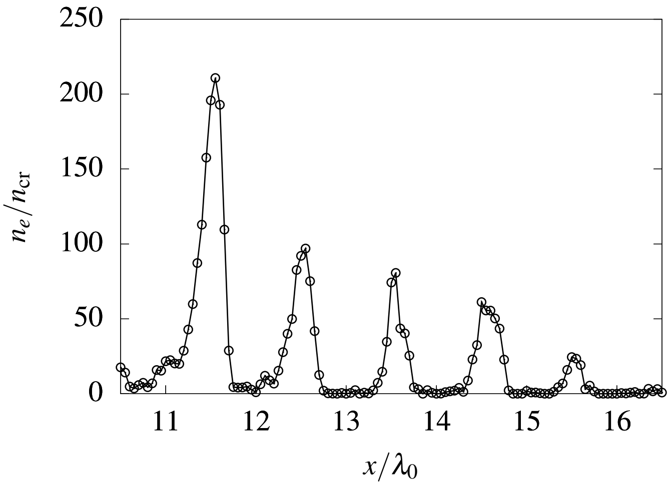

Figure 4.3.6: Cut of the electron density along the x-axis for fixed lateral positions $y = z = 0\lambda_0$. See figure 4.3.4 for the simulation parameters. Data published in [129].

ultra-short duration of ≈ 830 as, which potentially makes them interesting for a wide range of applications in the attosecond sciences [14]. Beyond to their ultra-short duration, these bunches also have extraordinarily high densities. For instance, it can be seen that the lastly released bunch at $x \approx 11.55\lambda_0$ has a density of roughly $200n_{\mathrm{cr}}$. Bunches that were released earlier have lower densities, which indicates that the bunches disperse slightly in the transverse direction with evolving time, but their density still remains high though.
Returning to the discussion about the electron patterns in the three-dimensional space, one might naively expect two laterally displaced trains of disk-like electron bunches when looking at figure 4.3.4 with the knowledge of figure 4.3.5(a). In reality, the electron pattern on the left is completely altered with respect to the right. This is illustrated in figure 4.3.5(b) which plots all grid cells in the volume $4.5 < x/\lambda_0 < 9.5$ and $0.75 < r/\lambda_0 < 1.5$ in which the electron density exceeds $10n_{\mathrm{cr}}$. Rather than seeing laterally displaced disk-like electron bunches, one can observe that the electrons are distributed on helical patterns instead. More detailed, one can identify two different helices on which the electrons are arranged when taking a closer look. Both of the two helices have right-handed orientation and twist around the x-axis with a period of $2\lambda_0$. The longitudinal separation between the two neighbored helices turns out to be λ_0 (see also figure 4.3.4). Likewise to the bunches, these helical electron patterns are also characterized by ultra-short durations on the attosecond timescale. In the end, it is noted that similar electron patterns have been reported in recent works about the interaction of circularly polarized Laguerre–Gaussian beams of relativistic intensity with several targets, ranging from nanorods [131, 132] over microdroplets [133] to under-dense plasma slabs [134].

To summarize the key features discussed so far: On the target's right, a train of disk-like electron bunches is generated. Conversely, two helical electron beams are excited on the left. Recalling that the right- and left-moving laser beams have mode parameters $m = -1,\ s = +1$ and $m = -1,\ s = -1$, respectively, this gives the impression that the electron patterns can be understood with the help of the total angular momentum per photon, $j = m + s$. This quantity differs for the two laser beams and is equal to $j = 0$ (right-moving) and $j = -2$ (left-moving). In order to understand the connection with the generated electron patterns in detail, the phase of the electric field turns out to be helpful. The focus is first laid on the electric field of only beam which propagates in positive x-direction for the sake of simplicity. Thereby, $p = 0$ is the only mode parameter that is fixed, while m and s are variable to generalize the discussion as much as possible. In addition, the geometry suggests the expression of the electric field in terms of its radial and azimuthal components. These can be determined from the Cartesian components according to the transformation rule

$$E_r = E_y \cos(\varphi) + E_z \sin(\varphi) \quad \text{and} \quad E_\varphi = E_z \cos(\varphi) - E_y \sin(\varphi). \tag{4.3.8}$$

Inserting the expressions for E_y and E_z from equation (4.3.1) and concentrating on the phase dependence, one arrives at

$$\begin{aligned} E_r &\propto \sin\left(\omega_0 t - k_0 x - j\varphi \ + \phi_p^{|m|}(r,x)\right), \\ E_\varphi &\propto -s\cos\left(\omega_0 t - k_0 x - j\varphi \ + \phi_p^{|m|}(r,x)\right), \end{aligned} \tag{4.3.9}$$

after making use of $s = \pm 1$ and the addition theorems for trigonometric functions. It can be seen that the index j appears in the radial and azimuthal electric field components. Even the calculation of the laser's electric field along the propagation direction yields a similar phase dependence (see appendix for the details of the calculation). As a result, the field has a unique dependence on a single phase which makes an interpretation of the emerging electron patterns feasible. At first, consider a non-zero j and neglect again the phase $\phi_p^{|m|}(r,x)$ as it varies marginally for distances not far (with respect to the Rayleigh length) from the focus. Then, one can see that for each fixed longitudinal position x there are j angles φ at which the electric field has the same phase at time t. When such a laser phase is appropriate, electrons can be captured and co-move with the driving laser pulse for rather long times [135, 136]. This phase capture is likely responsible for the emergence of $|j|$ helical electron orbits. As all electrons on such a helix are caught in the same phase, one can easily deduce further characteristics like orientation of the spiral or the spacing between neighbored spirals. For this purpose, consider a fixed moment in time. It thus requires

$$k_0 x + j\varphi = \text{constant} \tag{4.3.10}$$

to stay in the same phase. This describes a spiral whose orientation is determined by the sign of j. For $j > 0$, one needs to rotate around a negative angle φ in order to compensate for a phase increase caused by incrementing x. This is equivalent to a left-handed screw. Oppositely, $j < 0$ results in a screw with right-handed orientation. Further, one can see that the electric field has a spatial period of $j\lambda_0$ along the propagation axis x. Since $|j|$ helical patterns appear in total, the spacing between two adjacent spirals is λ_0. The above mentioned confirms the observations from figures 4.3.4 and 4.3.5(b), where the twisted light beam with $j = -2 < 0$ excited two intertwined spirals with right-handed orientation, each with a period of $2\lambda_0$ and a spacing of λ_0 along the longitudinal axis[10]. The generation of a single and a triplet helix is shown in [130] at a moderately relativistic intensity of $I = 2.47 \times 10^{21}$ Wcm^{-2} ($a_0 = 30$) for the case $|j| = 1$ and $|j| = 3$.

The case $j = 0$ is slightly different as the phase is completely independent of the azimuth angle φ. Correspondingly, electrons with any angle φ can get phase-locked at a proper position x. This explains the disk-like structure of the electron bunches. The absence of φ in the phase further implies the period of the bunches to be same as the usual period of a traveling wave, namely λ_0. This is exactly the longitudinal spacing of two disk-like electron bunches, as seen in figures 4.3.4 and 4.3.5(a).

[10] It is noted that the findings can be directly applied to a left-moving pulse though the discussion refers to a right-moving pulse. This is due to the fact that the handedness of a screw—which is defined by the signs of m and s—is the same for left- and right-moving waves.

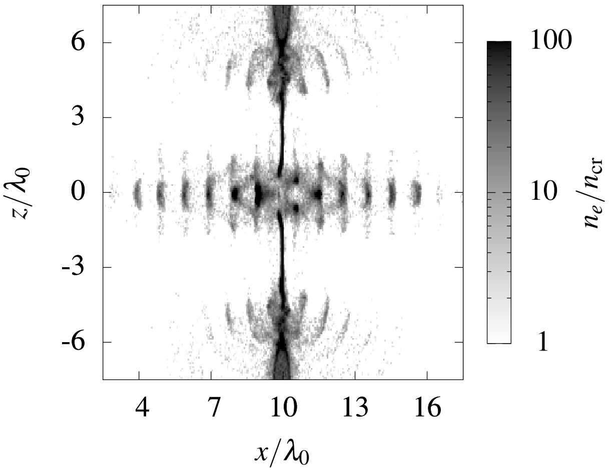

Figure 4.3.7: Electron distributions in the xz-plane at time $t = 14T_0$ for two colliding twisted light pulses ($a_0 = 500$) with $m = -1$ and handedness $s = +1$ (right-moving) and $m = +1$, $s = -1$ (left-moving). Data published in [129].

To demonstrate the applicability of the phenomenological explanation once more, a simulation is conducted in which only the azimuthal index of the left-moving beam is changed in sign ($m = +1$). As a consequence, j is zero for both the right- and the left-moving twisted pulse. Hence, one expects the generation of a train of disk-like electron bunches on both sides of the target. This is indeed what can be retrieved from the simulation data (see figure 4.3.7). One can see that the pattern on the left hand side of the target is modified and now also indicates a train of electron bunches. It should be emphasized that a change of the left-moving laser beam parameters leads to a change of the electron patterns on the target's left. This is a nice indicator for the plasma transparency induced within the interaction. The electron beams driven by circularly polarized Laguerre–Gaussian laser beams thus have the potential to represent a diagnostic tool for the optical properties of plasmas interacting with laser radiation of ultra-high field strengths.

4.4 Summary

In summary, this chapter dealt with the normal radiative trapping effect, which describes a trapping of electrons in the nodes of the superimposed electric field of at least two counter-propagating laser pulses induced by radiation losses. In the first part of the chapter (see section 4.2), the trapping was thoroughly investigated with special regard on how it behaved when the peak intensity of the irradiating laser pulses got continuously increased. Supported by PIC simulations in a one-dimensional geometry, it was shown that the trapping breaks down above a certain intensity. This could be ascribed to the increasing weight of the pair production process on the dynamics. Namely, at some point the density of generated pair plasma got so high that the plasma changed its optical properties and became opaque for the incident radiation. This caused a break of the standing wave with the result that also the trapping disappeared. It was further shown that multi-dimensional effects did not impact the main conclusion decisively, but led to a higher threshold up to which the trapping could survive.

In the second part of the chapter (see section 4.3), the radiative trapping was considered from the perspective of realizing it with exotic light. This was achieved by two counter-propagating and circularly polarized Laguerre–Gaussian laser beams. Generally, Laguerre–Gaussian laser modes are known to carry orbital angular momentum proportional to their azimuthal index m. It was found that the trapping pattern might change profoundly. Interestingly, one could observe that the electrons got trapped along helical patterns when the azimuthal indices of both counter-propagating laser pulses were equal to $m = -1$. Conversely, as one index was changed to $m = +1$, the trapping became more reminiscent of the case of non-twisted beams. Analytically, the structure of the trapping patterns was brought in connection with the electric field nodes which also forms helical or non-helical patterns depending on the value of the azimuthal indices.
As a side effect, it could be observed that circularly polarized twisted light beams allow the laser-driven excitation of either disk-like electron bunches or helical electron beams. Whether the electrons got excited as bunches or helical beams was determined by the total angular momentum carried by a laser photon, $j = m + s$. If $j = 0$, one will observe bunches, otherwise, one will see $|j|$ helical electron beams. In the latter case, the orientation of the electron spiral was given by the sign of j. Impressively, both bunches or helical beams were characterized by durations on the attosecond scale. This potentially makes them promising for a wide range of applications.

5 Approaching highly supercritical regimes of strong-field QED

The preceding chapter discussed the normal radiative-trapping effect in the standing wave transiently generated by two counter-propagating and circularly polarized laser pulses. In that scenario, the quantum nonlinearity parameter χ of electrons and photons doubtlessly approached and surpassed unity. This led to efficient pair production and finally to the break of the radiative trapping effect above a certain intensity threshold. However, χ was likely below the order of 10. In the now coming chapter, in contrast, much more extreme conditions will be addressed. It will be shown that in the midterm future χ values above 1000 might be in reach. As will be explained, this requires the interaction time between electrons and fields to be ultra-short. The main purpose of the chapter at hand is thus the demonstration how to create experimental configurations in which such ultra-short interaction times are possible.

5.1 Introduction

Quantum electrodynamics is one of the most successfully tested theories in physics. In the strong-field regime, however, it has been only possible so far to probe the theory in the regime $\chi \lesssim 1$ with optical laser pulses as, for instance, in the seminal E-144 experiment at the Stanford Linear Accelerator Center (SLAC) in the United States [137, 138] or in two recent experiments with the Astra-Gemini laser of the Central Laser Facility at the Rutherford Appleton Laboratory in the United Kingdom [19, 20]. Using the strong fields in aligned crystals serves as a good alternative to laser-based setups [139, 140]. There, $\chi \approx 7$ has been achieved in an experiment at CERN in the Switzerland [141]. In nature, however, it assumed that much more extreme conditions can occur. Particularly in astrophysical environments such as magnetized neutron stars, supercritical magnetic fields defined by $B \gg B_{\text{QED}}$ are present [142, 143]. Apparently, a reproduction of such conditions on earth would allow a deeper understanding of astrophysical objects. Though rapid progress in technology, reaching supercritical fields directly in the laboratory is still far beyond current capabilities. In combination with ultra-relativistic particles, however, one can boost to supercritical fields in the proper reference frame of the particle. Note that the field seen by such a particle is most likely not of magnetic type. The physics is thus complementary to pure supercritical magnetic fields, but especially important with regard to the upcoming high-intensity experiments at various facilities [21–23]. Going over to even higher fields, radiative corrections are expected to become more and more important. Physically speaking, this means that the emission of virtual photons by ultra-relativistic particles and the temporary conversion of a high-energy photon into a virtual electron-positron pair contribute significantly to the rate of the QED processes. As these radiative corrections grow unusually fast in the presence of a strong background field (see, for instance, [144, 145]), it was already conjectured in the 1970s by Ritus and Narozhny [146, 147]—and revisited by Fedotov in 2017 [148]—that a perturbative consideration of these loop corrections breaks down if $\alpha\chi^{2/3} \gtrsim 1$, and hence at $\chi \gtrsim 1600$. Correspondingly, QED becomes a fully non-perturbative and strongly coupled theory[1]. In fact, recent works have refined that the power-law scaling of the loop corrections, which is the reason for the conjectured breakdown of perturbation theory, can strictly speaking only be observed in the case of a constant-crossed field [149, 150]. As noted in section 2.5.1, ultra-relativistic particles see any field in the high-intensity limit as a constant-crossed field, and this class of background field is also essential for the application of the Monte-Carlo algorithm (see section 3.3). This implies that as long as the underlying approximations are justified, the QED-PIC method allows investigating the *power-law* regime.

The regime $\alpha\chi^{2/3} \gtrsim 1$ is barely studied at present and has only regained attraction in the last couple of years. One of the main reasons for missing studies is the assumption of the community that the regime is far beyond experimental reach, and therefore there is no urgent need for detailed analyses. This follows mainly from the ultra-fast time which characterizes the radiation losses in such extreme environments. In this regard consider an ultra-relativistic electron initially located outside a strong field. While approaching the strong field the electron is forced to emit high-energy photons. This can lead to significant radiation losses which reduce the energy of the electron and, as a consequence, also the value of the quantum nonlinearity parameter χ_e[2]. It is therefore necessary that the switching time of the electromagnetic background field is smaller than or at least comparable to the radiation time t_{rad} in order to mitigate radiation losses of the electron, and so to approach the highly supercritical regime. As noted in section 3.3, the radiation time can be identified with the inverse of the photon emission rate [see equations (2.5.6) and (2.5.7)]. In the case that the electrons are subjected to supercritical fields ($\chi_e \gg 1$), one finds

$$t_{\mathrm{rad}} = W_{\mathrm{rad}}^{-1} \simeq \left(1.46\,\frac{m_e c^2}{\hbar\gamma_e}\,\alpha\chi_e^{2/3}\right)^{-1}, \tag{5.1.1}$$

which reduces to[3]

$$t_{\mathrm{rad}} \sim \gamma_e\,\tau_C \tag{5.1.2}$$

in the regime $\alpha\chi_e^{2/3} \gtrsim 1$. Here $\tau_C = \hbar/\left(m_e c^2\right) = 1.3\times 10^{-21}$ s is the reduced Compton time. The minimum duration τ_L of a laser pulse is restricted to the laser period T_L, and hence to the femtosecond scale since high intensity laser systems operate at optical frequencies ($T_L \sim 3$ fs). Resulting from that, electron energies in the multiple-TeV range $\left(\gamma_e \sim 10^6\right)$ are necessary to boost t_{rad} to the femtosecond level. Such lepton energies are more than one order of magnitude beyond the energies that are currently attainable with standard linear accelerators. At SLAC, for instance, experiments with 46.6 GeV electrons were conducted in the 1990s [137, 138], and it was even possible to accelerate electrons up to a maximum energy of 85 GeV when combined with a plasma acceleration stage in 2007 [151]. At the Super-Proton-Synchrotron North Area facility at CERN, single electrons and positrons with energies of ≈ 100 GeV are available in the H4 beam line [139, 152]. Because of all that, one can conclude that the collision of ultra-relativistic electrons and clean optical laser pulses is not promising for probing the highly supercritical regime. Possible alternatives therefore demand finding experimentally acceptable configurations at a lower energy scale, most likely at the 100 GeV level. Obviously, this scale

[1]It is noted that in the following the expressions fully non-perturbative regime, $\alpha\chi^{2/3} \gtrsim 1$, and highly supercritical fields (regime) will be used interchangeably.

[2]The index e means that an electron or a positron is considered. If the index is γ, then a photon will be addressed. In the case of a missing index, χ is not restricted to a specific species.

[3]Note that numerical factors of the order of unity have been omitted.

has the advantage that it is already practicable at CERNs North Area facility [152]. Moreover, it is also worth mentioning that there is already a plan for the realization of a new linear accelerator operating at the 100 GeV level, termed as the *International Linear Collider* (ILC) [153]. For 100 GeV electrons, $\chi_e = 1600$ requires at least intensities of $I \simeq 3.7 \times 10^{24}$ Wcm^{-2}, which are, in principle, predicted by upcoming laser facilities [21–23]. These laser pulses, however, are too long because the radiation time drops to values of approximately $t_{\text{rad}} \simeq 200$ as $< \tau_L$. At this point, there are basically two distinct ways how to handle that time constraint: First, one can think about other sources of strong electromagnetic fields apart from optical laser radiation, like for example high-current particle beams. The length of a particle beam is not limited to (wave)lengths on the micron scale, so allowing sub-femtosecond switching times of the field. Additionally, the strength of the field can be controlled by the carrier current and the transverse size. And second, one can think about mechanisms that structure the optical laser radiation in such a way that the interaction time between the particle and the field is reduced to a minimum. As will be discussed in the next sections, one can find feasible experimental configurations for both approaches.

5.2 Non-perturbative QED collider

The presentation of experimentally feasible configurations starts with the non-perturbative QED collider as recently proposed by Yakimenko *et al*. [154]. Figure 5.2.1 gives a sketch of the scheme. The proposal pursues the collision of two 100 GeV-class electron (or positron) beams of appropriate current and size in order to reach the fully non-perturbative QED regime. Since the regime of interest is extreme, so are the parameters of the particle beams. How the parameters have to be chosen in detail is discussed in the following by estimating the self-generated field surrounding an ultra-relativistic beam.

5.2.1 Parameters of the collider

The profile of the ultra-relativistic beam is assumed Gaussian-like in all directions. The resulting charge density ρ of the beam can then be written as

$$\rho = q_e n_0 \exp\left(-\frac{r^2}{2\sigma_r^2}\right) \exp\left(-\frac{(x-vt)^2}{2\sigma_x^2}\right). \tag{5.2.1}$$

Here q_e denotes the charge of the particle species ($q_e = -e$ for electrons and $q_e = e$ for positrons), v is the velocity of the beam particles ($v \simeq c$), n_0 is the peak particle density, σ_r is the rms width and σ_x corresponds to the rms length (or duration) of the beam. The charge distribution in equation (5.2.1) generates both an electric field and a magnetic field as the charges propagate almost at the speed of light. In order to estimate the self-fields analytically, it is reasonable to switch for the calculation into the rest frame of the beam[4] since there the field is purely electrostatic, $\mathbf{E}' \neq 0$ and $\mathbf{B}' = 0$. Naturally, the origin of the primed coordinate system is put into the center of the beam, where $x' = r' = 0$. For reasons of symmetry, it is also obvious that the maximum of the field is located somewhere in the plane $x' = 0$. The geometry further suggests

[4] All primed quantities refer to the frame of reference in which the beam is at rest.

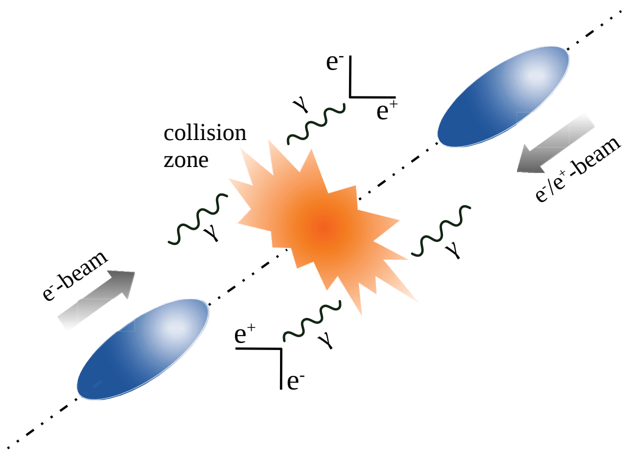

Figure 5.2.1: Schematic of the non-perturbative QED collider as proposed by Yakimenko *et al.* [154]. The two colliding beams are supposed to have unique properties: ultra-short duration (rms length $\sigma_x = 10\,\mathrm{nm}$), tight focus (rms width $\sigma_r = 10\,\mathrm{nm}$), high peak current ($I_{\max} = 1.7\,\mathrm{MA}$), and high energy ($\varepsilon_e = 125\,\mathrm{GeV}$). Figure published in [154], © 2019 American Physical Society, reproduced with permission, all rights reserved.

the electric field to be purely transverse in that plane, $\mathbf{E}' \equiv \mathbf{E}'_\perp$. It is then possible to find an expression for the electric field $\mathbf{E}'$ in the central plane directly from Gauss law

$$\int_{\partial V'} \mathbf{E}' \cdot \mathrm{d}\mathbf{A}' = 4\pi \int_{V'} \rho' \mathrm{d}V'. \tag{5.2.2}$$

The evaluation of equation (5.2.2) finally yields

$$\mathbf{E}'_\perp = \frac{4\pi\sigma_r^2 n'_0 q_e}{r} \exp\left(-\frac{x'^2}{2\sigma_x'^2}\right)\left[1-\exp\left(-\frac{r^2}{2\sigma_r^2}\right)\right]\hat{\mathbf{e}}_r, \tag{5.2.3}$$

where $n'_0 = n_0/\gamma_e$ is the peak density in the rest frame of the beam. In the next step, the inverse Lorentz transformation gives the electromagnetic field in the laboratory frame. At this point, it is important to stress that any longitudinal electric field component that may arise in the rest frame of the beam is strongly suppressed with respect to the transverse field for 100 GeV-class electrons, $|\mathbf{E}_\parallel| \simeq |\mathbf{E}_\perp|/\gamma_e$. Putting all together, the self-generated field can be approximated as

$$\begin{aligned}\mathbf{E} &= \frac{4\pi\sigma_r^2 n_0 q_e}{r} \exp\left(-\frac{(x-vt)^2}{2\sigma_x^2}\right)\left[1-\exp\left(-\frac{r^2}{2\sigma_r^2}\right)\right]\hat{\mathbf{e}}_r,\\ \mathbf{B} &= \frac{4\pi\sigma_r^2 n_0 q_e}{r}\frac{v}{c} \exp\left(-\frac{(x-vt)^2}{2\sigma_x^2}\right)\left[1-\exp\left(-\frac{r^2}{2\sigma_r^2}\right)\right]\hat{\mathbf{e}}_\varphi.\end{aligned} \tag{5.2.4}$$

Since $v \approx c$ for $\gamma_e \gg 1$, the electric and magnetic field are approximately equal in magnitude, $|\mathbf{E}| \simeq |\mathbf{B}|$. It is also noteworthy that an ultra-relativistic particle beam generates a crossed field, $\mathbf{E} \perp \mathbf{B}$.

To estimate the beam parameters required to approach the highly supercritical regime, it is reasonable to introduce the peak current related to the beam. The calculation can be performed straightforwardly and gives $I_{\max} = 2\pi\sigma_r^2 q_e n_0 c$. In this manner, the prefactor in equation (5.2.4) can be rewritten as $(2I_{\max})/(cr)$, which stresses a close relationship to the field of a normal axialsymmetric wire. It can be seen that the field vanishes on the symmetry axis $(r = 0)$ and scales as r^{-1} for $r \gg \sigma_r$. In between, the (electric) field reaches a maximum strength at approximately $r_{\max} \simeq 1.59\sigma_r$ which is given by $E_{\max} \simeq (0.9I_{\max})/(c\sigma_r)$. Under the assumption of counter-propagating beams, one can relate the ratio $I_{\max}/\sigma_r$ to the maximum value of the quantum nonlinearity parameter via [see equation (2.5.1)]

$$0.9\,\gamma_e \frac{I_{\max}}{\sigma_r} \simeq \frac{e\chi_e}{2\tau_C r_e}, \tag{5.2.5}$$

where $r_e = e^2/\left(m_e c^2\right)$ is the classical electron radius. To further advance the estimation of the beam parameters, one has to ensure that the interaction time is shorter than the radiation time t_{rad}. This is ensured when the total emission probability $\mathscr{P}$ is less than unity. Recalling equation (5.1.1), this leads in the limit $\alpha\chi_e^{2/3} \simeq 1$ to the condition

$$\mathscr{P} = \frac{\sigma_x}{\gamma_e c \tau_C} \lesssim 1 \tag{5.2.6}$$

for a Gaussian longitudinal profile with duration σ_x/c. In order to guarantee a controlled interaction between two colliding beams, it is important that the beams are not distorted too much during the collision. The emerging disruption is measured by the dimensionless parameter D which quantifies the deflection of a particle resulting from the interaction with the self-fields of an opposing beam. In particular, low values of D are equivalent to small disruption, and thus are beneficial for a controlled collision [155]. For an axialsymmetric Gaussian beam, D can be expressed as [155–157]

$$D = \sqrt{2\pi}\,\frac{r_e}{ec}\,\frac{I_{\max}\sigma_x^2}{\gamma_e\sigma_r^2}. \tag{5.2.7}$$

Combining the scaling equations (5.2.5),(5.2.6), and (5.2.7) yields the estimate for the beam parameters σ_x, σ_r, and $I_{\max}$ in terms of the constraining parameters $\chi_e, \mathscr{P}, D$, and γ_e:

$$\sigma_x = \gamma_e \mathscr{P} c\tau_C, \quad \sigma_r \sim \sqrt{\frac{\pi}{2}}\,\frac{\mathscr{P}^2\chi_e}{D}\,c\tau_C, \quad \text{and} \quad I_{\max} \sim \sqrt{\frac{\pi}{8}}\,\frac{\mathscr{P}^2\chi_e^2}{\gamma_e D}\,\frac{ec}{r_e}. \tag{5.2.8}$$

Setting $\chi_e = 1600$, $\gamma_e = 2\times 10^5$ (100 GeV), $\mathscr{P} = 0.1$, and $D = 0.001$ (low disruption) finally gives

$$\sigma_x \sim 10\ \mathrm{nm}, \quad \sigma_r \sim 10\ \mathrm{nm}, \quad \text{and} \quad I_{\max} \sim 1.5\ \mathrm{MA}. \tag{5.2.9}$$

This is the natural scale of parameters allowing the study of non-perturbative QED with a 100-GeV-class electron-electron collider in the low disruption limit. The parameters of the non-perturbative QED collider differ significantly from other proposed colliders such as ILC [153] or the Compact Linear Collider (CLIC) [158].

5.2.2 Applicability of the QED-PIC method

In order to emphasize the potential for reaching highly supercritical regimes with colliding high-current lepton beams, PIC simulations are performed with the code `VLPL`. Please note that the use of the PIC simulation technique has several advantages with respect to other codes that are frequently used to investigate beam-beam collisions in the high-energy-physics community (see, for instance, the codes CAIN [159] and GUINEA-PIG [160]). In particular, the most important advantage of PIC simulations is that they are fully electromagnetic. Charged particles are pushed according to the local electromagnetic field and act subsequently as source for new electromagnetic fields in Maxwell's equations. This self-consistent approach is thus capable of simulating beam-beam collisions more accurate as changes to the fields, either due to the creation of electron-positron pairs or to large disruption, are taken into account properly.

As described in section 3.3.1, the incorporation of QED effects into PIC codes requires the locally constant field approximation to be applicable. Correspondingly, the formation length for any QED process has to be smaller than the variation length of the field. In supercritical fields ($\chi_e \gg 1$), the formation length for a QED process behaves like $l_f \sim \gamma_e \lambda\!\!\!^{-}_C/\chi_e^{2/3}$ which gives $l_f \sim 0.7$ nm for the aforementioned beam parameters. Apparently, l_f is much smaller than the scale of the field variation $\sigma_x = 10$ nm. In addition, the two Lorentz-invariant field parameters f and g are supposed to be small with respect to unity, $f, g \ll 1$ [see equation (2.5.3)], in order to apply the QED rates in a constant-crossed field[5]. An evaluation of f and g is again relatively easy in the rest frame of one beam, where the field is purely electrostatic (see also the discussion in the previous section). From $g \propto \mathbf{E}' \cdot \mathbf{B}'$ [see equation (2.5.3)], it then follows directly that g is equal to zero. By analogy, f is only determined by the electric field,

$$f = \frac{\mathbf{E}'^2}{E_{\text{crit}}^2}. \tag{5.2.10}$$

Considering now a probing electron from the opposing beam in the current frame of reference. There, it has a normalized energy of $\gamma_e' \simeq 2\gamma_e^2$ and a quantum nonlinearity parameter of $\chi_e = (\gamma_e' |\mathbf{E}_\perp'|)/E_{\text{crit}}$. Note that χ_e is Lorentz-invariant and therefore it is expected to be large, $\chi_e \gg 1$. With regard to f this means that

$$f = \frac{\mathbf{E}'^2}{E_{\text{crit}}^2} = \frac{\mathbf{E}_\perp'^2}{E_{\text{crit}}^2}\frac{\mathbf{E}'^2}{\mathbf{E}_\perp'^2} = \frac{\chi_e^2}{\gamma_e'^2}\frac{\mathbf{E}'^2}{\mathbf{E}_\perp'^2} \simeq \frac{\chi_e^2}{\gamma_e'^2}. \tag{5.2.11}$$

In the last step, it was used that the ratio of $\mathbf{E}'^2$ and $\mathbf{E}_\perp'^2$ gives a factor of the order of unity. One then has for head-on collisions $f \ll 1 \ll \chi_e^2$ as $1 \ll \chi_e \ll \gamma_e \ll \gamma_e'$. In that sense, the use of the QED-PIC approach is justified for the proposed setup.

Finally, it must be emphasized that the following simulation results are only correct up to the point at which the theory might break. However, the main intention of this chapter is to demonstrate a reasonable path towards fully non-perturbative QED. Moreover, the Nikishov–Ritus theory also helps in identifying the impact of high-order radiative corrections from experimental data, as will be discussed in chapter 6.

5.2.3 Results

The concept of the non-perturbative QED collider is finally demonstrated for two colliding electron beams with rms width $\sigma_r = 10$ nm, rms duration $\sigma_x = 10$ nm, peak current $I_{\max} = 1.7$ MA,

[5]In principle, it is also necessary that $f, g \ll \chi_e^2$. However, under the assumption of $\chi_e \gg 1$, this will always be valid if $f, g \ll 1$.

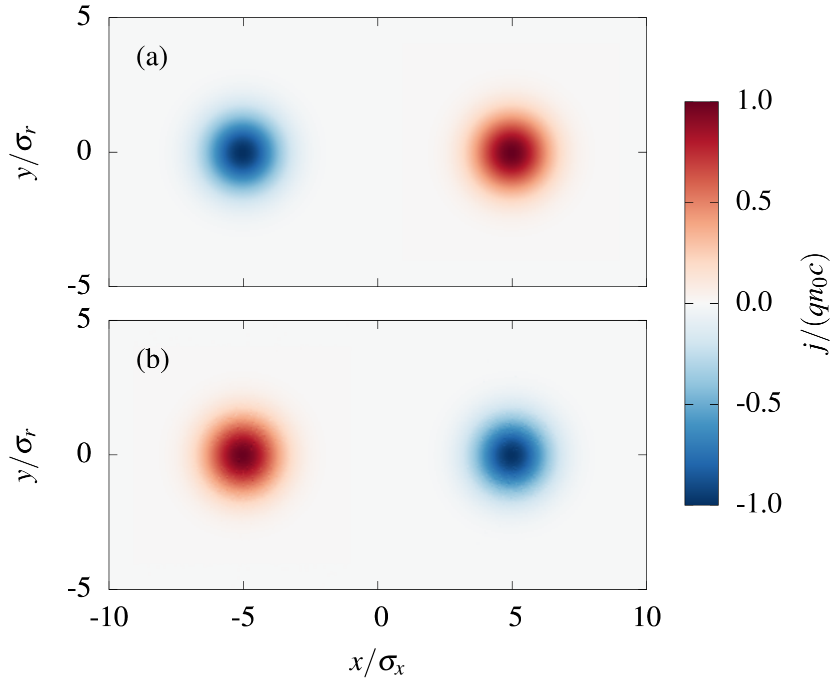

Figure 5.2.2: Plot of the two colliding electron beams in the xy-plane (a) before and (b) after the collision.

and a normalized energy per particle of $\varepsilon_e/\left(m_e c^2\right) = 2.5 \times 10^5$. The three-dimensional simulation domain is divided into smaller grid cells of size $0.05\,\sigma_x \times 0.05\,\sigma_r \times 0.05\,\sigma_r$. Both electron beams are assumed Gaussian-like as noted in equation (5.2.1)[6]. The peak density is calculated such that it matches the peak current $I_{\max}$. In the beginning of the simulation, the electromagnetic field of each beam is initialized with the help of equation (5.2.4), which is a good approximation for the real field distribution of a relativistic charged beam. The centers of the two beams are shifted by $10\,\sigma_x$ in the longitudinal direction, and both beams are represented by 8 macro-particles per cell.

Figure 5.2.2 shows a plot of the two colliding electron beams in the xy-plane before [see subplot (a)] and after the collision [see subplot (b)]. The beams are visualized through their corresponding charge density $j = \pm\rho c$, where the different signs indicate the different propagation directions. Particularly, the positive sign describes the electron beam propagating along the positive x-axis and the other way around for the negative sign. It can be nicely seen that the spatial shape of the particle distribution does not change significantly during the collision. The reason for that is low the disruption parameter of $D \approx 0.001$ in the above simulation which reduces a defocusing of the two electron beams, and so enables a highly controllable interaction.

The main intention of the collider design is the demonstration of its potential for approaching highly supercritical fields with high-current lepton beams of nanometer dimensions. Indeed, figure 5.2.3 corroborates the feasibility. Here the quantum nonlinearity parameter χ_e of the electron beam moving in the positive x-direction is plotted in different planes at the moment in time when the two beams overlap completely. For instance, figures 5.2.3(a) and (b) show the maximum value of χ_e in each simulation cell, once in a longitudinal plane [see subplot (a)] and the

[6] Based on computational reasons it should be stressed that the beams are cut longitudinally at $\pm 4\,\sigma_x$ and radially at $4\,\sigma_r$ around their center.

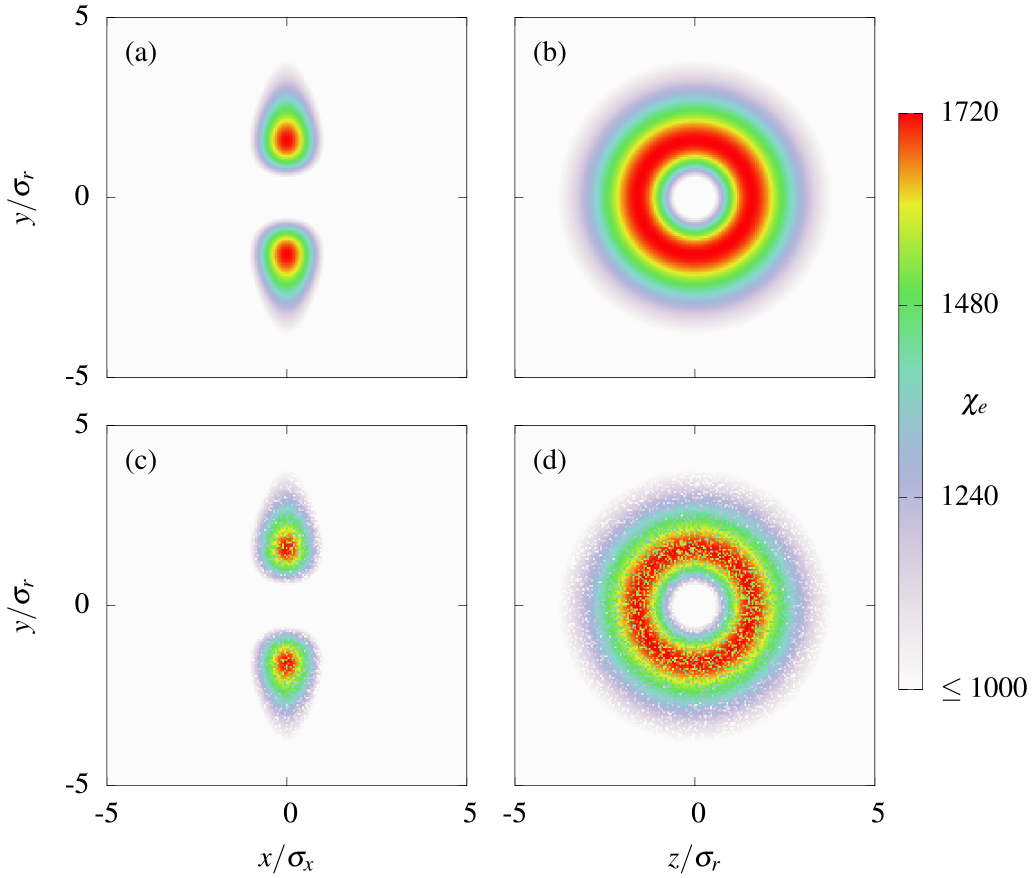

Figure 5.2.3: Plot of the [(a), (b)] maximum and of the [(c), (d)] averaged χ_e parameter in each simulation cell when both beams completely overlap. The subplots show a cut in the [(a), (c)] xy- and in the [(b), (d)] transverse plane. The data refer to the beam propagating along the positive x-axis. Note also that only values above $\chi_e = 1000$ are shown.

other time in the transverse plane [see subplot (b)]. As only values of χ_e surpassing 1000 are shown, one can directly see that supercritical regimes of the light-matter interaction could be reached. Besides, it should be clear that the specifically observable patterns of χ_e are closely related to the structure of the field. From the axial symmetry of the field, it follows that χ_e decreases for small radii $r \ll \sigma_r$ and approaches zero in the center. This can be also seen in figures 5.2.3(a) and (b)[7], and leads to a donut-shaped distribution of χ_e in the transverse plane. As discussed previously, the field reaches its maximum value at $r_{\mathrm{max}} \simeq 1.59\sigma_r$ which is simultaneously expected to be the region of the largest χ_e. This can be confirmed by the simulation data which further predict $\chi_e^{\mathrm{max}} \simeq 1719$, being also in agreement with equation (5.2.5). One can also see that the longitudinal extent of high χ_e values is smaller than the transverse extent. This is due to the field structure being different in both directions. Along the transverse axes the field shows a much slower decrease, namely only a $1/r$-dependence, in comparison with a Gaussian scaling longitudinally.

[7]Note that the simulation data indeed show that χ_e is zero in the center.

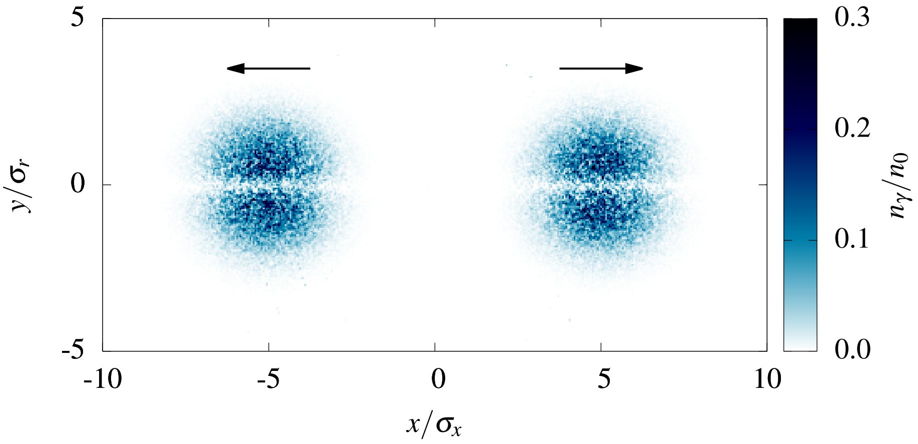

Figure 5.2.4: Plot of the generated photon beams in the xy-plane after the collision of the two high-current electron beams. The two black arrows indicate the direction of propagation of each photon beam.

The maximum value of χ_e is an important quantity because it shows that the collider design as such is a promising configuration for studies on non-perturbative QED. It lacks, however, information about how many particles in a specific region are actually in the interesting regime. It is therefore valuable to have an additional look at the averaged value of χ_e in each simulation cell. In the following the average is determined from

$$\chi_e^{\text{avg}}\big|_{\text{cell}\,j} = \frac{1}{N_j} \sum_{i \in \text{cell}\,j} w_i \chi_{e,i} \quad \text{with} \quad N_j = \sum_{i \in \text{cell}\,j} w_i. \tag{5.2.12}$$

Here the sum runs over all macro-particles that are in cell j and w_i is the weight of the i-th macro-particle. The results are shown in figure 5.2.3(c) and (d), again divided into a plot in a longitudinal plane [see subplot (c)] and in the transverse plane [see subplot (d)]. In general, one can see that the main patterns are the same. It is especially remarkable that χ_e exceeds 1600 even in the average in many cases. One can, however, notice that the plot does not show a continuous behavior as before. There are randomly distributed cells in which the averaged χ_e parameter drops to values being significantly lower compared to adjacent cells. This observation is a consequence of the emission of high-energy photons by some ultra-relativistic electrons which leads to a decrease in the electron energy and in the χ_e parameter accordingly. On the other hand, the random character can be ascribed to the stochastic nature of the employed Monte-Carlo routine. To quantify how much χ_e is modified in total by the photon emissions, it is helpful to calculate the averaged χ_e parameter of the entire beam, and to compare it afterwards with the average under the assumption that no photon emission takes place. In the latter case, one can use the value of χ_e^{max} for all macro-particles in the specific cell. The calculation yields roughly 962 when including photon emission and otherwise 1003. It means that the parameter is altered by approximately -4.1%.

Photon beams

In the following, the emitted photons will be addressed in more detail. This has basically two reasons. First, the photons represent a potentially measurable observable which can give mean-

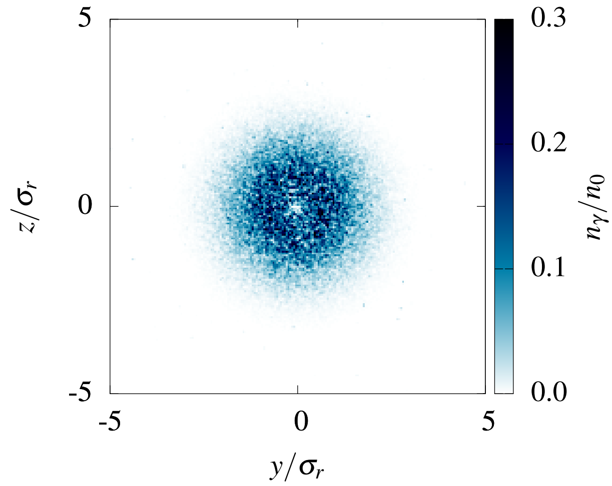

Figure 5.2.5: Transverse characterization of the photon beam that propagates in the positive x-direction ($x = 5\,\sigma_x$) after the collision of both high-current electron beams.

ingful information about the physics of the collision. An in-depth characterization may thus be of particular interest from an experimental point of view. Second, the collision of lepton beams is a longstanding research topic and one can find a lot of literature about it. The work by Yokoya and Chen [161] is worth mentioning at this point, as they derived estimates for the number of photons emitted in a linear electron-electron collider. This finally allows a direct comparison of the simulation results with the literature.

Figure 5.2.4 illustrates a density plot of the emitted photons in a longitudinal plane after the collision of the two electron beams. It is obvious that the interaction generates two spatially separated photon beams. The two photon beams propagate in opposite directions which is indicated in the figure by two black arrows. Though the photons accompany their parent electron beams, it should be stressed that they are mainly generated during the interaction with the field of the opposing beam. Besides, one can see that the photon density is low in the center ($y = 0\,\sigma_r$) which is based on the linear scaling of the field with the radius for $r \ll \sigma_r$. This can be also observed in figure 5.2.5, where a density plot of the forward moving photon beam is shown in the transverse plane at $x = 5\,\sigma_x$. In principle, the plot depicts that the qualitative behavior is comparable to χ_e. A detailed analysis, however, reveals the maximum photon density to be located at smaller radii with respect to χ_e, namely at $r \approx 0.7\sigma_r$. The reason therefor is that χ_e can be seen as a *single macro-particle* quantity, i.e. it is calculated once for a macro-particle and so independent of the macro-particle weight. The photon distribution, in contrast, depends explicitly on the density of the emitting particles. In the present configuration, the maxima of the field and the electron beam density are laterally displaced. The maximum of the transverse photon distribution is thus set by the product of the photon emission probability and the electron density. In supercritical fields, the former scales as $\chi_e^{2/3}$ [or as the transverse field to the power of $2/3$, see equation (5.2.4)] and the transverse density profile according to equation (5.2.1). Following this line of argument, one obtains a maximum at $r \simeq 0.71\sigma_r$ which nicely matches the simulation data.

To advance the investigation of the emitted photons, one should have a look at their energy spectrum as it is likely serves an important observable. The final spectrum after the interaction is shown in figure 5.2.6 as a dual logarithmic plot. Remarkably, in this way of plotting the spectrum follows a linearly decreasing trend almost over the entire energy range plotted (1.25 MeV $< \varepsilon_\gamma <$

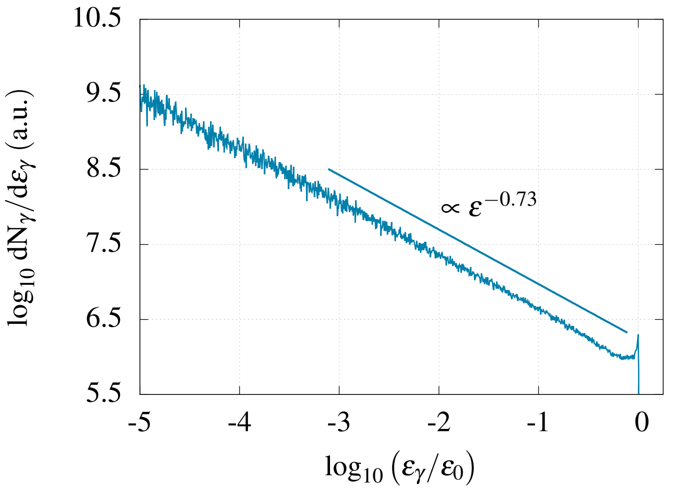

Figure 5.2.6: Log-log plot of the fully developed photon spectrum (blue). The linear scaling indicates that the spectrum obeys a power-law decrease. A power-law index of $p \simeq 0.73$ is obtained when fitting the data to a linear function in the range $100\ \mathrm{MeV} < \varepsilon_\gamma < 100\ \mathrm{GeV}$.

125 GeV). Nevertheless, it is surprising that the spectrum behaves conversely at high photon energies instead. Before the rough cut-off at the electron beam energy ε_0, it emerges a bump in the spectrum. Although the bump appears counter-intuitively, it is indeed physically correct and can be ascribed to the QED photon emission rate. Its discussion, however, will be postponed to the following chapter 6. Recalling the linear part of the spectrum, it means from a physical point of view that the spectrum obeys a power-law behavior, $\mathrm{dN}_\gamma/\mathrm{d}\varepsilon_\gamma \propto \varepsilon_\gamma^{-p}$, with p being the power-law index. Note that in the dual logarithmic plot, the power-law index is equal to the slope of the linear function. It is therefore relatively easy to determine its value numerically, for instance, by fitting a linear function to the data. In doing so, the `gnuplot` fitting routine predicts a value of $p \simeq 0.73$ for the data in the energy interval $100\ \mathrm{MeV} < \varepsilon_\gamma < 100\ \mathrm{GeV}$. The linear fit is marked in figure 5.2.6 as the (shifted) blue line.

As already mentioned, it is possible to compare the simulation results with appropriate literature [161]. The parameter of interest is either the total number of photons normalized with the initial number of electrons in the parent beams or the relative energy loss of electrons due to photon emission. Subsequently, the notation of the accelerator physics community is adopted, where it is common to classify the impact of strong-field QED processes in terms of the beamstrahlung parameter Υ. This parameter is closely related to the quantum nonlinearity parameter χ_e used in the strong-field QED community. More precisely, the beamstrahlung parameter can be regarded as the value of χ_e averaged over the beam profile, $\Upsilon = \chi_e^{\mathrm{avg}}$. In the case of Gaussian beams, it is possible to calculate Υ analytically, with the result being equal to

$$\Upsilon = \frac{5}{12} \frac{N_{e_0^-} \alpha \gamma_e \lambda_C^2}{\sigma_r \sigma_x}. \tag{5.2.13}$$

Here, $N_{e_0^-}$ stands for the total number of electrons in the beam. For the set of parameters given above, the beamstrahlung parameter equals approximately $\Upsilon \simeq 1000$ and is thus much larger than unity[8], $\Upsilon \gg 1$. It is then possible to estimate the amount of secondary photons that are generated

[8]Noteworthy, Υ coincides with the numerically averaged value of $\chi_e^{\max}$ over the beam profile (see the discussion on page 54), so strengthening its interpretation as an average of χ_e over the beam profile.

within the collision, and one finds for the normalized number per primary beam particle

$$\frac{N_\gamma}{N_{e_0^-}} \simeq 2.57 \left(\frac{\sigma_x}{\gamma_e \lambda_C} \, \alpha \Upsilon^{2/3} \right) \tag{5.2.14}$$

in the limit $\Upsilon \gg 1$ [161][9]. The emission of photons is accompanied by a reduction of the beam particle energy. In the average, the relative energy loss is given by [161][10]

$$\frac{\Delta \varepsilon_e}{\varepsilon_e} \simeq -0.689 \left(\frac{\sigma_x}{\gamma_e \lambda_C} \, \alpha \Upsilon^{2/3} \right). \tag{5.2.15}$$

Inserting the collider parameters gives $N_\gamma / N_{e_0^-} \simeq 0.194$ and $\Delta\varepsilon_e/\varepsilon_e \simeq -0.052$, which is in agreement with the simulation results of $N_\gamma / N_{e_0^-} \simeq 0.205$ and $\Delta\varepsilon_e/\varepsilon_e \simeq -0.050$ obtained with the code `VLPL`.

Electron-positron beams

On their ballistic motion through space, a great majority of the photons is transiently subjected to extreme fields, $\chi_\gamma \gtrsim 1$. This opens the possibility for the creation of copious electron-positron pairs (see figure 5.2.7). In particular, the longitudinally summed (pair) electron [see subplots (a) and (b)] and positron densities [see subplots (c) and (d)] are denoted in black and orange, respectively. The two plots on the left-hand side illustrate the pair yield at the collision time. One can see that the pair distributions resemble the transverse photon distribution as expected (see figure 5.2.5). In addition to that, no significant difference between the electron and positron distribution is visible. This changes profoundly within the course of the collision as can be seen in the plots on the right [subplots (b) and (d)]. Instead of keeping their donut-shaped profile, one can see that a non-vanishing fraction of the positrons is focused to the center. The electrons, in contrast, behave reversely and get slightly defocused. On the applied color scale, this is indicated by a relative noisy background at large radii [see subplot (b)]. In order to understand this difference in detail, consider the electron-positron pair right after its formation. Then, both electrons and positrons propagate at the speed of light in the same direction as the decayed parent photons. In doing so, the pairs are mainly subjected to the superimposed self-fields of the two primary electron beams. The contribution of the co-moving primary electron beam on the transverse (de)focusing, however, is negligible since the leading order force term scales as γ_e^{-2}. Correspondingly, it is the interaction with the opposing primary electron beam that causes the positrons and electrons to become focused and defocused, respectively. Interestingly, the (de)focusing can also be observed in the fully developed pair spectra (see figure 5.2.8). The focusing of positrons leads to an increased number of comparatively low-energetic positrons $\left(\text{below } 125 \text{ MeV}, \ \varepsilon_e/\varepsilon_0 < 10^{-3}\right)$ with respect to the number of electrons. At high energies instead, the spectra of electrons and positrons coincide very well. There, the particles are relativistically too inert for (de)focusing to be important. The log-log plot further implies a power-law behavior, $\mathrm{dN}_e/\mathrm{d}\varepsilon_e \propto \varepsilon_e^{-\tilde{p}}$, for energies $\varepsilon_e/\varepsilon_0 > 10^{-3}$. A `gnuplot` fit in the interval $100 \text{ MeV} < \varepsilon_e < 100 \text{ GeV}$ yields a power-law index of $\tilde{p} \simeq 1$. This differs from the photon case discussed above and will be addressed in more detail in chapter 6.

[9]Note that equation (5.2.14) has a very simple origin. Up to a factor of the order of unity, the normalized number of photons equals the ratio of the interaction time σ_x/c to the radiation time $t_{\mathrm{rad}} = W_\gamma^{-1}$.

[10]By analogy and again up to a factor of the order of unity, the relative energy loss is equal to the normalized number of photons multiplied by the characteristic energy of the emitted photon. In supercritical fields, this is approximately $\varepsilon_\gamma/\varepsilon_0 \simeq 1/4$.

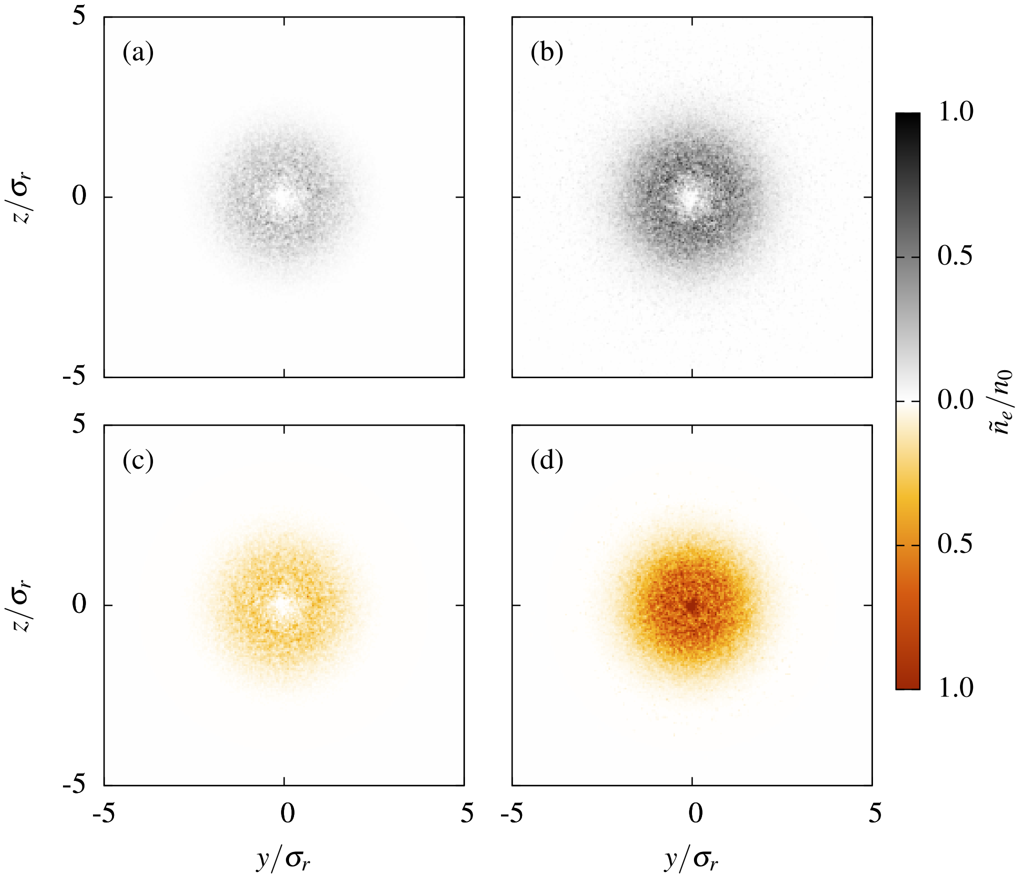

Figure 5.2.7: Transverse distribution of the longitudinally summed [(a), (b)] (pair) electron (in red) and [(c), (d)] positron density (in orange). Subplots [(a), (c)] are recorded at the collision time and subplots [(b), (d)] after the collision.

The focusing and defocusing of the generated pair-plasma jets can have great impact on the collision physics itself. Particularly at relatively high pair yields, and so at long interaction times, this gets predominantly important. In the present case, the relative pair yield after the collision is $N_{e^+e^-}/N_{e_0^-} \simeq 8.6 \times 10^{-3}$, which is rather low. Nonetheless, the result for the relative pair yield is telling because it can be compared with the literature. Following Yokoya, Chen, and Telnov, the number of pairs per primary beam particle for $\Upsilon \gg 1$ can be estimated as [161, 162]

$$\frac{N_{e^+e^-}}{N_{e_0^-}} \simeq \frac{10.4\sqrt{3}}{25\pi} \left(\frac{\sigma_x}{\gamma_e \lambda_C} \alpha \Upsilon^{2/3} \right)^2 \ln(\Upsilon) \,. \tag{5.2.16}$$

After inserting the parameters, one obtains $N_{e^+e^-}/N_{e_0^-} \simeq 9.1 \times 10^{-3}$, which is again in reasonable accordance with the previously mentioned `VLPL` result. Table 5.2.1 gives a summarizing overview about all comparisons between simulation results and literature values. It is also worth mentioning that the above results are verified by simulations with the independent code `OSIRIS`. The results can be found in reference [154]. The overall good agreement strengthens the reliability in `VLPL` simulations.

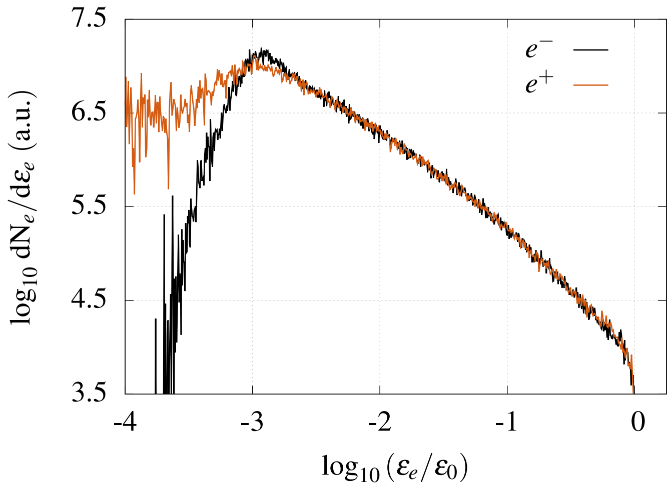

Figure 5.2.8: Log-log plot of the fully developed pair spectra. Electrons are denoted in black and positrons in orange.

	$N_\gamma/N_{e_0^-}$	$\Delta\varepsilon_e/\varepsilon_e$	$N_{e^+e^-}/N_{e_0^-}$
theory	0.194	-0.052	9.1×10^{-3}
data	0.205	-0.050	8.6×10^{-3}

Table 5.2.1: Comparison of the VLPL simulation data with the theoretical predictions by Yokoya, Chen, and Telnov [161, 162].

5.3 Conversion of optical laser pulses into ultra-intense attosecond pulses

In the previous section, it was shown that the head-on collision of two 100 GeV-class electron bunches, each carrying Mega-Ampere currents and being focused to radii on the nanometer scale, generates a promising configuration for reaching highly supercritical fields. Leading experts are indeed confident that such a collider will be technically feasible in the medium-term future. Nevertheless, the development of alternative configurations is essential to deeply attract attention to almost unexplored high-field regimes of the light-matter interaction. The following section therefore introduces an alternative based on high-power laser pulses of the next generation. These laser pulses are intense enough for 100 GeV-class electrons to enter supercritical fields but, as described in section 5.1, their duration is usually too long to mitigate radiation losses of the electrons properly. Thus, it will be discussed subsequently how one can convert an intense optical laser pulse to an ultra-intense attosecond pulse.

The idea for the proposed configuration is adopted from works about the generation of high harmonics in the relativistic regime [164, 165]. Figure 5.3.1 illustrates a schematic representation of the proposal. A laser pulse with central wavelength $\lambda_0 = 1$ µm impinges at oblique incidence onto an over-dense plasma surface. The laser pulse is linearly polarized in the plane of incidence and has a Gaussian profile in both the transverse and the longitudinal direction.

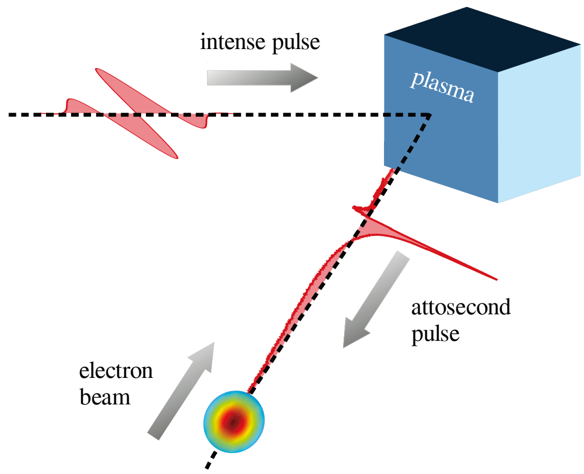

Figure 5.3.1: Schematic of the proposed setup for converting an intense optical laser pulse into an ultra-intense attosecond pulse. The optical pulse ($a_0 = 350$) impinges at an angle of $\theta = 30°$ onto the over-dense plasma target ($n_e = 150\,n_{\mathrm{cr}}$). The generated attosecond pulse is ultra-intense and finally collides with a counter-propagating electron beam (energy $\varepsilon_e \simeq 125$ GeV). Figure published in [163], © 2019 The Authors, available under the CC BY 4.0 license.

The corresponding beam waist parameter is $w_0 = 2.5$ µm. The laser pulse is focused to the point $(x_0, y_0) = (10\lambda_0, 0\lambda_0)$ at time $t = 7.5T_0$, reaching a peak intensity of 1.68×10^{23} Wcm^{-2}. This is equivalent to a dimensionless field amplitude of $a_0 = 350$, which is predicted by facilities like ELI [21]. Longitudinally, the rms duration is $\tau = 1.5T_0$ such that the pulse is nearly single-cycled. But a generalization to multi-cycled laser pulses is in principle possible when using the attosecond lighthouse effect [166]. The angle of incidence is equal to $\theta = 30°$ and is measured with respect to the target's normal direction. The plasma target is assumed to be fully ionized right from the beginning due to the high intensities involved. Spatially, the target is modeled as a combination of a $5\lambda_0$ thick slab of electron density 150 n_{cr} and an exponential plasma density ramp $n \propto \exp\left[(x - x_0)/(0.33\lambda_0)\right]$ for $x < x_0$. The exponential plasma profile ensures a smooth transition from vacuum to over-dense plasma and impacts the efficiency of the high harmonic generation process. In this way, it sets the requirements for the contrast of the high-power laser pulse [167]. The ions are mobile with a mass-to-charge ratio of two times that of protons. Basically, one could use any fully ionized low-Z element as a target material. The probing electrons are modeled as a Gaussian-like beam with rms width and length of $\sigma_\perp = \lambda_0/5$ and $\sigma_\parallel = \lambda_0/40$, respectively. The beam density is chosen such that the total beam charge is approximately 2.8 pC, which corresponds to a peak current of $I_{\max} \approx 13.5$ kA for the above beam width. The beam electrons have the same energy as in the proposal for the non-perturbative QED collider, $\varepsilon_0/\left(m_e c^2\right) = 2.5 \times 10^5$. They are propagating under an angle of $\theta = -30°$ (measured from the target's normal) with the result that a collision with the reflected radiation in a head-on geometry is enabled. The initial position of the electron beam is determined by the focal point of the reflected pulse. The feasibility of the proposal is numerically strengthened through two-dimensional PIC simulations with the code `VLPL`. In these simulations, the numerical grid has a size of $15\lambda_0$ in the x-direction and $20\lambda_0$ in the-y direction with a cell size of $\Delta x = \Delta y = \lambda_0/200$. The over-dense plasma target gets represented by 15 macro-particles per species and cell, while 10 macro-particles per cell resolve the probing electron beam. The QED module is incorporated during the whole simulation, i.e. especially quantum radiation reaction is taken care of in the

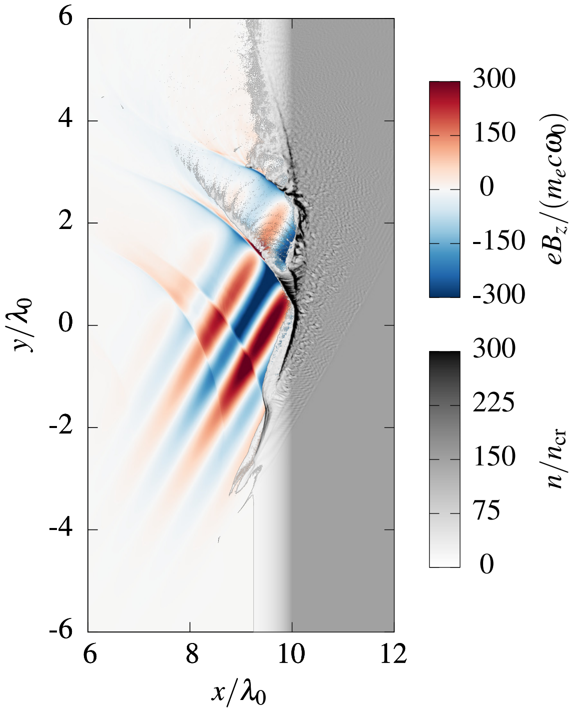

Figure 5.3.2: Plot of the B_z-field (blue-white-red) and the electron density (white-gray-black) in the plane of incidence at time $t = 7T_0$. It is noted that electron densities below $15n_{\rm cr}$ are not plotted in order to improve the visualization.

generation of the attosecond pulse.

Figure 5.3.2 shows simulation results for the electron density (in shades of gray) and the B_z-field (blue-white-red) in the plane of incidence at time $7T_0$. One can see that the incident wave excites electron density modulations on the surface at regular intervals of $\lambda_0/\sin(\theta)$ along y like, for instance, at $(x,y) \approx (10\lambda_0, 0.5\lambda_0)$ and $(x,y) \approx (10\lambda_0, 2.5\lambda_0)$. These modulations correspond to dense electron bunches that form at the target's surface and afterwards cross the vacuum region in front of the target. The electron bunches thereby appear very thin (ultra-short). On their way, the ultra-short bunches interact with the incoming wave which in turn leads to the emission of ultra-short electromagnetic pulses [164, 165]. In figure 5.3.2, this can be seen by arc-like patterns crossing the incoming wave. At time $7T_0$, these patterns are most visible in the vacuum region in front of the target, where they characterize emissions released at an earlier stage in the interaction and are not overlayed by the electron bunches themselves. The arc-like waves propagate perpendicular to the arcs inwards. In this perpendicular direction, they appear very thin indicating their ultra-short duration. Along the arcs, however, the dimensions are significantly larger. This results from the fact that each appropriate phase of the incoming wave continuously excites electron bunches which, as they move through the incoming wave, gradually convert the former into arc-like waves.

The further temporal evolution of the electromagnetic field is shown in figure 5.3.3 in the form of plots of B_z at four different moments in time. As noted previously, it can indeed be seen that the arc-like waves propagate perpendicular to the arc inwards [compare, for instance, subplot (a) with (b)]. Physically speaking, it means that the electromagnetic pulses will be focused to center of the arcs. Associated with this, the peak field strength of the ultra-short pulses

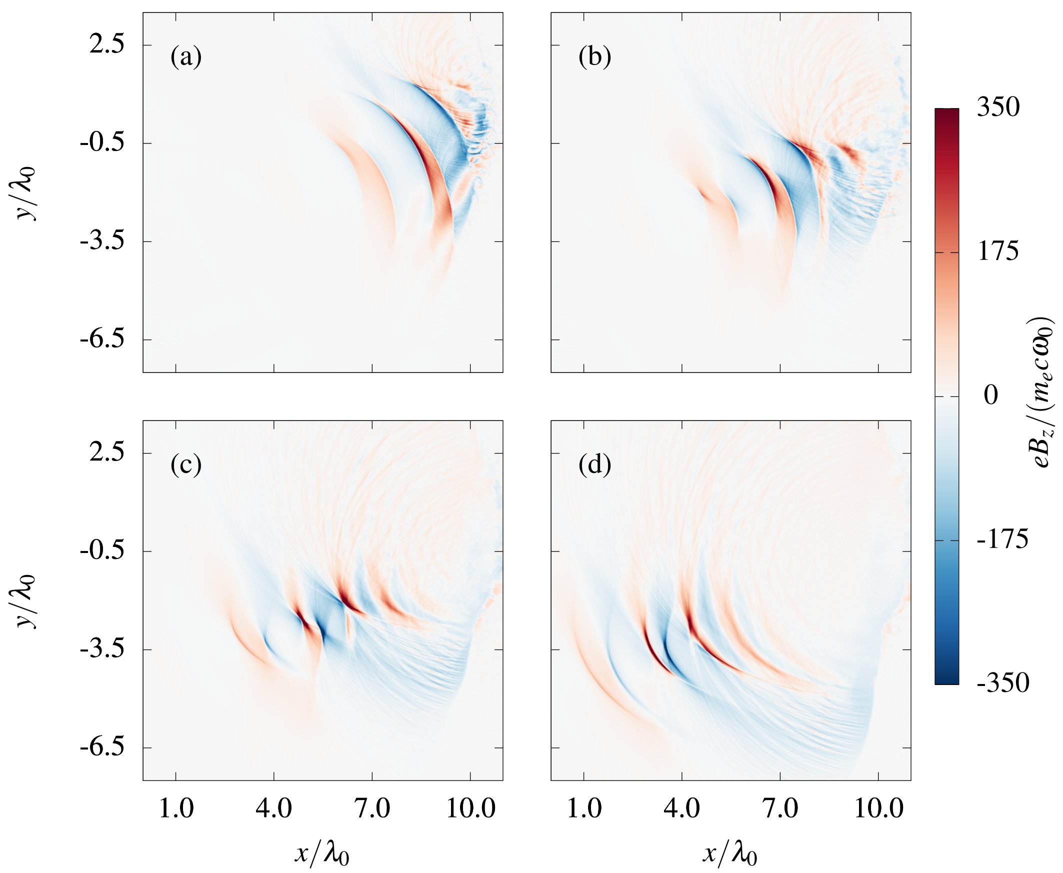

Figure 5.3.3: Plot of the B_z-field in the plane of incidence at four different moments in time, namely at (a) $t = 9T_0$, (b) $t = 11T_0$, (c) $t = 13T_0$, and (d) $t = 15T_0$. The highest field is obtained at time $t = 13T_0$ [see subplot (c)] and thus this time will also be referred to as collision time with the counter-propagating electron beam.

will increase decisively. The highest field observed in the simulation is reached at the point $(x,y) \approx (4.9\lambda_0, -2.6\lambda_0)$ at time $13T_0$ [see figure 5.3.3(c)]. Figure 5.3.3(d) finally shows the B_z-field at time $t = 15T_0$ after passing the focal point. It can be seen directly that the curvature of the arcs is flipped with respect to earlier times, so indicating the divergence of the light beam. As a consequence of this defocusing effect, the peak field strength decreases again which elucidates that the timing of the electron beam is particularly crucial. It is highly desirable that the electrons interact with the field structure shown in figure 5.3.3(c) in order to probe highly supercritical fields. In this context, the focal point in subplot (c) defines the initial position of the electron beam. The time $t = 13T_0$ is therefore referred to as the collision time in the following.

Figure 5.3.4 provides a detailed characterization of the electromagnetic field structure at the collision time. More precisely, figure 5.3.4(a) illustrates the longitudinal profile of the B_z-field along the propagation axis of the probing electrons. In the plot, the abscissa $r_\parallel$ represents the longitudinal distance from the focal point, which per definition is at $r_\parallel/\lambda_0 = 0$.[11] There, one can clearly identify one main peak which is significantly larger in amplitude than the rest. In

[11] To concretize, the electron beam is propagating from $r_\parallel < 0$ to $r_\parallel > 0$.

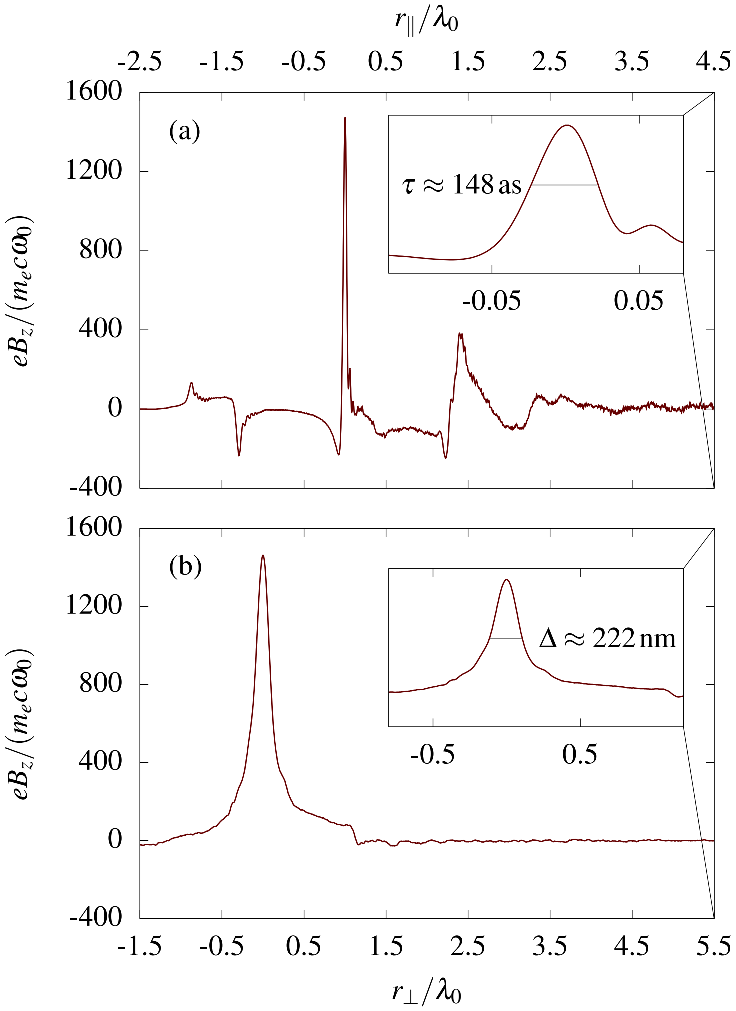

Figure 5.3.4: Cut of the (a) longitudinal and (b) transverse shape for the B_z-component of the generated electromagnetic pulse at the collision time $t = 13T_0$. The insets reveal a full-width-at-maximum duration and spot of $\tau \approx 148$ as and $\Delta \approx 222$ nm, respectively. Please note the different x-axes for top and bottom plot. Data published in [163].

particular, one finds a maximum amplitude of $eB_z/(m_e c\omega_0) \approx 1450$ when normalizing to the central wavelength λ_0 of the driving optical pulse. The peak amplitude implies that maximum values of about 1760 for χ_e might be in reach for the probing electrons if the pulse is short enough. To address that point, the inset in subplot (a) shows an enlarged plot of the main peak. Two interesting features can be deduced here. First, it is evident that the main peak does not contain internal oscillations, meaning that the main pulse is almost unipolar. And second, one can generate an attosecond pulse without applying a spectral filter. Obviously, the latter would simplify the experiment considerably. The data suggest the full-width-at-half-maximum duration to be approximately 150 as. Admittedly, the duration of the main peak is twice as long in comparison with the non-perturbative QED collider ($\tau \approx 78$ as, see section 5.2); but still promisingly short with respect to the characteristic radiation time for 100 GeV-class particles in the case $\alpha\chi_e^{2/3} \simeq 1$ ($t_{\mathrm{rad}} \approx 200$ as). In spite of that, it should be clear that this does not directly imply that the electrons could approach highly supercritical fields. The reason is the

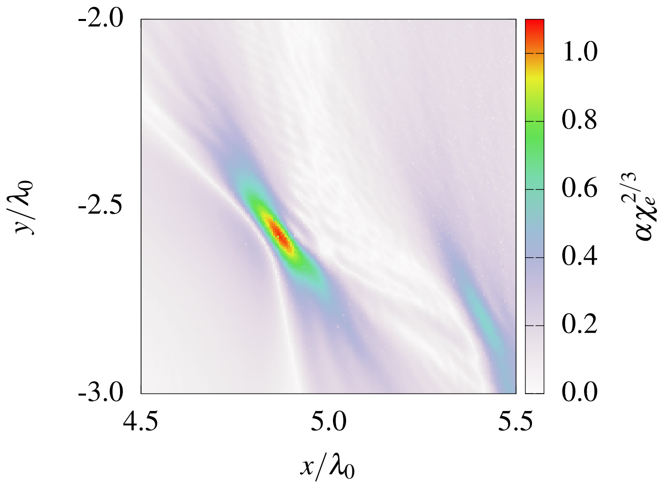

Figure 5.3.5: Plot of the maximum value for the quantity $\alpha\chi_e^{2/3}$ in each simulation cell at the collision time $t = 13T_0$. Data published in [163].

pre-pulse with amplitudes of the order of $eB_z/(m_e c\omega_0) \approx 100$ at $r_\parallel < 0$ which the electrons have to cross before the interaction with the main peak. Though it will turn out shortly that the pre-pulse does not prevent the entering of $\alpha\chi_e^{2/3} \simeq 1$, it will leave imprints in the particle spectra (see figure 5.3.6 and the discussion in section 6.2). On the other hand, figure 5.3.4(b) shows a transverse cut of the magnetic field B_z at the focus. The inset reveals a focal spot size of approximately 220 nm. Combining all the parameters, one obtains a peak intensity of 2.9×10^{24} Wcm^{-2} and a peak power of 4.5 PW for the generated electromagnetic pulse. Finally, it is noted that all spatial dimensions of the generated attosecond pulse are larger than those in the case of the non-perturbative QED collider. The peak field, in contrast, is the same (at least up to a factor of unity). The QED algorithm can thus be applied to the collision of the probing electrons with the attosecond pulse (see section 5.2.2).

The demonstration that the non-perturbative regime $\alpha\chi^{2/3} \simeq 1$ might be accessed with the present setup is given in figure 5.3.5, where the maximum value of the non-perturbative parameter for the probing electrons is plotted in each simulation cell. In fact, one can deduce from the figure that the pre-pulse does not prevent all the electrons from reaching $\alpha\chi_e^{2/3} \simeq 1$. In contrast, one can see that there are electrons in almost the entire vicinity of the focal point that surpass χ_e values of 1600 at the collision time. For instance, the highest value observed in the simulations is $\alpha\chi_e^{2/3} \approx 1.06$, which is equal to $\chi_e \approx 1750$. This in turn is in very good agreement with the maximum attainable value for electrons with energy $\varepsilon_0/\left(m_e c^2\right) = 2.5 \times 10^5$ colliding with a field of strength ≈ 1450 in a head-on scenario as given above.

On their way through the field structure shown in figure 5.3.4, the probing electrons lose a part of their kinetic energy by emitting high-energy photons. In a second step, these photons can decay into electron-positron pairs. As already explained in the previous section, these secondary particles might give insights into the physics of the interaction in the regime $\alpha\chi^{2/3}$. In that regard, particle spectra are probably those observables that can be accessed simplest from an experimental point of view. For this reason, figure 5.3.6 gives information about the spectra of the particles[12]. It is again striking that the photon spectrum (blue line) obeys a rather well-defined

[12]For clarification: The spectra are only given for particles that are directly connected to the probing electrons.

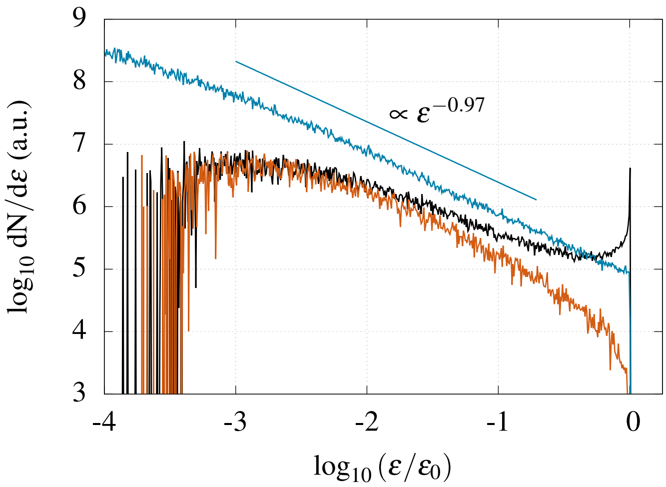

Figure 5.3.6: Simulation results for the spectra of electrons (black), photons (blue) and positrons (orange) obtained from the interaction of 125 GeV electrons the generated electromagnetic field structure at time $t = 13T_0$. The linear function corresponds to a `gnuplot` fit in the energy interval 125 MeV $< \varepsilon <$ 25 GeV. Data published in [163].

power law over a large energy interval. In comparison with the photon spectrum generated by the non-perturbative QED collider (see figure 5.2.6), however, the photon spectrum decays here slightly faster[13]. The `gnuplot` fitting routine reveals a power-law index of $p \simeq 0.97$ when performing a linear fit to the data in the energy interval 125 MeV $< \varepsilon <$ 25 GeV. A comprehensive discussion why the photon spectrum (and also all others) obeys a power law and how one can understand the power-law index will be given in chapter 6. At this juncture, it should only be stressed that the steeper slope in figure 5.3.6 can be ascribed to the effectively longer interaction time, mainly caused by the pre-pulse and not by the 150 as main pulse. It is also interesting to note that the bump at the high-energy cutoff cannot be observed here. Besides the photon spectrum, figure 5.3.6 also shows the spectra of positrons (orange) and electrons (black). It can be seen that both the electron and positron spectrum follow a power law over a certain interval. Thereby, the shape of the positron spectrum resembles the one from the non-perturbative QED collider (see figure 5.2.6). Only at low energies the behavior is qualitatively different. The reason for that is basically the importance of the exact shape of the electromagnetic field for weak relativistic particles. In the case of the collider, the collective field of the electron beams tends to focus opposing positrons and to confine them axially based on the field's donut shape. Such a confinement is not possible with the present field configuration, so that the number of low-energetic positrons is less and the qualitative behavior is the same for positrons and electrons. Indeed, this can be seen in the figure, where the spectra of electrons and positrons match up to an energy of approximately 1 GeV. Thereafter, it comes to a deviation in the spectra. This can be attributed to the fact that, in contrast to figure 5.2.6, the full electron spectrum is shown, i.e. no distinction between probing electrons and generated pair electrons is made. Simultaneously, it means that below 1 GeV the electron spectrum is dominated by pair electrons and above by initial beam electrons. Interestingly, the slope of the electron spectrum in the part where the spectrum is dominated by beam electrons is flatter compared to the positrons. One can also see

[13] As a reminder, the photon spectrum follows a power law with an index of $p \simeq 0.73$ in the case of the non-perturbative QED collider (see figure 5.2.6).

that the spectrum peaks when the energy approaches ε_0. The peak at ε_0 refers to beam electrons that did not suffer critical radiation losses at all, and so shows once more that the setup might be used to probe highly supercritical fields.

5.4 Reducing the switching time of the electromagnetic field by plasma screening

In the two preceding sections, it was shown that highly supercritical fields either might be reached by the collision of two high-current, 100 GeV-class electron beams or by the collision of a single 100 GeV-class electron beam with an ultra-intense attosecond pulse. It was supported by simulations that the ultra-intense attosecond pulse can be generated in the interaction of a high-power laser pulse with a dense plasma target. Since much effort is currently put in the construction of high-intensity laser facilities all around the globe, the demonstration that high-power laser pulses are promising for reaching extremely regimes of QED is of great interest. On the other hand, the generation of the ultra-intense attosecond pulse can depend sensitively on the parameters of the interaction like, for instance, the angle of incidence, the profile of the pre-plasma, or the plasma density. Exactly controlling all the parameters in the experiment, however, will be a very challenging task. Resulting from this, it arises the question of simpler setup geometries using high-power laser pulses. The main point that needs to be clarified is the question how one can reduce the switching time of the ultra-strong laser field in order to mitigate radiation losses of the electrons decisively. In the following, it will hence be motivated that instead of converting an incident optical pulse into an attosecond pulse, the plasma itself can directly truncate the laser pulse front. Consider in this connection a laser pulse which illuminates a solid target at normal incidence. Typically, electron densities of the order of 10^{23-24} cm^{-3} can be reached in solid materials[14], and so extremely dense plasma ($\sim 1000 n_{\mathrm{cr}}$) can be produced by ultra-high intensity laser pulses. As a consequence, it is unlikely for the irradiating laser pulse to penetrate deeper into the plasma than the relativistic skin depth [168][15],

$$l_s = \frac{\lambda_0}{2\pi}\sqrt{\frac{\bar{\gamma}_e n_{\mathrm{cr}}}{n_e}}. \tag{5.4.1}$$

Here $\bar{\gamma}_e$ is the averaged Lorentz factor of electrons at the plasma surface. It finally emerges a sharp interface separating the quasi field-free plasma from the non field-free vacuum. This means that an ultra-relativistic electron beam, which is crossing the plasma towards the sharp interface, is subjected to the laser field just in the thin skin layer. If the time l_s/c, which elapses as the electrons pass the skin layer, is shorter than or at least comparable to the characteristic radiation time t_{rad}, then radiation losses could be mitigated sufficiently. Figure 5.4.1 illustrates a schematic presentation of the idea.

Simulation in a one-dimensional geometry

Similar to the previous sections, the feasibility of the proposal is emphasized by PIC simulations with the code `VLPL`. First, the simulations are performed in a one-dimensional geometry. The

[14] For instance, fully ionized aluminum has an electron density of $\approx 7.8 \times 10^{23}$ cm^{-3}, fully ionized silicon of $\approx 7.0 \times 10^{23}$ cm^{-3}, or fully ionized diamond of $\approx 1.06 \times 10^{24}$ cm^{-3}.

[15] It is assumed that the thickness of the plasma is large with respect to the skin depth.

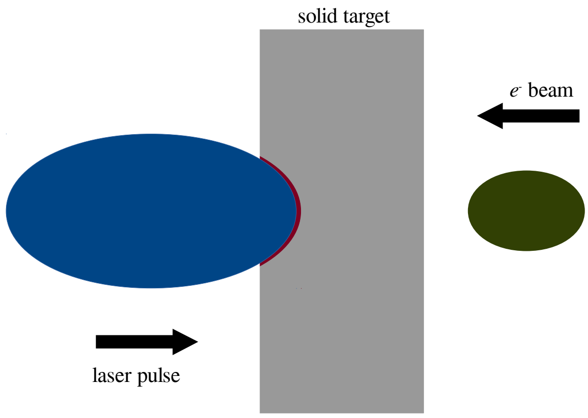

Figure 5.4.1: Schematic of how to reduce the effective interaction time by the plasma itself. A circularly polarized optical pulse ($a_0 = 1400$) impinges at normal incidence onto a solid-dense target. The laser pulse can only penetrate in the skin layer (red) of the plasma. A counter-propagating electron beam, $\varepsilon_0/\left(m_e c^2\right) = 2.5 \times 10^5$, is almost instantaneously subjected to the field of the optical pulse. Figure published in [169], © 2019 IOP Publishing, reproduced with permission, all rights reserved.

simulation box has a size of $15\lambda_0$ in the x-direction, where $\lambda_0 = 1$ µm is again the central wavelength of the laser pulse. The simulation domain is divided into 15,000 cells, corresponding to a cell size of $\Delta x = 0.001\lambda_0$. The rather fine resolution is necessary in order to accurately resolve the skin depth of the high-density plasma target. As such, a $7.5\lambda_0$ thick diamond foil beginning at $x = 5\lambda_0$ is used, which is assumed to have solid density and additionally to be fully ionized right from the start of the simulation. Expressed in terms of the critical density for a one micron wavelength this gives an ion density of $n_i = 158n_{\mathrm{cr}}$ and an electron density of $n_e = 6n_i = 948n_{\mathrm{cr}}$. In the simulations, 30 macro-particles per cell represent the carbon ions and 180 macro-particles per cell the related electrons.
The probing electron beam is propagating in the negative x-direction and has a Gaussian density profile, $n_{e,\mathrm{probe}} = n_0\, e^{-x^2/(2\sigma_x^2)}$. Here, $n_0 = n_{\mathrm{cr}}$ is the peak density and $\sigma_x = \lambda_0/4$ is the rms length of the electron beam. The initial energy of each beam electron is the same as in the two sections before, $\varepsilon_0/\left(m_e c^2\right) = 2.5 \times 10^5$. Numerically, the electron beam is modeled by 50 macro-particles per cell. It is further noted that the electron beam has sharp edges at a distance of $3\sigma_x$ from its center, which has basically the reason to save computational resources.
The plasma is driven by a laser pulse which impinges at normal incidence onto its surface. In this way, the laser pulse is also counter-propagating with respect to the probing electron beam. The laser pulse has a Gaussian temporal profile, $a = a_0\, e^{-(x-ct)^2/(2\sigma_\tau^2)}$. The dimensionless field amplitude a_0 and the rms duration σ_τ are equal to 1400 and $1.5T_0$, respectively. If one further assumes the laser pulse to be circularly polarized, a peak intensity of 5.4×10^{24} Wcm^{-2} will be reached. Although recent works about radiation pressure acceleration in ultra-intense fields have shown that electron heating and especially radiation losses of the plasma electrons can be significant for circular polarization [170–172], they are expected to be much stronger in the case of linear polarization [67, 173]. To affect the laser–plasma interaction as little as possible, circular polarization is therefore preferred.

Whether a probing electron emits a photon or not, and so experiences radiation losses, is predom-

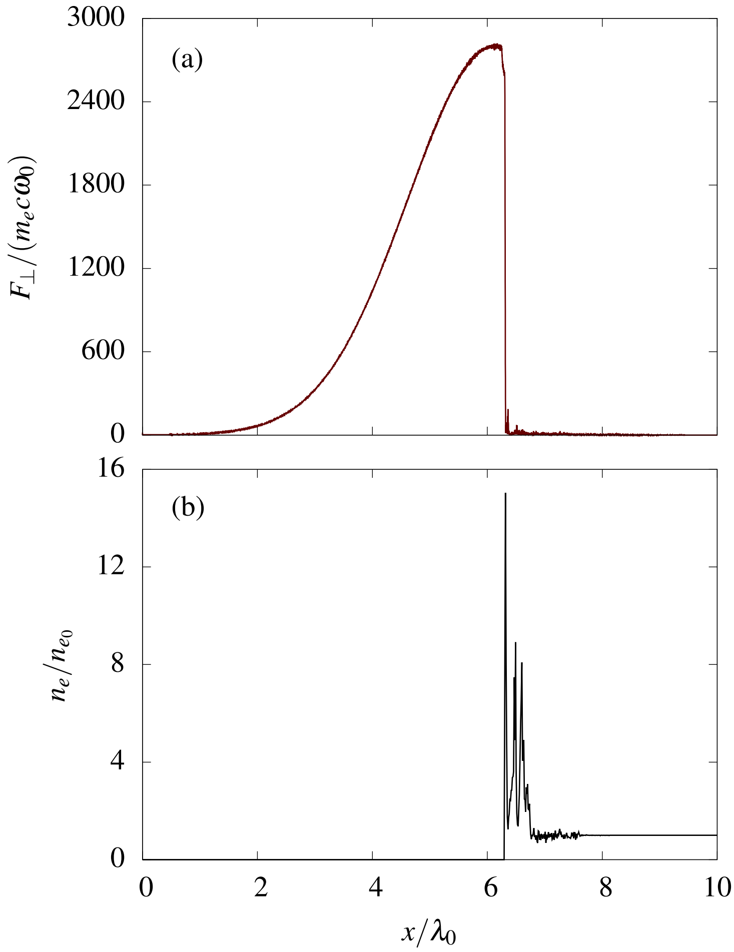

Figure 5.4.2: Plot of (a) the transverse force experienced by a particle moving in the negative x-direction nearly at the speed of light according to equation (5.4.2) and (b) the electron density of the plasma target. Both snapshots are recorded at time $t = 11.125T_0$. Data published in [169].

inantly triggered by the force acting perpendicular to its direction of motion. For ultra-relativistic electrons moving in the negative x-direction, the absolute value of this transverse force can be calculated as

$$F_\perp = e\sqrt{(E_y + B_z)^2 + (E_z - B_y)^2}. \tag{5.4.2}$$

For the configuration described here, the simulation result for equation (5.4.2) at time $t = 11.125T_0$ is illustrated in figure 5.4.2(a). At first sight, one can see a clear difference in the transverse force for $x \lesssim 6.3\lambda_0$ and $x \gtrsim 6.3\lambda_0$. The almost step-like drop is strongly related to the plasma electrons which fill the space $x \gtrsim 6.3\lambda_0$, as can be seen in figure 5.4.2(b). In fact, one can observe electron densities at the surface that are more than 10 times higher than the initial electron density of the target n_{e_0}. It is this high-density plasma surface which prevents the laser radiation from penetrating deeply into the plasma. Resulting from that the ultra-relativistic beam electrons are not subjected to substantial transverse forces inside the plasma. Only outside the plasma ($x \lesssim 6.3\lambda_0$), the beam electrons experience a transverse acceleration and so will be stim-

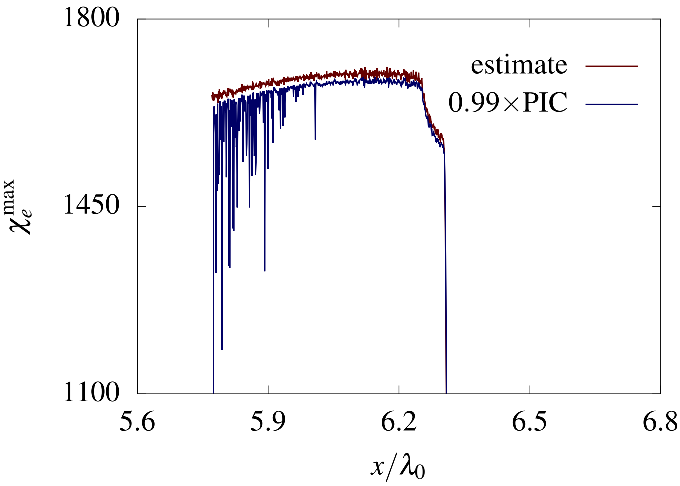

Figure 5.4.3: Plot of the maximum value for the χ_e parameter in each simulation cell at time $t = 11.125T_0$. Note that the sharp edges on the left and right are related to the cutting of the electron beam at $-3\sigma_x$ from its center (left side) and to the plasma which screens the laser fields (right side). Data published in [169].

ulated to emit photons. The gradient, i.e. the distance over which the transverse force changes, appears to be ultra-steep on the scale of $\lambda_0 = 1$ µm. A closer look at the data reveals that the layer is only 18 nm thick. Expressed in time instead, it yields that the laser field is effectively switched on after only 60 as. Recalling that the characteristic radiation time for 100 GeV-class electrons and $\alpha\chi_e^{2/3} \simeq 1$ is of the order of 200 as [see equation (5.1.1)], the skin-layer approach allows the beam electrons to be injected directly into the most intense part of the laser field without suffering strong radiation losses. It is further found in figure 5.4.2(a) that the normalized peak field is $\approx 2800 = 2a_0$. Here the factor 2 mirrors the head-on scattering geometry. Furthermore, it is stated that—in the same sense as described in section 5.2.2—the effective field parameters (such as amplitude and gradient length) allow the use of the QED module with respect to the probing electron beam.

Figures 5.4.3 and 5.4.4 depict simulation results for the χ_e value of the probing electrons. More precisely, figure 5.4.3 compares $\chi_e^{\max}$ (red curve), the maximum value of χ_e in each simulation cell, with the maximal attainable value for electrons with energies $\varepsilon_0/\left(m_e c^2\right) = 2.5 \times 10^5$ in the field described by figure 5.4.2 (blue curve). The result from the PIC simulation is here multiplied with 0.99 to improve the visibility by avoiding the overlap of the red and blue curve. Already at first glance one can see the sharp edges on the plot's left and right. This is due to the cutting of the beam at $-3\sigma_x$ from its center (left side) and to the plasma which screens the laser field (right side) [see also figures 5.4.2(a) and (b)]. Further, the plot allows drawing two more important conclusions. First, the simulation result corroborates that χ_e values above 1600 might be probed with this setup. Indeed, a maximum value of ≈ 1700 is observed in the simulations. This is very close to the prediction of

$$2a_0 \frac{\varepsilon_0}{m_e c^2} \frac{\hbar\omega_0}{m_e c^2} \simeq 1698. \tag{5.4.3}$$

Moreover, one still finds χ_e values of approximately 1650 up to the left edge of the plot. This leads directly to a second very important point. The estimate and the PIC simulation result coincide very well over the entire interval $5.8 < x/\lambda_0 < 6.3$. This is surprising as it states

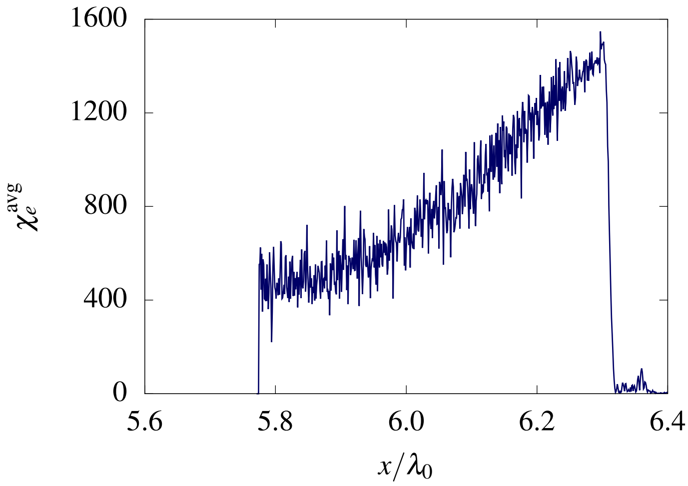

Figure 5.4.4: Plot of the averaged value for the quantum nonlinearity parameter in each simulation cell at time $t = 11.125T_0$. It is noted that the sharp edges on the left and right are related to the cutting of the electron beam at $-3\sigma_x$ from its center (left side) and to the plasma which screens the laser field (right side). Data published in [169].

that there are electrons that resist these extreme fields without suffering significant radiation losses for a distance in the order of a few hundred nanometers. Obviously, these represent times clearly above t_{rad}. In actual fact, these non-radiating beam electrons are just the exception. To illustrate that, figure 5.4.4 shows χ_e^{avg}, the averaged value of χ_e in each simulation cell. Here, the calculation of χ_e^{avg} is performed as explained in the context of equation (5.2.12). As expected, figure 5.4.4 reveals that χ_e decreases in average for longer interaction distances (times). For instance, χ_e^{avg} is about 500 at the left edge ($x \approx 5.8\lambda_0$) and so more than three times smaller than at the right edge ($x \approx 6.3\lambda_0$). There, one has values of 1500. In between, the data follow an exponential law, $\chi_e^{\text{avg}} \propto \exp(-|x - x_r|/\Lambda)$ for $x < x_r = 6.3\lambda_0$. Using again the `gnuplot` fitting routine, the spatial decay length Λ is approximately $0.395\lambda_0$ at time $11.125T_0$. This, however, overestimates the real spatial decay length slightly. The reason for that is the plasma surface which is moving at the hole-boring velocity v_{HB} along the positive x-axis. As a consequence, the interaction is effectively shortened. Taking the motion of the surface into account and switching to the time domain, one eventually arrives at

$$T = \frac{\Lambda}{c + v_{\text{HB}}}, \tag{5.4.4}$$

where T stands for the temporal decay constant. In the present simulation, the hole-boring velocity can be determined to be $v_{\text{HB}} \simeq 0.4c$, as can be seen from the space-time distribution of the ion density [see figure 5.4.5]. Re-inserting this subsequently into equation (5.4.4), one obtains $T \simeq 0.282T_0$ for the characteristic decay time. In relation to the characteristic radiation time t_{rad}, the effective temporal decay constant is thus $T \simeq 4t_{\text{rad}}$ at time $11.125T_0$. So, the decay time describing the averaged quantum parameter is longer but still of the same order of magnitude as t_{rad}. More interestingly, one can understand the factor 4 in a rule-of-thumb manner. The laser field is almost constant over the interval $5.8 < x/\lambda_0 < 6.3$ [see figure 5.4.2(a)] with the result that χ_e^{avg} is predominantly determined by the averaged electron energy. The ratio of χ_e^{avg} at positions $x \simeq 5.8\,\lambda_0$ to $x \simeq 6.3\,\lambda_0$ should thus be equal to the ratio of the corresponding averaged electron energies. As electrons emit in average photons with energy $\varepsilon_\gamma \simeq \varepsilon_0/4$ in the

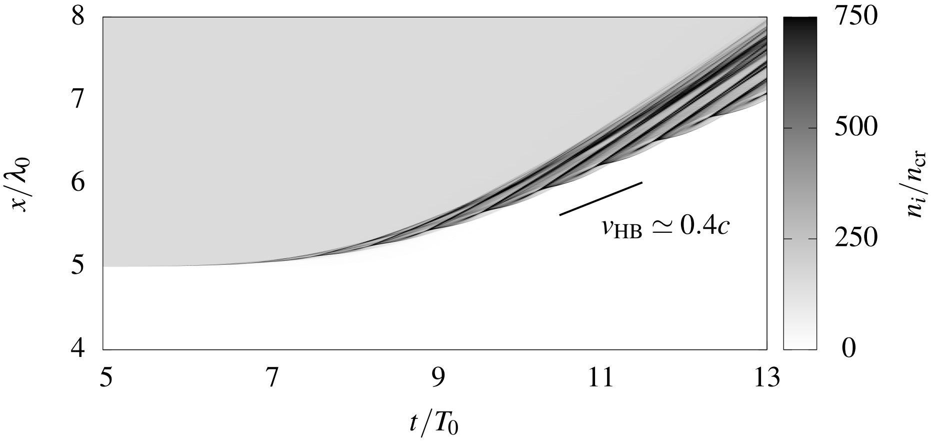

Figure 5.4.5: Space-time distribution of the ion density. The target surface is pushed inwards due to the radiation pressure exerted by the circularly polarized laser pulse. In the time interval $10.5 \leq t/T_0 \leq 11.5$ the velocity of the front surface is equal to $v_{\mathrm{HB}} \simeq 0.4c$ which is indicated by the black line.

limit $\chi_e \gg 1$, the ratio of the actual electron energy ε_e to the initial energy ε_0 after n emissions is $\varepsilon_e/\varepsilon_0 \simeq (3/4)^n$. Equating that with the ratio of χ_e^{avg} finally gives that one expects roughly $n = 4$ emissions from an electron between $x \simeq 5.8\,\lambda_0$ and $x \simeq 6.3\,\lambda_0$.

Simulation in a two-dimensional geometry

In order to check the impact of the reduced dimension on the results, simulations are also performed in a two-dimensional geometry. The simulation parameters from the one-dimensional case remain the same, if not stated otherwise. The specific two-dimensional parameters are as follows. The simulation box has a size of $15\lambda_0$ in the y-direction with a cell size of $\Delta_y = 0.1\lambda_0$. Likewise, the diamond foil is $15\lambda_0$ wide in the transverse direction and it is represented by 5 ion macro-particles and 30 electron macro-particles per cell. The laser pulse is focused to a minimum beam waist with radius $w_0 = 2.5$ µm located at the front of the plasma surface $(x = 5\lambda_0)$ at time $t = 10T_0$. The density profile of the probing electron beam is Gaussian-like in both directions, $n^{2D}_{e,\mathrm{probe}} = n^{1D}_{e,\mathrm{probe}}\, e^{-y^2/(2\sigma_y^2)}$, with the rms width $\sigma_y = \lambda_0/2$. As for the one-dimensional simulation, the electron beam is cut at $\pm 3\sigma_x$, but also laterally at $\pm 3\sigma_y$. Numerically, the electron beam gets resolved by 10 macro-particles per cell.

Comparable to figure 5.4.2 in the case of the one-dimensional simulation, figure 5.4.6 shows (a) a cut along the axis $y = 0\lambda_0$ of the transverse force exerted on an ultra-relativistic particle moving in the negative x-direction and (b) of the plasma electron density. Both data are recorded at time $11T_0$. Though minor deviations can be detected, the main physics is the same. The radiation pressure associated with the laser pulse pushes the target surface inwards, resulting in electron densities that are considerably higher than at the beginning. In that regard, peak electron densities above $6n_{e_0}$ can be obtained at $t = 11T_0$. These peak densities, however, are below those in the one-dimensional case [see figure 5.4.2(b)]. This is due to the inhomogeneity of the laser pulse in the y-direction which causes a ponderomotive expulsion of the electrons from

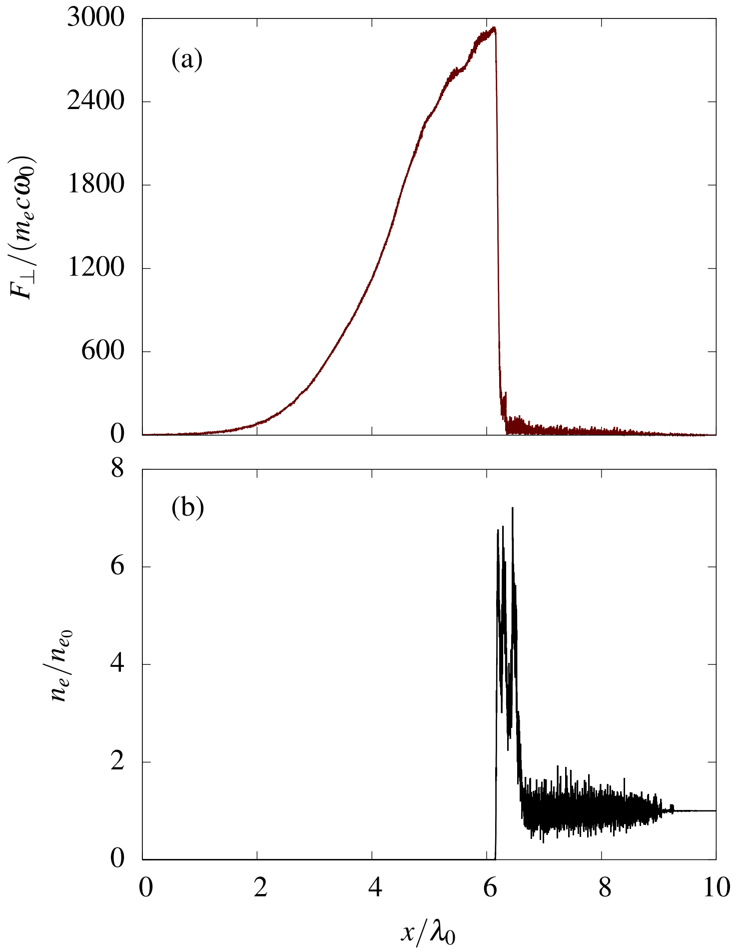

Figure 5.4.6: Plot of (a) the transverse force experienced by a particle moving nearly at the speed of light in the negative x-direction according to equation (5.4.2) and (b) the electron density of the plasma target. Both snapshots show a cut at $y = 0\lambda_0$ and are recorded at time $t = 11T_0$.

the center. However, the density is still high enough to prevent the laser pulse from penetrating deeply into the target. As in the previous case, the data reveal that the gradient length over which the transverse force drops is in the order of 20 nm. It can be also found that the plasma front is moving slower than before. As a consequence, the peak force is already reached $T_0/8$ earlier. An explanation could be that the plasma electrons emit more γ-photons. Conversely, energy transfer from the laser field to the ions is less efficient, finally yielding a reduction of the hole-boring velocity [170].

The simulation result for χ_e is given in figure 5.4.7 which illustrates the quantum nonlinearity parameter for every tenth beam electron at time $t = 11T_0$. It can be clearly seen that χ_e values above 1600 are still predicted. It means that the key point is not affected in a critical way through the more realistic two-dimensional geometry.

To comment briefly, the last presented configuration may be particularly promising from an experimental point of view. Obviously, the main advantage is its very simple geometry. One just

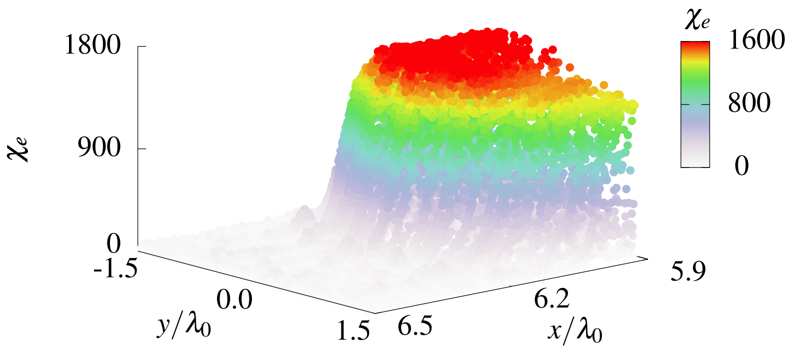

Figure 5.4.7: Plot of the quantum nonlinearity parameter χ_e obtained from the two-dimensional simulation for a fraction of the beam electrons at time $t = 11T_0$. It can be seen that even in the two-dimensional case, χ_e surpasses the value of 1600. Data published in [169].

has to irradiate a solid material with an ultra-strong laser pulse at normal incidence. Of course, one also needs 100 GeV-class electrons. But, these electrons do not have to be available in terms of extremely high-current and tightly focused/compressed beams (see section 5.2). Furthermore, the conversion of an optical into an ultra-intense attosecond pulse is not necessary (see section 5.3). The latter may depend in a sensitive way on the interaction parameters and may thus require their accurate control. However, even for the skin-layer setup further work is essential. This particularly addresses potential observables as the spectra of particle are only of limited suitability. This is due to the interaction with the long tail of the optical laser pulse, which dominates the spectra. How this can be understood in detail will be covered by the next chapter 6.

For the sake of completeness, it should be mentioned that two additional configurations have been proposed recently. The first approach is a laser-based one. Blackburn *et al.* achieve the mitigation of radiation losses by the cross-collision of 40 GeV electrons with an optical laser beam of intensity 2×10^{24} Wcm^{-2} [174], i.e. the scattering angle is 90°. The driving idea is there that it is generally easier to reduce the laser focal spot than the laser duration. In this way, the unfavorable scattering geometry prevails over higher radiation losses in the head-on scattering case. The second proposal builds on the interaction of ultra-relativistic electrons with strong crystalline fields [175]. In detail, Di Piazza *et al.* report on TeV electrons that pass thin tungsten crystals. Both approaches, however, focus their attention to the close, non-perturbative QED regime with values of χ around 100.

5.5 Summary

In summary, the last chapter started with an introduction of the highly supercritical regime of QED. This regime, which is characterized by the fact that radiative loop corrections are so important that QED perturbation theory is conjectured to break down, requires the background field to be extremely strong such that $\chi \gtrsim 1600$. It is widely believed that the regime is far beyond experimental reach due to ultra-short radiation loss times. Notwithstanding the above, it was consecutively shown via PIC simulations that radiation losses can be mitigated in several configurations. Here, three experimental setups were proposed that sound promising for reaching and so for probing the highly supercritical regime.

Firstly, it was explained in section 5.2 that one could probe the regime by the collision of two high-current 100-GeV-class electron bunches, so circumventing the use of optical laser radiation. Namely, when each electron bunch carries a Mega-Ampere current and is additionally focused to a transverse size of $\sigma_r = 10$ nm, its collective self-field can be as strong as provided by the most intense optical laser. Compressing the bunch also longitudinally to a length of $\sigma_x = 10$ nm, it was demonstrated that electrons in each counter-propagating bunch could reach $\chi \gtrsim 1600$. It was further argued that the photons and electron-positron pairs generated during the collision could give insights about the physics of the interaction. Interestingly in that context, the particle spectra were found to obey well-defined power laws over a certain energy range.

Secondly, it was proposed in section 5.3 how one can use intense optical laser radiation instead. It was particularly argued that one could convert an incident optical laser pulse into an ultra-intense attosecond pulse. The conversion from optical to attosecond pulse was here done with the help of high-harmonic generation at an over-dense plasma surface. In this way, it was shown that one could generate an almost unipolar pulse with peak intensity $I \approx 2.9 \times 10^{24}$ Wcm^{-2} and an ultra-short pulse duration of only $\tau \approx 150$ as. With that pulse, it was finally possible to reach $\chi \gtrsim 1600$ for a counter-propagating 100-GeV-class electron beam.

Thirdly, it was considered in section 5.4 that one could directly use a plasma to reduce the switching time of the strong laser field. The key word is the skin depth up to which a laser pulse can propagate into an over-dense plasma before getting reflected. Using a solid-dense diamond target, the penetration depth was numerically found to be of the order of $l_s \approx 20$ nm. An electron beam that propagates through the plasma towards the irradiating laser pulse was shown to facilitate approaching the highly supercritical regime.

6 Non-perturbative QED and its identification

The previous chapter had the intention to demonstrate that highly supercritical fields may be in experimental reach in the not too distant future. As pointed out therein, this can be achieved either by the collision of two counter-propagating high-current (~ 1.7 MA) and high-energy (~ 100 GeV) electron bunches with dimensions on the nanometer scale (see section 5.2) or by head-on collisions of 100 GeV electron beams with strong laser radiation (see sections 5.3 and 5.4). The prospect of promising experiments, however, also raises the question on how one can identify the entering of such a regime experimentally. The following chapter will address this issue in more detail. It will be shown that the spectra of particles being involved in the interaction (i.e. electrons, positrons, and high-energy photons) represent an important observable. In particular, an analytical model describing the temporal evolution of the particle's energy distribution is introduced that finally allows differentiating the impact of non-perturbative QED effects from the particle spectra.

6.1 Modeling the spectra of ultra-relativistic particles in supercritical fields

The main purpose of the following section is the introduction of a model describing the ultra-short interaction of ultra-relativistic particles with (highly) supercritical fields in a self-consistent manner. In the end, the model gives insights about the shape of the particle spectra after the interaction.

The analytic approach starts with the consideration of the particle dynamics in the phase space. Although the particle's phase space is in principle six-dimensional (three coordinates and three momenta), the proposed experimental geometries can be used to greatly reduce the dimensionality and thus the complexity of the problem. For instance, the interaction time τ between particles and fields is expected to be ultra-short. This means that for ultra-relativistic (≈ 100 GeV) electrons the transversely gained momentum $p_\perp = q_e E \tau$ is much less than the longitudinal one. Correspondingly, the particle trajectories are only distorted by the negligible angle $\vartheta \simeq p_\perp/(\gamma_e m_e c) \ll 1$ during the interaction, so that one can completely neglect the transverse motion. Following the same line of argument, one can also neglect the impact of the fields on the longitudinal momentum component. It is therefore reasonable to assume that all particles move on straight lines at the speed of light, $x(t) = x_0 + ct$. It results that the phase space becomes effectively one-dimensional, so that the dynamics can solely be described by the particle energy ε. Of course, the particle energy and so the particle distribution function can be altered by QED processes. However, as will be motivated later (see section 6.2.2), the exact shape of the external field is of second rank for $\chi \gg 1$, so that one can treat the background as a globally constant magnetic field [176]. Then, the temporal evolution of the distribution functions is governed by the one-dimensional Boltzmann equations

$$\begin{aligned}
\partial_t f_\gamma(\varepsilon) &= -\,W_{\text{pair}}(\varepsilon)\, f_\gamma(\varepsilon) \\
&\quad + \int_\varepsilon^\infty \mathrm{d}\tilde{\varepsilon}\ \left[f_{e^-}(\tilde{\varepsilon}) + f_{e^+}(\tilde{\varepsilon})\right] \left.\frac{\mathrm{d}W_{\text{rad}}}{\mathrm{d}\varepsilon}\right|_{\tilde{\varepsilon}\to\tilde{\varepsilon}-\varepsilon}, \\
\partial_t f_{e^-,e^+}(\varepsilon) &= -\,W_{\text{rad}}(\varepsilon)\ f_{e^-,e^+}(\varepsilon) \\
&\quad + \int_\varepsilon^\infty \mathrm{d}\tilde{\varepsilon} \left[f_\gamma(\tilde{\varepsilon}) \left.\frac{\mathrm{d}W_{\text{pair}}}{\mathrm{d}\varepsilon}\right|_{\tilde{\varepsilon}\to\varepsilon} + f_{e^-,e^+}(\tilde{\varepsilon}) \left.\frac{\mathrm{d}W_{\text{rad}}}{\mathrm{d}\varepsilon}\right|_{\tilde{\varepsilon}\to\varepsilon} \right].
\end{aligned} \tag{6.1.1}$$

Here, f_γ and f_{e^-,e^+} are the particle distribution functions at time t, describing high-energy photons, electrons, and positrons, respectively[1]. However, it should be clear that under the above assumptions the particle distribution functions coincide with the particle spectra. In addition, $W_{\text{rad}}(\varepsilon)$ and $W_{\text{pair}}(\varepsilon)$ are the total photon emission rate and the total pair creation rate for a parent particle with energy ε, $(\mathrm{d}W_{\text{rad}}/\mathrm{d}\varepsilon)|_{\tilde{\varepsilon}\to\varepsilon}$ is the differential photon emission rate for an electron (or a positron) to change its energy from $\tilde{\varepsilon}$ to ε through the emission of a high-energy photon[2], and $\left(\mathrm{d}W_{\text{pair}}/\mathrm{d}\varepsilon\right)\big|_{\tilde{\varepsilon}\to\varepsilon}$ is the differential pair production rate for a photon with energy $\tilde{\varepsilon}$ to decay into an electron with energy ε and a positron with energy $\tilde{\varepsilon}-\varepsilon$. The general solution of the coupled system of Boltzmann equations (6.1.1) is very complicated. In principle, a formal solution can be expressed in terms of time-ordered exponentials since the equations are linear in the particle distribution functions [176]. However, a different approach will be pursued in the following. It turns out to be convenient to solve equation (6.1.1) in perturbation theory with respect to time t. This is reasonable as the total interaction time τ is supposed to be short on timescales representing the QED processes, $W_{\text{rad, pair}}\,\tau \leq 1$. This leads to the ansatz

$$f_\mu(t) = f_\mu^{(0)} + f_\mu^{(1)} + f_\mu^{(2)} + \ldots \tag{6.1.2}$$

for the particle spectra, where $\mu = \gamma,\ e^-,$ and e^+ indices the different particle species, and $f_\mu^{(i)} \propto \left(W_{\text{rad, pair}}\, t\right)^i$ describes the spectrum in the i-th order of the perturbation theory. Recalling the proposed experiments from the previous chapter, it is possible to determine the distributions in zeroth order since all setups start with monoenergetic electrons of energy ε_0. The initial condition then translates into $f_{e^-}^{(0)} = \delta(\varepsilon-\varepsilon_0)$ and $f_{e^+}^{(0)} = f_\gamma^{(0)} \equiv 0$. Subsequently, one can solve equation (6.1.1) in stages. In first order, the particle spectra can then be written as

$$\begin{aligned}
f_{e^-}^{(1)}(\varepsilon) &= t \cdot \left[\left.\frac{\mathrm{d}W_{\text{rad}}}{\mathrm{d}\varepsilon}\right|_{\varepsilon_0\to\varepsilon} - W_{\text{rad}}\,\delta(\varepsilon-\varepsilon_0) \right], \\
f_{e^+}^{(1)}(\varepsilon) &= 0, \\
f_\gamma^{(1)}(\varepsilon) &= t \cdot \left.\frac{\mathrm{d}W_{\text{rad}}}{\mathrm{d}\varepsilon}\right|_{\varepsilon_0\to\varepsilon_0-\varepsilon}.
\end{aligned} \tag{6.1.3}$$

The equations allow drawing several conclusions. First, the equation depicts that one does not generate positrons in first order. This is due to the fact that Breit-Wheeler pair production is here a two-step process: In the first step, electrons have to emit photons, which in turn can decay into electron-positron pairs. As there is in average only a single generation of secondary particles per

[1] It is noted that the dependence of the distribution functions on time t is not written explicitly.

[2] In the above notation, one always evaluates the differential photon emission rate at electron energies. Therefore, one inserts $\tilde{\varepsilon}$ (energy of the emitting electron) and $\tilde{\varepsilon}-\varepsilon$ in the case of the emission of a photon with energy ε [see upper equation in (6.1.1)].

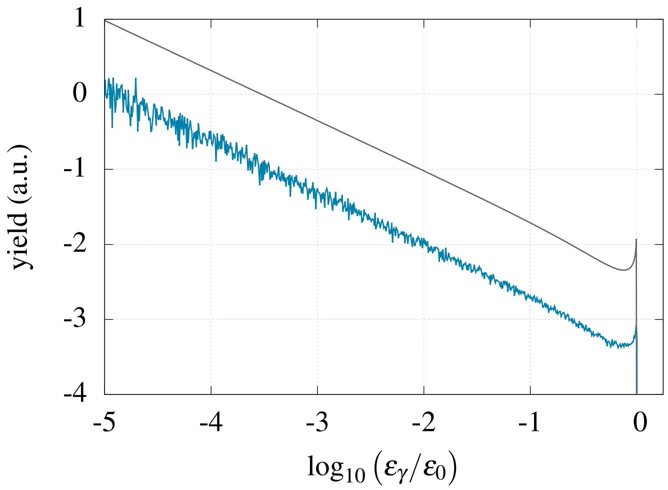

Figure 6.1.1: The log-log plot shows the differential photon emission rate for electrons with $\varepsilon_0 = 125$ GeV and $\chi_0 = 1600$ in gray and the photon spectrum generated by such electrons interacting with a clean attosecond pulse (duration 50 as). The vertical misalignment is ascribed to different normalizations used in both plots.

time $W^{-1}_{\mathrm{rad,\,pair}}$, positrons are expected in the second order of the perturbation theory. Second, the result of the electron and the photon spectrum is of great importance. This becomes particularly obvious when considering ultra-short interaction times, $W_{\mathrm{rad,\,pair}}\,\tau \ll 1$. Higher orders of the perturbation theory are suppressed under such circumstances with the result that the first-order contribution is a very good approximation to the full particle spectra. Notably, this enables a direct measurement of the differential photon emission rate from the electron and the photon spectrum. It should also be emphasized that this includes the regime $\alpha\chi^{2/3} \geq 1$ as no assumptions have been made so far on the differential QED rates. To corroborate the statement, the interaction of 125 GeV electrons with a clean attosecond pulse (duration 50 as) is investigated in the framework of a one-dimensional QED-PIC simulation. The supplement 'clean' means that the pulse has a perfect Gaussian temporal profile $a_0 e^{-(x-ct)^2/(2\sigma_\tau^2)}$. Here, σ_τ represents the pulse duration via $\tau = 2\sigma_\tau\sqrt{\ln(4)}$. The field strength a_0 is chosen such that maximum χ_e values of 1600 can be reached by the electrons. As the radiation time $W^{-1}_{\mathrm{rad}} = t_{\mathrm{rad}} \simeq 200$ as is rather long with respect to the pulse duration, it is expected that the photon spectrum reproduces the differential photon emission rate. Figure 6.1.1 shows the corresponding simulation results in blue (photon spectrum) and gray [Nikishov–Ritus differential photon emission rate for electrons with $\varepsilon_0 = 125$ GeV and $\chi_0 = 1600$, see equation (2.5.5)]. Overall, one can see that both the differential photon emission rate and the photon spectrum show the same behavior. They both obey a power law almost over the entire domain shown. Even the previously observed bump emerging at the high-energy cutoff can be identified in both plots. This strengthens the statement that the shape of the differential photon emission rate can be accurately reproduced by the photon spectrum if the interaction time is ultra-short in the above sense. The mismatch in height, in contrast, is ascribed to different normalization values for both quantities.

At this point, it is also clear that the previously observed power-law photon spectrum (see sections 5.2 and 5.3) is a direct consequence of the Nikishov–Ritus differential rates as they are applied in all simulations. Accordingly, it is not far to seek to take a closer look at these rates. Recalling the expression for the Nikishov–Ritus rates from equations (2.5.5) and (2.5.10), one finds that they depend mainly on $\mathrm{Ai}'(x)$, i.e. on the first derivative of the Airy function[3]. The Airy function and also its first derivative are exponentially suppressed for large arguments $x \gg 1$. It is therefore likely that only secondary particles with $x \lesssim 1$ contribute significantly to the spectra. In addition, the parameter x is symmetric around $\chi_\gamma/2$ for pair creation, attaining a minimum of $x_{\min} = (4/\chi_\gamma)^{2/3}$. In the following, the focus is thus laid on photons with $\chi_\gamma \gg 1$ for which the constraint $x \lesssim 1$ is ensured and even tightened to $x \ll 1$. From a physical perspective, it means that only photons having a relatively high decay probability will be taken into account afterwards, as they enable the development of an electromagnetic cascade. Such photons can only be generated by electrons and positrons with $\chi_e \gg 1$. The constraint $\chi \gg 1$ for all species therefore labels the lower limit of particles that control the spectra. On the other side, $x \ll 1$ requires the maximum quantum nonlinearity parameter to be much less than the initiating one χ_0. In fact, these limits can be translated into a range of particle energies for which the constraint $x \ll 1$ serves as a good approximation, $\varepsilon_0/\chi_0 \ll \varepsilon \ll \varepsilon_0$. On this energy interval, the Nikishov–Ritus differential QED rates can be simplified to [177]

$$\begin{aligned}
\left.\frac{\mathrm{d}W_{\mathrm{rad}}}{\mathrm{d}\varepsilon}\right|_{\tilde{\varepsilon}\to\varepsilon} &\simeq \frac{\nu}{\tilde{\varepsilon}^{4/3}} \frac{1+\eta^2}{\eta^{1/3}(1-\eta)^{2/3}} \left(\frac{H}{H_{\mathrm{crit}}}\right)^{2/3}, \\
\left.\frac{\mathrm{d}W_{\mathrm{pair}}}{\mathrm{d}\varepsilon}\right|_{\tilde{\varepsilon}\to\varepsilon} &\simeq \frac{\nu}{\tilde{\varepsilon}^{4/3}} \frac{\eta^2+(1-\eta)^2}{\eta^{1/3}(1-\eta)^{1/3}} \left(\frac{H}{H_{\mathrm{crit}}}\right)^{2/3},
\end{aligned} \tag{6.1.4}$$

where the abbreviations

$$\nu = -\frac{\alpha \mathrm{Ai}'(0)\left(m_e c^2\right)^{4/3}}{\hbar} \quad \text{and} \quad \eta = \frac{\varepsilon}{\tilde{\varepsilon}} \tag{6.1.5}$$

are introduced, and H represents the background field. Inserting the approximations back into equation (6.1.3), one finds that the spectra are supposed to scale as[4]

$$f_{e^-}^{(1)} \propto \varepsilon_e^{-1/3} \quad \text{and} \quad f_\gamma^{(1)} \propto \varepsilon_\gamma^{-2/3}. \tag{6.1.6}$$

Hence, the approximation features the power-law behavior and it is expected that a power-law index of $p = 2/3$ describes a large part of the photon spectrum if the interaction time is short. This coincides with the data of the photon spectrum in figure 6.1.1 whose index is very close to $p = 2/3$ when performing a linear fit. On the other hand, the power-law index is slightly smaller as predicted by the proposals ($p = 0.73$ for the non-perturbative QED collider and $p = 0.96$ for the attosecond pulse setup), indicating that the interactions are not short enough to be able to characterize the spectrum in first order. The same deduction can also be drawn with regard to positrons which were observed in the proposals, but are not comprised of the first-order result. Consequently, higher orders of the perturbation theory should be included. In this context, it is particularly important to understand how higher orders are formed from such a power-law behavior. For this reason, one inserts a power-law distribution function $f(\varepsilon) \propto \varepsilon^s$ into the Boltzmann equations (6.1.1) and uses additionally the approximations in equation (6.1.4). In doing so, it can straightforwardly be shown (see appendix A.3.1 for the details of the calculation) that any convolution in the Boltzmann equations with a power-law distribution gives again a

[3] As a brief reminder, the parameter is defined as $x = \left[\chi_\gamma/(\chi_e|\chi_e - \chi_\gamma|)\right]^{2/3}$.

[4] In the case of the electron spectrum, η is much less than unity for the considered energies. Conversely, it approaches unity in the case of the photon spectrum.

power-law distribution with reduced power-law index,

$$\left.\begin{aligned} \int_{\varepsilon}^{\infty} \mathrm{d}\tilde{\varepsilon}\, \tilde{\varepsilon}^{\,s}\, \frac{\mathrm{d}W_{\text{pair}}}{\mathrm{d}\varepsilon}\bigg|_{\tilde{\varepsilon}\to\varepsilon} \\ \int_{\varepsilon}^{\infty} \mathrm{d}\tilde{\varepsilon}\, \tilde{\varepsilon}^{\,s}\, \frac{\mathrm{d}W_{\text{rad}}}{\mathrm{d}\varepsilon}\bigg|_{\tilde{\varepsilon}\to\varepsilon} \\ \int_{\varepsilon}^{\infty} \mathrm{d}\tilde{\varepsilon}\, \tilde{\varepsilon}^{\,s}\, \frac{\mathrm{d}W_{\text{rad}}}{\mathrm{d}\varepsilon}\bigg|_{\tilde{\varepsilon}\to\varepsilon-\tilde{\varepsilon}} \end{aligned}\right\} \propto \varepsilon^{\,s-1/3}. \tag{6.1.7}$$

The same holds for any multiplication of the particle distribution functions with the total QED rates (see appendix A.3.2 for the details of the calculation),

$$\left.\begin{aligned} W_{\text{pair}}\,\varepsilon^{\,s} \\ W_{\text{rad}}\,\varepsilon^{\,s} \end{aligned}\right\} \propto \varepsilon^{\,s-1/3}. \tag{6.1.8}$$

Surprisingly, the transformation behavior is universal since the modified power-law index is always reduced by $1/3$ to $s-1/3$. Applying this to the perturbation theory, the spectra up to second order can be finally written as

$$\begin{aligned} f_{e^-}(\varepsilon) &\simeq a\varepsilon^{-1/3} + b\varepsilon^{-2/3} + c\varepsilon^{-1}, \\ f_{e^+}(\varepsilon) &\simeq d\varepsilon^{-1}, \\ f_{\gamma}(\varepsilon) &\simeq g\varepsilon^{-2/3} - h\varepsilon^{-1}. \end{aligned} \tag{6.1.9}$$

Here a, b, c, d, g, and h represent positive quantities that depend quadratically on time. It is further noted that the negative sign in front of h symbolizes those photons which have decayed into electron-positron pairs.

In order to test the predictions of the model, the interaction of electrons with a clean electromagnetic attosecond pulse (duration 150 as) is investigated numerically. The simulation parameters are the same as compared to the case in figure 6.1.1 except for the longer duration. Figure 6.1.2 shows the results of the one-dimensional simulation. More precisely, the photon spectrum is illustrated in blue, the merged seed- and pair-electron spectrum in black, and the positron spectrum in orange. Starting with the photon spectrum, a power law with an index of approximately $p = 0.77$ can be deduced from a linear fit to the data (see the linear function in blue)[5]. The index is close but not exactly equal to the first-order expectation $p = 2/3$, which indicates that more than one generation of photons already contributes to the spectrum. Nonetheless, the model correctly predicts the trend, namely that the spectrum drops off faster for longer interaction times. It is also interesting to note that the power-law index remains below the second-order contribution $p = 1$. From that, it follows that the spectrum lays well within the range predicted by the model. The same holds also for the electron spectrum. There, the fitting routine yields a power-law index $p \simeq 0.68$, which is in the range predicted by equation (6.1.9). The best agreement, however, is obtained in the case of the positron spectrum. The power-law index is approximately equal to $p = 0.99$ which is very close to the prediction of the model $p = 1$.

In conclusion, the analytical model allows the understanding of the particle spectra with reasonable accuracy, when the interaction time is short with respect to the characteristic time of the QED processes.

[5] It is noted that the fitting range has to respect the applicability range of the approximation. Applied to the present case, this is respected within the interval 125 MeV $< \varepsilon <$ 25 GeV.

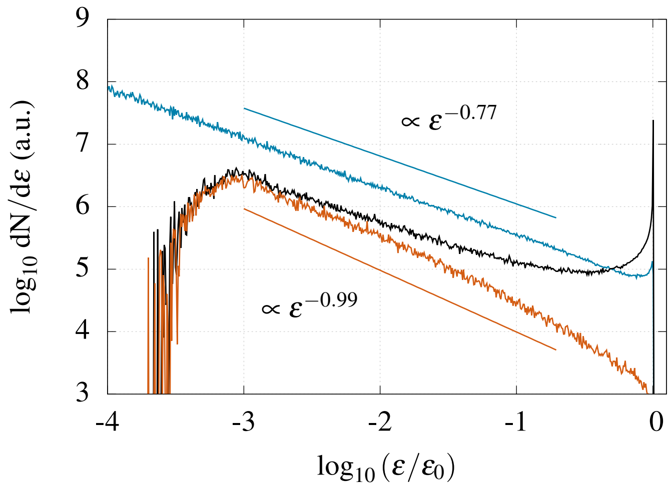

Figure 6.1.2: The plot shows the energy spectrum for electrons (black), photons (blue), and positrons (orange) obtained from the interaction of ultra-relativistic electrons ($\varepsilon_0 = 125$ GeV) with a clean attosecond pulse (duration 150 as). The intensity of the electromagnetic pulse is chosen such that a maximum quantum nonlinearity of $\chi_0 = 1600$ can be reached. The plot also contains linear fits predicting power-law indices of $p = 0.77$ for photons, $p = 0.68$ for electrons, and $p = 0.99$ for positrons in the energy range 125 MeV $< \varepsilon <$ 25 GeV.

6.2 Identifying non-perturbative QED effects from the particle spectra

The preceding section introduced an analytical model for the particle spectra generated in supercritical and ultra-short interactions. To some extent, the model builds up on the Nikishov–Ritus theory. As this theory is conjectured to break at $\alpha\chi^{2/3} \simeq 1$, both the particle spectra and the model simultaneously provide opportunities to identify (fully) non-perturbative QED. How this basically works will be explained in the following.

6.2.1 Shape of the particle spectra

A first opportunity was already given in the previous section. If the interaction time is ultra-short in the sense that the spectrum can be described by the first-order approximation, the photon spectrum directly gives the differential photon emission rate. A simple comparison with the Nikishov–Ritus theory would then indicate whether, and if where, non-perturbative QED effects are significant. In addition to that, the shape of the particle spectra can also be helpful when the spectra go beyond the first order. One can deduce from equation (6.1.4) that the scaling of the Nikishov–Ritus rates in fields of different strengths is the same as long as the interaction stays in the supercritical regime $\chi \gg 1$. As the shape of the differential QED rates is essential for the shape of the particle spectra, the shape of the spectra should also be comparable. To illustrate that, the interaction of ultra-relativistic electrons ($\varepsilon_0 = 125$ GeV) with a clean attosecond pulse ($\tau = 150$ as) of two different strengths is considered numerically. Figure 6.2.1 shows the photon spectra for the interaction with peak amplitudes chosen such that electrons experience either

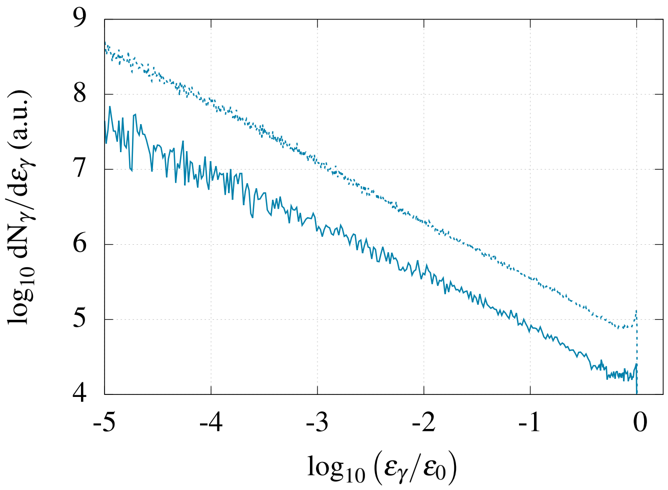

Figure 6.2.1: One-dimensional simulation results for the spectra of photons obtained from the interaction of ultra-relativistic electrons ($\varepsilon_0 = 125$ GeV) with a clean 150-attosecond pulse of different strengths. In particular, the peak field is such that the electrons can reach $\chi_0 = 1600$ (dotted) and $\chi_0 = 160$ (solid).

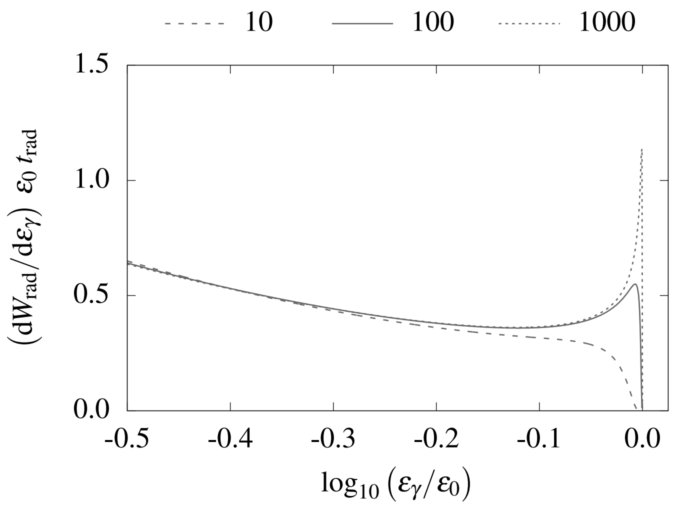

Figure 6.2.2: Nikishov–Ritus differential photon emission rate for electrons with $\chi_0 = 10$ (dashed), $\chi_0 = 100$ (solid), and $\chi_0 = 1000$ (dotted). Please note that each emission rate is normalized such that the area under all plots is unity.

$\chi_0 = 160$ (solid) or $\chi_0 = 1600$ (dotted). Again, one can see that both spectra follow a power law. Even though a closer look reveals a slight deviation in the power-law indices—especially at low energies—the overall shape of the spectra remains the same. Now, the Nikishov–Ritus theory is more likely to fail at $\chi_0 = 1600$ as $\alpha\chi_0^{2/3} \simeq 1$. At $\chi_0 = 160$, $\alpha\chi_0^{2/3} \simeq 0.2$, in contrast, the formulas may still be applicable at least up to a certain extent. It means that if the experimental photon spectra will not agree in shape, this may be a clear hint to entering the fully non-perturbative regime of QED. This may also give insights in which part of the spectrum the theory fails.

A further feature is the aforementioned bump in the photon spectrum that arises in the vicinity of the initial electron energy. The bump in itself appears counter-intuitively as the electron is likely to emit all its energy in a single emission. Therefore, the bump has recently gained interest by Tamburini and Meuren [178]. Based on the discussion so far it should be clear that the bump originates from the Nikishov–Ritus differential photon emission rate (see figure 6.1.1), and can formally be set in relation to the $\eta^{1/3}$ term emerging in equation (6.1.4) (η tends to zero when the energy of the emitted photon approaches the initial electron energy). Fortunately, the exact details of the bump depend on the quantum nonlinearity parameter of the initiating electron χ_0. For example, the bump gets more pronounced with increasing χ_0. To show that, figure 6.2.2 depicts the Nikishov–Ritus differential photon emission rate for three different values of χ_0: 1000 (dotted), 100 (solid), and 10 (dashed). Clearly, the bump can be seen to be highest and sharpest in the strongest field. Thereby, it exceeds the case $\chi_0 = 100$ significantly. In the weakest field $\chi_0 = 10$, in contrast, the bump cannot be observed at all. This qualitative behavior is retained in the photon spectrum. A close look at the spectra in figure 6.2.1 reveals the bump to be more pronounced in the stronger field. Additionally, the non-existence of the bump at low χ_0 can be seen in figure 5 from [163]. This is in agreement with the findings in [178], where the bump was reported to emerge only in fields with $\chi_0 > 16$. Moreover, it was found that the height of the bump increases monotonically with χ_0. As both the shape and the existence of the bump depend on χ_0, it represents an implicit observable for the physics of the interaction, and may thus be used as a signature for non-perturbative QED. Following [178] once more, the bump also disappears when the interaction time is too long in the above sense, so that the spectrum gets dominated by multiple emissions. Here, one can take the photon spectrum for the generated attosecond pulse as an example (see figure 5.3.6). Based on the pre-pulse, the interaction time was extended resulting in the suppression of the bump. However, even the spectra originated from multiple generations of secondary particles can be used to identify fully non-perturbative QED. The next section will pick up that point in the context of the $H^{2/3}-$correspondence.

6.2.2 The $H^{2/3}-$correspondence

The following part introduces the so-called $H^{2/3}-$correspondence, which has versatile consequences. First, it motivates the global constant field approximation used before. In that context, it also allows the reproduction of particle spectra through simple and fast one-dimensional simulations. And second, it may have the potential to identify significant deviations in the QED probability distributions for $\chi \gg 1$ from the particle spectra.

In order to understand the concept, one first puts the perturbation theory with respect to the interaction time in the rear and starts again with the coupled Boltzmann equations (6.1.1) instead. As already mentioned previously, one can formally express the solution of the Boltzmann equations in terms of time-ordered exponentials in the general case [176]. The particle distribution functions at time t are thus determined by a time integral over the (differential) QED probability rates. A closer look at these rates reveals that the dependence on the external field is universal in the case $\chi \gg 1$ [see equations (2.5.7), (2.5.12), and (6.1.4)]. To be more precise, the rates are directly proportional to $H^{2/3}$. This in turn leads to the following hypothesis. If there are two distinct systems in which electrons from the same source interact with two different fields, namely in system 1 with field $H_1(t)$ and in system 2 with field $H_2(t)$, then the particle distribution functions at time t will coincide when

$$\int_0^t \mathrm{d}t'\, H_1^{2/3}(t') = \int_0^t \mathrm{d}t'\, H_2^{2/3}(t') \tag{6.2.1}$$

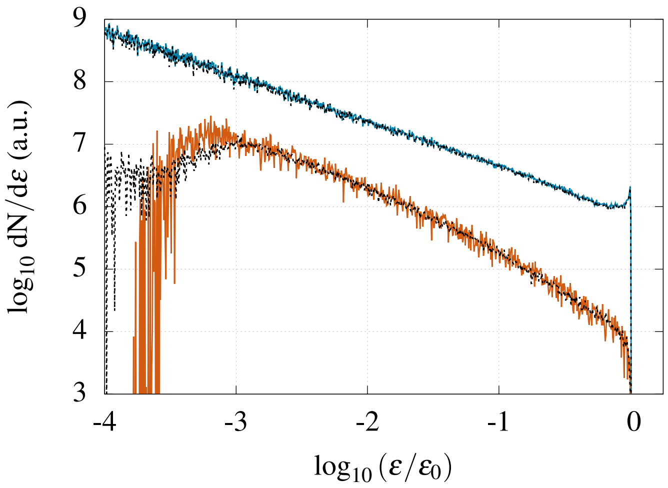

Figure 6.2.3: One-dimensional simulation results for the spectra of photons (blue) and positrons (orange) obtained from the interaction of ultra-relativistic electrons ($\varepsilon_0 = 125$ GeV) with a clean attosecond pulse (duration 78 as). This duration translates into a rms length of 10 nm. In this way, one can reproduce the spectra for the non-perturbative QED collider (dotted plots, see also figures 5.2.6 and 5.2.8). Note that the plots are vertically adjusted to match in height.

holds[6]. This is the so-called $H^{2/3}-$correspondence which has several interesting implications. For instance, it suggests that the exact shape of the electromagnetic field is not of prior importance in the supercritical regime $\chi \gg 1$, since the final particle spectra can be simply reproduced on condition that equation (6.2.1) is fulfilled. This motivates the globally constant field assumption and simultaneously opens up the possibility of modeling the particle spectra in complex physical systems through much simpler geometries. As an example, simulating the non-perturbative QED collider in three dimensions (see section 5.2) is extremely time- and storage-consuming from a computational point of view. The final particle spectra, however, can be reproduced by simple one-dimensional simulations, which are considerably faster and smaller in storage. In order to check that, a one-dimensional simulation modeling the interaction of an ultra-relativistic electron beam ($\varepsilon_0 = 125$ GeV) with a clean attosecond pulse is conducted. The duration ($\tau \simeq 78$ as) and the peak strength of the pulse match the field of the non-perturbative QED collider, implying that equation (6.2.1) is fulfilled. Figure 6.2.3 presents the results for the particle spectra. In particular, the solid lines (photons in blue and positrons in orange) represent the data from the one-dimensional simulation, whereas the black dotted lines correspond to the fully three-dimensional simulation (see also figures 5.2.6 and 5.2.8). One can directly see that apart from the low-energetic positrons the shapes of the spectra are in perfect agreement. It should be stressed that the total yield in the spectra (ordinate), however, depends on the details of the configuration—such as number of initial electrons—and was adjusted in the figure to better visualize the coincidence. Further, the difference at low energies is not unexpected[7] because this part of the spectrum is not covered by the model approximations.

As a second example, one considers the interaction between the ultra-relativistic electrons with the self-consistently generated attosecond pulse (see section 5.3). Although the duration of the

[6] In that case, electrons with $\chi_e \gg 1$ lose in total the same amount of energy in both systems [see equation (2.5.9)].

[7] To be more precise, it results from the transverse motion of positrons being subjected to the focusing forces of the opposing electron beam.

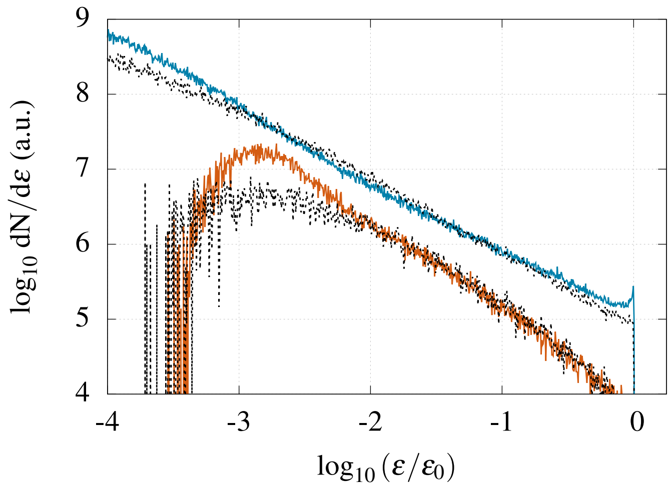

Figure 6.2.4: One-dimensional simulation results for the spectra of photons (blue) and positrons (orange) obtained from the interaction of ultra-relativistic electrons ($\varepsilon_0 = 125$ GeV) with a clean attosecond pulse (duration 350 as). This duration characterizes the interaction with the self-consistently generated attosecond pulse from section 5.3 including the pre-pulse. The dotted lines represent the full results obtained from two-dimensional simulations (see also figure 5.3.6). Data published in [163].

main pulse is relatively short ($\tau \approx 150$ as), the power-law indices describing e.g. the photon spectrum do not comply well with the second-order model. Following the correspondence principle, the main pulse is expected to produce a photon spectrum with $p \simeq 0.77$ (see figure 6.1.2 as a reference) rather than $p \simeq 0.97$ (see figure 5.3.6). The reason for that difference is the pre-pulse which is too long to be neglected. Fortunately, the main part of the particle spectra can be reconstructed in simple one-dimensional simulations when the $H^{2/3}-$correspondence is applied as follows. In the first step, one calculates the integral of $H^{2/3}$ along the electron trajectory. In the second step, one chooses the duration of a clean Gaussian attosecond pulse in such a way that the time integral over $H^{2/3}$ matches the one along the electron trajectory. Applied to the self-consistently generated pulse from section 5.3 and under the assumption of same peak strengths, one obtains an effective duration of $\tau \approx 350$ as. The spectra resulting from the interaction of such a pulse with 125 GeV electrons are given in figure 6.2.4 as solid lines together with the full results (dotted lines, see also figure 5.3.6). It can be seen that the spectra can be reproduced with reasonable accuracy in the energy range of interest. It is further noted that a comparison with the spectra generated by a pulse of 150 as duration (see figure 6.1.2) gives insights into the role of the main and pre-pulse on the distribution of particles with $\chi \gg 1$.

The examples above support the applicability of the $H^{2/3}-$correspondence. Hence, it will be addressed in the following how the correspondence principle can be valuable for the identification of impactful high-order radiative corrections. In this context suppose that one of the experiments proposed in chapter 5 has been performed and the interaction geometry suggests that only a few generations of secondary particles contribute to the spectra[8]. One can then try to reproduce the experimental particle spectra through simple and fast one-dimensional sim-

[8] The proposal in section 5.4 should be considered more carefully due to the long total interaction time which results from the tail of the optical laser pulse.

ulations by adjusting the effective duration of a clean attosecond pulse until one observes a coincidence of the experimental and simulation data. If this simple reconstruction of the particle spectra via one-dimensional simulations is impossible, this will indicate the failure of the $H^{2/3}-$correspondence. From a theoretical viewpoint, the failure of the $H^{2/3}-$correspondence implies the break of the Nikishov–Ritus formulae as a result of entering a regime where high-order radiative corrections become impactful. Depending on which part of the spectrum cannot be recovered, one may also get information which part of the theory requires an amendment.

6.3 Summary

The preceding chapter dealt with the analytic modeling of energy spectra generated during the interaction of ultra-relativistic particles with highly supercritical fields. Boltzmann equations describing the temporal evolution of the spectra served as a starting point for the analysis. Under the assumption of ultra-short interactions in the sense that only a few generation of secondary particles are expected, it was possible to solve the equations through an ansatz in the form of perturbation theory. Importantly, it was found that in first-order perturbation theory the photon spectrum coincides with the differential photon emission rate [see equation (6.1.3)]. Experimentally, this is a powerful matter of fact as it allows the direct measurement of the QED probability rate from the photon spectrum, including also the unknown regime of highly supercritical fields. In order to understand the spectra from the simulations in detail (see sections 5.2 and 5.3), the focus was then laid on the Nikishov–Ritus probability rates. In fact, the first-order result in the case of the standard Nikishov–Ritus theory yielded power-law particle spectra [see equation (6.1.6)], but it was not able to correctly predict the power-law indices as observed in simulations. Furthermore, it was also not possible to exhibit information on the positron spectrum as pair creation is a two step process. The model was therefore extended by incorporating contributions up to the second order of the perturbation theory. The subsequent comparison with the simulated spectra pointed out that the second-order model suffices in understanding the main features of the particle spectra. Particularly notable in that regard is the power-law index belonging to the positron spectrum, which was in excellent agreement with the prediction of the second-order model [see equation (6.1.9) and figure 6.1.2].

The second part of the chapter addressed the question how one could prove the entrance of (highly) supercritical regimes from experimental data. It was argued that within the Nikishov–Ritus theory the particle spectra retain their shape when being generated in supercritical fields. Simple comparisons between experimental spectra in fields of different strengths would then reveal whether, and if where, the current theory lacks. A further observable was the bump emerging in the high-energy part of the photon spectrum. Its properties depend on the quantum nonlinearity parameter of the probing electrons and thus could give information about the physics. Moreover, the $H^{2/3}-$correspondencee was introduced as an attractive tool. The correspondence principle enabled the reproduction of particle spectra through simple and fast one-dimensional simulations, provided that the time integral over $H^{2/3}$ in the one-dimensional simulation matches the integral in the proper system [see equation (6.2.1)]. It was elaborated that if one-dimensional simulations cannot reproduce the experimental spectra, this will indicate the failure of the $H^{2/3}-$correspondence and so indicates a break of the Nikishov–Ritus theory.

7 Conclusion

The present thesis investigated high intensity laser–plasma interactions with special focus on how they can be exploited in order to explore and advance QED, the fundamental theory describing the interaction of charged particles with electromagnetic fields.

Chapter 2 started with a description about the theoretical background which is necessary for the interpretation of the results. As the majority of these results were obtained in the framework of numerical simulations, chapter 3 gave a comprehensive overview of the applied particle-in-cell (PIC) technique. In that regard, section 3.3.1 explained in detail how the dominant QED effects, namely γ-photon emission and (multi-photon) Breit-Wheeler pair production, are implemented into the PIC code `VLPL`. Through a series of test simulations, it was afterwards shown that the QED module works properly (see section 3.3.2), so truly strengthening the reliability in QED-PIC simulations performed with the code `VLPL`.

Physically relevant results were then presented in chapter 4, where the interaction of two circularly polarized and counter-propagating high-intensity laser pulses with a thin plasma foil was studied. It was seen that radiation reaction can strongly alter the electron dynamics. When radiation reaction is included in the simulations, it became possible to trap electrons in the nodes of the electric field emerging from the superposition of the counter-propagating waves. In a second step, the focus was laid on the robustness of this *normal radiative trapping* with respect to the intensity of the irradiating laser pulses. The simulations indicated that the radiative trapping breaks when the intensity gets too large ($a_0 \gtrsim 800$). Physically, the increasing role of the pair production process with increasing intensity turned out to be driving force. Pairs were created so efficiently that the generated electron-positron plasma turned opaque, which in turn caused a break of the standing-wave structure and so the break of radiative trapping.
In a further study, it was discussed how the radiative trapping is affected when twisted light is used instead. The twisted light was modeled by means of two circularly polarized Laguerre–Gaussian laser beams. Supported by analytics and simulations it was shown that under appropriately chosen mode parameters, the electric nodes of the emerging standing wave took on the form of a helix. In that way, it was possible to trap electrons along a helical path. The simulations further revealed that circularly polarized Laguerre–Gaussian beams can be used to drive electron structures with ultra-short durations on the attosecond level. Depending on the laser mode parameters, these structures can either be disk-like electron bunches or helical electron beams. The emergence of these structures could finally be understood after introducing the total angular momentum $j = m + s$ per laser photon, where m describes the azimuthal Laguerre index and s the handedness of the laser pulse.

Chapter 5 continued with the question of how the highly supercritical regime of QED, which so far is not covered by any theory and was previously considered as inaccessible, could soon be brought into experimental reach. The key task involved the reduction of the electromagnetic field's switching time, in order to mitigate radiation losses of ultra-relativistic electrons as much as possible. The present thesis addressed in total three promising geometries. First, it was discussed that a future electron-electron collider can prove beneficial when the beam parameters are as follows (see section 5.2): each electron beam has an energy of 125 GeV (per particle), carries a peak current of 1.7 MA, is focused to a radius of 10 nm, and has also a length of 10 nm. Second, it was elaborated that one can indirectly tackle the highly supercritical regime with high-intensity optical laser radiation (see section 5.3). By means of high-harmonic generation at an over-dense plasma surface, the optical laser radiation was found to be convertible into an ultra-intense attosecond pulse. In the simulation, the converted pulse had a duration of 150 as and a peak intensity of 10^{24} Wcm^{-2}. The head-on collision with 125 GeV electrons emphasized the feasibility of the setup. And third, section 5.4 brought a combined laser-plasma, laser-beam configuration into play. The idea based on the shielding properties of an over-dense plasma. There, a laser pulse can only penetrate up to the skin depth. In that way, it was possible to limit the penetration depth of an optical laser pulse with intensity 5.4×10^{24} Wcm^{-2} to an ultra-thin surface of roughly 20 nm at the front of a solid-dense diamond target. The highly supercritical regime was finally shown to be in reach for 125 GeV electrons, moving collinearly to the optical pulse.

After showing that highly supercritical fields could in principle be probed, the final chapter 6 addressed the point of how the successful realization can be identified from experimental observables. As such, the particle spectra generated during the interaction were concluded to be appropriate. For that reason, it was aimed at modeling the spectra also analytically in order to understand them in detail. In that regard, it was found that the photon spectrum will match the differential photon emission rate if the interaction is ultra-short. Experimentally, this is obviously desirable, especially because it also includes the unexplored highly supercritical regime. Moreover, it was demonstrated that the shape of all particle spectra can be understood when only a few generations of secondary particles contribute. In regard of identifying the highly supercritical regime, the $H^{2/3}-$correspondence principle was introduced as a powerful approach. It was based on perturbative QED by means of the Nikishov–Ritus theory, and indicated the possibility of reproducing experimental particle spectra through simple and fast one-dimensional simulations with clean Gaussian pulses of appropriate duration. If one-dimensional simulations will not suffice in recovering the experimental spectra, this implies the break of the Nikishov–Ritus theory and so the entrance of the fully non-perturbative regime of QED.

In conclusion, it could be seen that laser–plasma interactions are quite multifaceted. On the one hand, they could be used to study how and when QED effects alter the collective plasma behavior, so allowing the exploration of QED directly in the plasma (see, for instance, chapter 4). On the other hand, one could make use of plasma and its unique properties to create suitable configurations in which QED could subsequently be probed (see, for instance, chapter 5). In the future, this variety will make high intensity laser–plasmas to an absolutely essential tool for exploring QED.

A Appendix

A.1 Longitudinal field profile of a Laguerre–Gaussian beam

The dependence of the transverse field on the transverse coordinates y and z comes along with a longitudinal field component in order to fulfill Gauss law in vacuum, div $\mathbf{E} = 0$. Thus, the laser field needs to ensure

$$-\partial_x E_x = \partial_y E_y + \partial_z E_z. \tag{A.1.1}$$

Based on the symmetry, it makes sense to express the transverse Cartesian derivatives through radius r and azimuth angle φ. Then, the right hand side of the above equation transforms into

$$-\partial_x E_x = \left(\cos(\varphi)\,\partial_r - \frac{\sin(\varphi)}{r}\,\partial_\varphi\right) E_y + \left(\sin(\varphi)\,\partial_r + \frac{\cos(\varphi)}{r}\,\partial_\varphi\right) E_z. \tag{A.1.2}$$

Without loss of generality, the calculation is shown for the right-moving wave from equation (4.3.1). Inserting that equation with the abbreviation $E_p^{|m|}(r,x) \equiv E_p^{|m|}$ for the upper line into equation (A.1.1) gives after some math

$$\begin{aligned} -\partial_x E_x = &\left(\frac{\partial E_p^{|m|}}{\partial r} - ms\,\frac{E_p^{|m|}}{r}\right) \sin\left(\omega_0 t - k_0 x - (m+s)\varphi + \phi_p^{|m|}\right) \\ &+ E_p^{|m|}\,\frac{\partial \phi_p^{|m|}}{\partial r} \cos\left(\omega_0 t - k_0 x - (m+s)\varphi + \phi_p^{|m|}\right). \end{aligned} \tag{A.1.3}$$

It is noted that the relations $s^2 = 1$, $\cos(\varphi) = \cos(s\varphi)$, $s\sin(\varphi) = \sin(s\varphi)$, as well as additional theorems for trigonometric functions are utilized to obtain equation (A.1.3). The longitudinal field component E_x can then be obtained by integrating equation (A.1.3) with respect to x. However, the transverse fields are given in paraxial approximation, so that the same must hold for the longitudinal component to be consistent. In that approximation, the variation of the field profile can be neglected on the scale determined by the wavelength. As a consequence, the integral over x simplifies significantly as one only considers the $k_0 x$ dependence. Eventually, the integral is trivial and one has

$$\begin{aligned} k_0 E_x = &\left(ms\,\frac{E_p^{|m|}}{r} - \frac{\partial E_p^{|m|}}{\partial r}\right) \cos\left(\omega_0 t - k_0 x - (m+s)\varphi + \phi_p^{|m|}\right) \\ &+ E_p^{|m|}\,\frac{\partial \phi_p^{|m|}}{\partial r} \sin\left(\omega_0 t - k_0 x - (m+s)\varphi + \phi_p^{|m|}\right). \end{aligned} \tag{A.1.4}$$

A.2 Angular momentum of electromagnetic fields

This part of the appendix is meant to show that in vacuum one typically separates the total angular momentum of a localized electromagnetic field into two contributions; one that can be ascribed to the *spin* of the radiation field, and the other that represents an *orbital* contribution.

A.2.1 Orbital and spin angular momentum of electromagnetic fields

In classical electrodynamics one can determine the angular momentum of the radiation field from the formula [17]

$$\mathbf{L} = \frac{1}{4\pi c}\int \mathrm{d}V\, \mathbf{x}\times(\mathbf{E}\times\mathbf{B})\,. \tag{A.2.1}$$

In order to obtain the separation into two contributions, it is now convenient to express the magnetic field in terms of the vector potential $\mathbf{A}$. Inserting $\mathbf{B} = \mathrm{rot}\,\mathbf{A} = \nabla\times\mathbf{A}$ into equation (A.2.1) gives the triple cross product

$$\mathbf{x}\times\Big(\mathbf{E}\times(\nabla\times\mathbf{A})\Big). \tag{A.2.2}$$

which needs to be addressed in more detail. Most easily, this can done with the help of the Levi-Civita symbol. Applying additionally Einstein's sum convention, the triple cross product can then be written as

$$\begin{aligned}\mathbf{x}\times\Big(\mathbf{E}\times(\nabla\times\mathbf{A})\Big) &= \hat{\mathbf{e}}_i\,\varepsilon_{ijk}\,x_j\Big(\mathbf{E}\times(\nabla\times\mathbf{A})\Big)_k\\ &= \hat{\mathbf{e}}_i\,\varepsilon_{ijk}\,\varepsilon_{klm}\,x_jE_l\,(\nabla\times\mathbf{A})_m\\ &= \hat{\mathbf{e}}_i\,\varepsilon_{ijk}\,\varepsilon_{klm}\,\varepsilon_{mno}\,x_jE_l\,(\partial_nA_o)\,.\end{aligned} \tag{A.2.3}$$

To further advance the derivation one should notice that $\varepsilon_{mno} = \varepsilon_{nom}$. This allows the use of the identity $\varepsilon_{klm}\,\varepsilon_{nom} = \delta_{kn}\delta_{lo} - \delta_{ko}\delta_{ln}$, where δ represents the Kronecker delta. With this in mind it is possible to perform explicitly the sums over the indices n and o, which results in

$$\mathbf{x}\times\Big(\mathbf{E}\times(\nabla\times\mathbf{A})\Big) = \hat{\mathbf{e}}_i\,\varepsilon_{ijk}\Big[x_jE_l\,(\partial_kA_l) - x_jE_l\,(\partial_lA_k)\Big]. \tag{A.2.4}$$

In vector notation, the first summand on the right-hand side of equation (A.2.4) can now be written as

$$\hat{\mathbf{e}}_i\,\varepsilon_{ijk}\,x_jE_l\,(\partial_kA_l) = E_l\,(\mathbf{x}\times\nabla)\,A_l. \tag{A.2.5}$$

Up to here, the angular momentum is equal to

$$\mathbf{L} = \frac{1}{4\pi c}\int \mathrm{d}V\Big[E_l\,(\mathbf{x}\times\nabla)\,A_l - \hat{\mathbf{e}}_i\,\varepsilon_{ijk}\,x_jE_l\,(\partial_lA_k)\Big]. \tag{A.2.6}$$

Through an integration by parts over the variable x_l and using the fact that the field is localized in space, $|\mathbf{E}|, |\mathbf{A}| \to 0$ for $|\mathbf{x}| \to \infty$, one can write the second part in equation (A.2.6) as

$$-\hat{\mathbf{e}}_i\,\varepsilon_{ijk}\int \mathrm{d}V\; x_jE_l\,(\partial_lA_k) = \hat{\mathbf{e}}_i\,\varepsilon_{ijk}\int \mathrm{d}V\;\partial_l\,(x_jE_l)\,A_k. \tag{A.2.7}$$

This can be simplified by explicitly taking the derivative $\partial_l\,(x_jE_l) = \delta_{jl}E_l + x_j\partial_lE_l = \delta_{jl}E_l$. In the last step the term ∂_lE_l was identified as $\nabla\cdot\mathbf{E}$, which is identically zero in vacuum. Then, equation (A.2.7) is obviously equal to

$$-\hat{\mathbf{e}}_i\,\varepsilon_{ijk}\int \mathrm{d}V\; x_jE_l\,(\partial_lA_k) = \int \mathrm{d}V\,(\mathbf{E}\times\mathbf{A})\,. \tag{A.2.8}$$

Putting everything together, the angular momentum of spatially localized fields can be calculated from

$$\mathbf{L} = \underbrace{\frac{1}{4\pi c}\int \mathrm{d}V\,(\mathbf{E}\times\mathbf{A})}_{\mathbf{L}_{\text{spin}}} + \underbrace{\frac{1}{4\pi c}\int \mathrm{d}V\,E_l\,(\mathbf{x}\times\nabla)A_l}_{\mathbf{L}_{\text{orbital}}}. \tag{A.2.9}$$

One can see that the angular momentum consists of two contributions. Apparently, the first contribution depends only on the field itself and not explicitly on the coordinate $\mathbf{x}$. It therefore seems to be an intrinsic property of the field, and thus this part is commonly interpreted as the *spin* of the radiation field. The second contribution, in contrast, does have an explicit dependence on $\mathbf{x}$. This part is frequently referred to as *orbital* angular momentum, which is basically motivated by the term $\mathbf{x}\times\nabla$ that resembles the quantum mechanical orbital angular momentum operator.

A.2.2 Total angular momentum of a circularly polarized Laguerre–Gaussian beam

In the following subsection, equation (A.2.9) will be applied for the case of a circularly polarized Laguerre–Gaussian beam as defined in equation (4.3.1)[1]. In particular, the main interest is on the angular momentum L_x which is carried along the propagation axis x. In order to perform the calculation, knowledge about the vector potential $\mathbf{A}$ is essential as can seen from equation (A.2.9). If the gauge is chosen such that the scalar potential ϕ is equal to zero, one can determine the vector potential through direct integration of $\mathbf{E}$ over time. Under the assumption that the temporal envelope of the laser field varies slowly with respect to the laser period[2], one can further neglect the time dependence of the pulse envelope in first order. In doing so, one first considers the *spin* contribution. When again abbreviating the upper line in equation (4.3.1) with $E_p^{|m|}(r,x)$, it reads

$$\begin{aligned} L_{\text{spin},x} &= \frac{1}{4\pi c}\int \mathrm{d}V\,(\mathbf{E}\times\mathbf{A})_x = \frac{1}{4\pi c}\int \mathrm{d}V\,(E_yA_z - E_zA_y) \\ &= \frac{s}{4\pi\omega_0}\int \mathrm{d}V\,E_p^{|m|}(r,x)^2\,. \end{aligned} \tag{A.2.10}$$

The contribution is proportional to the handedness s of the laser field as expected. Next, one continues with the *orbital* contribution for which one first takes a closer look at the x-component of the operator $(\mathbf{x}\times\nabla)$. As the field components are expressed in cylindrical coordinates [see equation (4.3.1)], it is not far to seek to do the same for $(\mathbf{x}\times\nabla)_x$. In doing so, one has $(\mathbf{x}\times\nabla)_x = \partial_\varphi$. In total, one can thus write

$$\begin{aligned} L_{\text{orbital},x} &= \frac{1}{4\pi c}\int \mathrm{d}V\,E_l\,(\mathbf{x}\times\nabla)_x A_l = \frac{1}{4\pi c}\int \mathrm{d}V\,E_l\left(\partial_\varphi A_l\right) \\ &= \frac{m}{4\pi\omega_0}\int \mathrm{d}V\,E_p^{|m|}(r,x)^2 + \frac{(m+s)}{4\pi\omega_0}\int \mathrm{d}V\,E_x(r,x)^2\,. \end{aligned} \tag{A.2.11}$$

One can see that the contribution of the transverse fields is proportional to m. However, there is an unexpected contribution that depends on $(m+s)$. The strict separation as done above is

[1] Equation (4.3.1) describes two waves; one that propagates along the positive and the other that propagates along the negative x-axis. Without loss of generality, the calculation is performed for the former wave.

[2] Physically, this means that the laser duration τ is much longer than the laser period T_0.

thus only correct if one neglects the longitudinal components in the second term. In general, however, one can still draw the conclusion that the total angular momentum is proportional to $j = m + s$. This can be seen when adding $L_{\text{spin},x}$ and $L_{\text{orbital},x}$ with the result

$$L_x = \frac{(m+s)}{4\pi\omega_0} \int \mathrm{d}V\, \mathbf{E}^2. \tag{A.2.12}$$

Interestingly, the integral is closely related to the total energy of the laser field.

A.3 Deriving the transformation rules for power-law functions in the Boltzmann equations

The last part of the appendix discusses the evolution of power-law distribution functions in the Boltzmann equation in the case of supercritical fields.

A.3.1 Convolution of a power-law distribution function and the differential QED rates

For the derivation of the analytic model in section 6.1, it was crucial to show that each convolution in the Boltzmann equation with a power-law function transforms into another power-law function. To prove this, one starts with the equations in (6.1.7) and inserts the approximation for the differential QED rates from equation (6.1.4). In doing so, the first line in equation (6.1.7) reads

$$\int_{\varepsilon}^{\infty} \mathrm{d}\tilde{\varepsilon}\, \tilde{\varepsilon}^{s} \left.\frac{\mathrm{d}W_{\text{pair}}}{\mathrm{d}\varepsilon}\right|_{\tilde{\varepsilon}\to\varepsilon} = \nu \left(\frac{H}{H_{\text{crit}}}\right)^{2/3} \int_{\varepsilon}^{\infty} \mathrm{d}\tilde{\varepsilon}\, \tilde{\varepsilon}^{s} \frac{1}{\tilde{\varepsilon}^{4/3}} \frac{\eta^2 + (1-\eta)^2}{\eta^{1/3}(1-\eta)^{1/3}}, \tag{A.3.1}$$

where $\eta = \varepsilon/\tilde{\varepsilon}$. It is thus convenient to integrate over η instead of $\tilde{\varepsilon}$. Merging the prefactors of the integral in the variable $\tilde{\nu}$, performing the substitution, and simplifying as much as possible, one can write the integral as

$$\tilde{\nu}\, \varepsilon^{s-1/3} \int_0^1 \mathrm{d}\eta\, \frac{1}{\eta^{s+1}} \frac{\eta^2 + (1-\eta)^2}{(1-\eta)^{1/3}} \propto \varepsilon^{s-1/3}. \tag{A.3.2}$$

The remaining integral does not depend either on ε or on $\tilde{\varepsilon}$ so that the result is proportional to $\varepsilon^{s-1/3}$. However, it is important to discuss the conditions under which the integral converges because the integrand diverges at both the upper and the lower bound of integration. The divergence at $\eta \to 1$ is not problematic as it is integrable. In contrast to that, the integrand scales like η^{-s-1} at the lower bound which may cause a divergence for $s \geq 0$. Recapitulating that only the photon distribution function couples to $\left.(\mathrm{d}W_{\text{pair}}/\mathrm{d}\varepsilon)\right|_{\tilde{\varepsilon}\to\varepsilon}$, the integral A.3.2 converges eventually since the power-law index in first order is $s = -2/3$.
In the same manner, one obtains for the middle part in equation (6.1.7)

$$\begin{aligned} \int_{\varepsilon}^{\infty} \mathrm{d}\tilde{\varepsilon}\, \tilde{\varepsilon}^{s} \left.\frac{\mathrm{d}W_{\text{rad}}}{\mathrm{d}\varepsilon}\right|_{\tilde{\varepsilon}\to\varepsilon} &= \tilde{\nu} \int_{\varepsilon}^{\infty} \mathrm{d}\tilde{\varepsilon}\, \tilde{\varepsilon}^{s} \frac{1}{\tilde{\varepsilon}^{4/3}} \frac{1+\eta^2}{\eta^{1/3}(1-\eta)^{2/3}} \\ &= \tilde{\nu}\, \varepsilon^{s-1/3} \int_0^1 \mathrm{d}\eta\, \frac{1}{\eta^{s+1}} \frac{1+\eta^2}{(1-\eta)^{2/3}} \propto \varepsilon^{s-1/3}. \end{aligned} \tag{A.3.3}$$

Following the same line of argument as above, one can deduce that the integral converges because $(\mathrm{d}W_{\mathrm{rad}}/\mathrm{d}\varepsilon)|_{\tilde{\varepsilon}\to\varepsilon}$ couples to the electron and positron distribution functions which scale as $\tilde{\varepsilon}^{-1/3}$ and 0, respectively.
Lastly, one finds

$$\begin{aligned}\int_{\varepsilon}^{\infty} \mathrm{d}\tilde{\varepsilon}\, \tilde{\varepsilon}^{s} \left.\frac{\mathrm{d}W_{\mathrm{rad}}}{\mathrm{d}\varepsilon}\right|_{\tilde{\varepsilon}\to\tilde{\varepsilon}-\varepsilon} &= \tilde{\nu} \int_{\varepsilon}^{\infty} \mathrm{d}\tilde{\varepsilon}\, \tilde{\varepsilon}^{s} \frac{1}{\tilde{\varepsilon}^{4/3}} \frac{1+(1-\eta)^2}{(1-\eta)^{1/3}\eta^{2/3}} \\ &= \tilde{\nu}\, \varepsilon^{s-1/3} \int_0^1 \mathrm{d}\eta\, \frac{1}{\eta^{s+4/3}} \frac{1+(1-\eta)^2}{(1-\eta)^{1/3}} \propto \varepsilon^{s-1/3}.\end{aligned} \tag{A.3.4}$$

A.3.2 Multiplying a power-law distribution function with the total QED rates

Besides, it is important to understand that each multiplication with a QED rate reduces the power-law index by $1/3$. In order to show that, one starts with the definition of W_{rad},

$$W_{\mathrm{rad}}(\varepsilon) = \int_0^{\varepsilon} \mathrm{d}\tilde{\varepsilon}\, \left.\frac{\mathrm{d}W_{\mathrm{rad}}}{\mathrm{d}\varepsilon}\right|_{\varepsilon\to\tilde{\varepsilon}}. \tag{A.3.5}$$

Note the permuted order of the subscript in the differential photon emission rate. This follows from the fact that one needs to sum over all final electron energies $\tilde{\varepsilon}$ that can be generated by the initial electron with energy ε to obtain the total photon emission rate. Inserting subsequently equation (6.1.4) and performing the same steps as above, one arrives at

$$W_{\mathrm{rad}}(\varepsilon) = \tilde{\nu}\, \varepsilon^{-1/3} \underbrace{\int_0^1 \mathrm{d}\eta\, \frac{1+\eta^2}{\eta^{1/3}(1-\eta)^{2/3}}}_{\approx 5.64} \propto \varepsilon^{-1/3}. \tag{A.3.6}$$

Correspondingly, each multiplication by W_{rad} reduces the power-law index by $1/3$. As a side note, one obtains exactly the limit $\chi \gg 1$ of W_{rad} [see equation (2.5.7)] when inserting $\tilde{\nu}$.
In analogy, one has

$$W_{\mathrm{pair}}(\varepsilon) = \int_0^{\varepsilon} \mathrm{d}\tilde{\varepsilon}\, \left.\frac{\mathrm{d}W_{\mathrm{pair}}}{\mathrm{d}\varepsilon}\right|_{\varepsilon\to\tilde{\varepsilon}} = \tilde{\nu}\, \varepsilon^{-1/3} \underbrace{\int_0^1 \mathrm{d}\eta\, \frac{\eta^2+(1-\eta)^2}{\eta^{1/3}(1-\eta)^{1/3}}}_{\approx 1.47} \propto \varepsilon^{-1/3}, \tag{A.3.7}$$

which is also in agreement with equation (2.5.12).

In conclusion, it is shown that the interaction transforms a power-law function ε^{s} into a new power-law function $\varepsilon^{s-1/3}$.

Bibliography

[1] A Einstein, *Strahlungsemission und Absorption nach der Quantentheorie*, Verhandlungen der Deutschen Physikalischen Gesellschaft **18**, 318–323 (1916).

[2] T H Maiman, *Stimulated Optical Radiation in Ruby*, Nature **187**, 493–494 (1960).

[3] M H Anderson, J R Ensher, M R Matthews, C E Wieman, and E A Cornell, *Observation of Bose-Einstein Condensation in a Dilute Atomic Vapor*, Science **269**, 198–201 (1995).

[4] K B Davis, M-O Mewes, M R Andrews, N J van Druten, D S Durfee, D M Kurn, and W Ketterle, *Bose-Einstein Condensation in a Gas of Sodium Atoms*, Physical Review Letters **75**, 3969–3973 (1995).

[5] B P Abbott *et al.* (LIGO Scientific Collaboration and Virgo Collaboration), *Observation of Gravitational Waves from a Binary Black Hole Merger*, Physical Review Letters **116**, 061102 (2016).

[6] W Kaiser and C G B Garrett, *Two-Photon Excitation in Ca*F_2*:* Eu^{2+}, Physical Review Letters **7**, 229–231 (1961).

[7] G S Voronov and N B Delone, *Many-photon ionization of the xenon atom by ruby laser radiation*, Soviet Physics JETP **23**, 54–58 (1966).

[8] P Agostini, F Fabre, G Mainfray, G Petite, and N K Rahman, *Free-Free Transitions Following Six-Photon Ionization of Xenon Atoms*, Physical Review Letters **42**, 1127–1130 (1979).

[9] D Strickland and G Mourou, *Compression of amplified chirped optical pulses*, Optics Communications **55**, 447–449 (1985).

[10] T Tajima and J M Dawson, *Laser Electron Accelerator*, Physical Review Letters **43**, 267–270 (1979).

[11] J Faure, Y Glinec, A Pukhov, S Kiselev, S Gordienko, E Lefebvre, J-P Rousseau, F Burgy, and V Malka, *A laser–plasma accelerator producing monoenergetic electron beams*, Nature **431**, 541 (2004).

[12] A J Gonsalves, K Nakamura, J Daniels, C Benedetti, C Pieronek, T C H de Raadt, S Steinke, J H Bin, S S Bulanov, J van Tilborg, *et al.*, *Petawatt Laser Guiding and Electron Beam Acceleration to 8 GeV in a Laser-Heated Capillary Discharge Waveguide*, Physical Review Letters **122**, 084801 (2019).

[13] C Thaury and F Quéré, *High-order harmonic and attosecond pulse generation on plasma mirrors: basic mechanisms*, Journal of Physics B: Atomic, Molecular and Optical Physics **43**, 213001 (2010).

[14] P B Corkum and F Krausz, *Attosecond science*, Nature Physics **3**, 381 (2007).

[15] V Yanovsky, V Chvykov, G Kalinchenko, P Rousseau, T Planchon, T Matsuoka, A Maksimchuk, J Nees, G Cheriaux, G Mourou, *et al.*, *Ultra-high intensity-300-TW laser at 0.1 Hz repetition rate*, Optics Express **16**, 2109–2114 (2008).

[16] C Danson, D Hillier, N Hopps, and D Neely, *Petawatt class lasers worldwide*, High Power Laser Science and Engineering **3**, e3 (2015).

[17] J D Jackson, *Classical Electrodynamics* (John Wiley & Sons, 1999).

[18] L D Landau and E M Lifschitz, *The Classical Theory of Fields* (Pergamon Press, New York, 1971).

[19] J M Cole, K T Behm, E Gerstmayr, T G Blackburn, J C Wood, C D Baird, M J Duff, C Harvey, A Ilderton, A S Joglekar, *et al.*, *Experimental Evidence of Radiation Reaction in the Collision of a High-Intensity Laser Pulse with a Laser-Wakefield Accelerated Electron Beam*, Physical Review X **8**, 011020 (2018).

[20] K Poder, M Tamburini, G Sarri, A Di Piazza, S Kuschel, C D Baird, K Behm, S Bohlen, J M Cole, D J Corvan, *et al.*, *Experimental Signatures of the Quantum Nature of Radiation Reaction in the Field of an Ultraintense Laser*, Physical Review X **8**, 031004 (2018).

[21] Extreme Light Infrastructure Project, https://eli-laser.eu.

[22] C Hernandez-Gomez, S P Blake, O Chekhlov, R J Clarke, A M Dunne, M Galimberti, S Hancock, R Heathcote, P Holligan, A Lyachev, *et al.*, *The Vulcan 10 PW project*, Journal of Physics: Conference Series **244**, 032006 (2010).

[23] Exawatt Center for Extreme Light Studies, https://xcels.iapras.ru.

[24] N V Elkina, A M Fedotov, I Yu Kostyukov, M V Legkov, N B Narozhny, E N Nerush, and H Ruhl, *QED cascades induced by circularly polarized laser fields*, Physical Review Special Topics-Accelerators and Beams **14**, 054401 (2011).

[25] W L Kruer, *The Physics of Laser Plasma Interactions* (CRC Press, Boca Raton, 2003).

[26] K H Spatschek, *High Temperature Plasmas: Theory and Mathematical Tools for Laser and Fusion Plasmas* (Wiley-VCH Verlag, Weinheim, Germany, 2012).

[27] A Pukhov, *Strong field interaction of laser radiation*, Reports on Progress in Physics **66**, 47 (2002).

[28] B Quesnel and P Mora, *Theory and simulation of the interaction of ultraintense laser pulses with electrons in vacuum*, Physical Review E **58**, 3719 (1998).

[29] J Schwinger, *On the Classical Radiation of Accelerated Electrons*, Physical Review **75**, 1912 (1949).

[30] A Di Piazza, C Müller, K Z Hatsagortsyan, and C H Keitel, *Extremely high-intensity laser interactions with fundamental quantum systems*, Reviews of Modern Physics **84**, 1177 (2012).

[31] N B Narozhny and A M Fedotov, *Extreme light physics*, Contemporary Physics **56**, 249–268 (2015).

[32] F Sauter, *Über das Verhalten eines Elektrons im homogenen elektrischen Feld nach der relativistischen Theorie Diracs*, Zeitschrift für Physik **69**, 742–764 (1931).

[33] W Heisenberg and H Euler, *Folgerungen aus der Diracschen Theorie des Positrons*, Zeitschrift für Physik **98**, 714–732 (1936).

[34] J Schwinger, *On Gauge Invariance and Vacuum Polarization*, Physical Review **82**, 664 (1951).

[35] V I Ritus, *Quantum effects of the interaction of elementary particles with an intense electromagnetic field*, Journal of Soviet Laser Research **6**, 497–617 (1985).

[36] V N Baier, V M Katkov, and V M Strakhovenko, *Quantum radiation theory in inhomogeneous external fields*, Nuclear Physics B **328**, 387–405 (1989).

[37] A I Nikishov and V I Ritus, *Quantum processes in the field of a plane electromagnetic wave and in a constant field. I*, Soviet Physics JETP **19**, 529 (1964).

[38] T Erber, *High-Energy Electromagnetic Conversion Processes in Intense Magnetic Fields*, Reviews of Modern Physics **38**, 626–659 (1966).

[39] V N Baier, V M Katkov, and V M Strakhovenko, *Electromagnetic Processes at High Energies in Oriented Single Crystals* (World Scientific, 1998).

[40] A I Nikishov and V I Ritus, *Pair Production by a Photon and Photon Emission by an Electron in the Field of an Intense Electromagnetic Wave and in a Constant Field*, Soviet Physics JETP **25**, 1135 (1967).

[41] G Breit and J A Wheeler, *Collision of Two Light Quanta*, Physical Review **46**, 1087 (1934).

[42] H Ruhl and P Mulser, *Relativistic Vlasov simulation of intense fs laser pulse-matter interaction*, Physics Letters A **205**, 388–392 (1995).

[43] E Sonnendrücker, J Roche, P Bertrand, and A Ghizzo, *The Semi-Lagrangian Method for the Numerical Resolution of the Vlasov Equation*, Journal of Computational Physics **149**, 201–220 (1999).

[44] A Mangeney, F Califano, C Cavazzoni, and P Travnicek, *A Numerical Scheme for the Integration of the Vlasov–Maxwell System of Equations*, Journal of Computational Physics **179**, 495–538 (2002).

[45] G Lehmann, *Efficient Semi-Lagrangian Vlasov-Maxwell Simulations of High Order Harmonic Generation from Relativistic Laser-Plasma Interactions*, Communications in Computational Physics **20**, 583–602 (2016).

[46] O Buneman, *Dissipation of Currents in Ionized Media*, Physical Review **115**, 503–517 (1959).

[47] J Dawson, *One-Dimensional Plasma Model*, The Physics of Fluids **5**, 445–459 (1962).

[48] R W Hockney and J W Eastwood, *Computer Simulation Using Particles* (CRC Press, Boca Raton, 1988).

[49] C K Birdsall and A B Langdon, *Plasma Physics Via Computer Simulation* (CRC Press, Boca Raton, 1991).

[50] K Yee, *Numerical solution of initial boundary value problems involving Maxwell's equations in isotropic media*, IEEE Transactions on Antennas and Propagation **14**, 302–307 (1966).

[51] J-L Vay, I Haber, and B B Godfrey, *A domain decomposition method for pseudo-spectral electromagnetic simulations of plasmas*, Journal of Computational Physics **243**, 260–268 (2013).

[52] A Pukhov, *Three-dimensional electromagnetic relativistic particle-in-cell code VLPL (Virtual Laser Plasma Lab)*, Journal of Plasma Physics **61**, 425–433 (1999).

[53] A Pukhov, *X-dispersionless Maxwell solver for plasma-based particle acceleration*, Journal of Computational Physics **418**, 109622 (2020).

[54] A Pukhov, *Particle-In-Cell Codes for Plasma-based Particle Acceleration*, CERN Yellow Reports **1**, 181 (2016).

[55] R A Fonseca, L O Silva, F S Tsung, V K Decyk, W Lu, C Ren, W B Mori, S Deng, S Lee, T Katsouleas, *et al.*, *OSIRIS: A Three-Dimensional, Fully Relativistic Particle in Cell Code for Modeling Plasma Based Accelerators,* in International Conference on Computational Science (Springer, Berlin, Germany, 2002) pp. 342–351.

[56] C Nieter and J R Cary, *VORPAL: a versatile plasma simulation code*, Journal of Computational Physics **196**, 448–473 (2004).

[57] S Bastrakov, R Donchenko, A Gonoskov, E Efimenko, A Malyshev, I Meyerov, and I Surmin, *Particle-in-cell plasma simulation on heterogeneous cluster systems*, Journal of Computational Science **3**, 474–479 (2012).

[58] T D Arber, K Bennett, C S Brady, A Lawrence-Douglas, M G Ramsay, N J Sircombe, P Gillies, R G Evans, H Schmitz, A R Bell, and C P Ridgers, *Contemporary particle-in-cell approach to laser-plasma modelling*, Plasma Physics and Controlled Fusion **57**, 113001 (2015).

[59] J Derouillat, A Beck, F Pérez, T Vinci, M Chiaramello, A Grassi, M Flé, G Bouchard, I Plotnikov, N Aunai, *et al.*, *SMILEI: A collaborative, open-source, multi-purpose particle-in-cell code for plasma simulation*, Computer Physics Communications **222**, 351–373 (2018).

[60] J P Boris, *Relativistic plasma simulation-optimization of a hybrid code,* in Proceedings of the 4th Conference on Numerical Simulation of Plasmas (Naval Research Laboratory, Washington, D.C., 1970) pp. 3–67.

[61] J-L Vay, *Simulation of beams or plasmas crossing at relativistic velocity*, Physics of Plasmas **15**, 056701 (2008).

[62] R Courant, K Friedrichs, and H Lewy, *On the Partial Difference Equations of Mathematical Physics*, IBM Journal of Research and Development **11**, 215–234 (1967).

[63] A Gonoskov, S Bastrakov, E Efimenko, A Ilderton, M Marklund, I Meyerov, A Muraviev, A Sergeev, I Surmin, and E Wallin, *Extended particle-in-cell schemes for physics in ultrastrong laser fields: Review and developments*, Physical Review E **92**, 023305 (2015).

[64] P A M Dirac, *Classical theory of radiating electrons*, Proceedings of the Royal Society A: Mathematical, Physical and Engineering Sciences **167**, 148–169 (1938).

[65] M Vranic, J L Martins, R A Fonseca, and L O Silva, *Classical radiation reaction in particle-in-cell simulations*, Computer Physics Communications **204**, 141–151 (2016).

[66] I V Sokolov, N M Naumova, J A Nees, G A Mourou, and V P Yanovsky, *Dynamics of emitting electrons in strong laser fields*, Physics of Plasmas **16**, 093115 (2009).

[67] M Tamburini, F Pegoraro, A Di Piazza, C H Keitel, and A Macchi, *Radiation reaction effects on radiation pressure acceleration*, New Journal of Physics **12**, 123005 (2010).

[68] M Tamburini, T V Liseykina, F Pegoraro, and A Macchi, *Radiation-pressure-dominant acceleration: Polarization and radiation reaction effects and energy increase in three-dimensional simulations*, Physical Review E **85**, 016407 (2012).

[69] T Schlegel and V T Tikhonchuk, *Classical radiation effects on relativistic electrons in ultraintense laser fields with circular polarization*, New Journal of Physics **14**, 073034 (2012).

[70] R Capdessus, E d'Humières, and V T Tikhonchuk, *Modeling of radiation losses in ultra-high power laser-matter interaction*, Physical Review E **86**, 036401 (2012).

[71] D Wu, B Qiao, and X T He, *The radiation reaction effects in the ultra-intense and ultra-short laser foil interaction regime*, Physics of Plasmas **22**, 093108 (2015).

[72] M Chen, A Pukhov, T-P Yu, and Z-M Sheng, *Radiation reaction effects on ion acceleration in laser foil interaction*, Plasma Physics and Controlled Fusion **53**, 014004 (2010).

[73] T G Blackburn, C P Ridgers, J G Kirk, and A R Bell, *Quantum Radiation Reaction in Laser–Electron-Beam Collisions*, Physical Review Letters **112**, 015001 (2014).

[74] E N Nerush, I Yu Kostyukov, A M Fedotov, N B Narozhny, N V Elkina, and H Ruhl, *Laser field absorption in self-generated electron-positron pair plasma*, Physical Review Letters **106**, 035001 (2011).

[75] Z Lécz and A Andreev, *Minimum requirements for electron–positron pair creation in the interaction of ultra-short laser pulses with thin foils*, Plasma Physics and Controlled Fusion **61**, 045005 (2019).

[76] R Duclous, J G Kirk, and A R Bell, *Monte Carlo calculations of pair production in high-intensity laser–plasma interactions*, Plasma Physics and Controlled Fusion **53**, 015009 (2010).

[77] I Yu Kostyukov, E N Nerush, and V F Bashmakov, *QED effects and radiation generation in relativistic laser plasma*, Proceedings of SPIE **8075**, 807504 (2011).

[78] C Baumann and A Pukhov, *Influence of e^-e^+ creation on the radiative trapping in ultraintense fields of colliding laser pulses*, Physical Review E **94**, 063204 (2016).

[79] V Anguelov and H Vankov, *Electromagnetic showers in a strong magnetic field*, Journal of Physics G: Nuclear and Particle Physics **25**, 1755 (1999).

[80] A A Mironov, A M Fedotov, and N B Narozhny, *Generation of quantum-electrodynamic cascades in oblique collisions of ultrarelativistic electrons with an intense laser field*, Quantum Electronics **46**, 305 (2016).

[81] P Zhang, C P Ridgers, and A G R Thomas, *The effect of nonlinear quantum electrodynamics on relativistic transparency and laser absorption in ultra-relativistic plasmas*, New Journal of Physics **17**, 043051 (2015).

[82] M Vranic, T Grismayer, R A Fonseca, and L O Silva, *Electron–positron cascades in multiple-laser optical traps*, Plasma Physics and Controlled Fusion **59**, 014040 (2016).

[83] Z Gong, R H Hu, Y R Shou, B Qiao, C E Chen, X T He, S S Bulanov, T Zh Esirkepov, S V Bulanov, and X Q Yan, *High-efficiency γ-ray flash generation via multiple-laser scattering in ponderomotive potential well*, Physical Review E **95**, 013210 (2017).

[84] A R Bell and J G Kirk, *Possibility of Prolific Pair Production with High-Power Lasers*, Physical Review Letters **101**, 200403 (2008).

[85] T Grismayer, M Vranic, J L Martins, R A Fonseca, and L O Silva, *Seeded QED cascades in counterpropagating laser pulses*, Physical Review E **95**, 023210 (2017).

[86] T Grismayer, M Vranic, J L Martins, R A Fonseca, and L O Silva, *Laser absorption via quantum electrodynamics cascades in counter propagating laser pulses*, Physics of Plasmas **23**, 056706 (2016).

[87] S S Bulanov, V D Mur, N B Narozhny, J Nees, and V S Popov, *Multiple Colliding Electromagnetic Pulses: A Way to Lower the Threshold of e^+e^- Pair Production from Vacuum*, Physical Review Letters **104**, 220404 (2010).

[88] L L Ji, A Pukhov, I Yu Kostyukov, B F Shen, and K Akli, *Radiation-Reaction Trapping of Electrons in Extreme Laser Fields*, Physical Review Letters **112**, 145003 (2014).

[89] A M Fedotov, N V Elkina, E G Gelfer, N B Narozhny, and H Ruhl, *Radiation friction versus ponderomotive effect*, Physical Review A **90**, 053847 (2014).

[90] J G Kirk, A R Bell, and I Arka, *Pair production in counter-propagating laser beams*, Plasma Physics and Controlled Fusion **51**, 085008 (2009).

[91] W Y Liu, W Luo, T Yuan, J Y Yu, M Chen, and Z M Sheng, *Enhanced pair plasma generation in the relativistic transparency regime*, Physics of Plasmas **24**, 103130 (2017).

[92] M Jirka, O Klimo, S V Bulanov, T Zh Esirkepov, E Gelfer, S S Bulanov, S Weber, and G Korn, *Electron dynamics and γ and e^-e^+ production by colliding laser pulses*, Physical Review E **93**, 023207 (2016).

[93] A Gonoskov, A Bashinov, I Gonoskov, C Harvey, A Ilderton, A Kim, M Marklund, G Mourou, and A Sergeev, *Anomalous Radiative Trapping in Laser Fields of Extreme Intensity*, Physical Review Letters **113**, 014801 (2014).

[94] A V Bashinov, P Kumar, and A V Kim, *Particle dynamics and spatial e^-e^+ density structures at QED cascading in circularly polarized standing waves*, Physical Review A **95**, 042127 (2017).

[95] G Lehmann and K H Spatschek, *Phase-space contraction and attractors for ultrarelativistic electrons*, Physical Review E **85**, 056412 (2012).

[96] J G Kirk, *Radiative trapping in intense laser beams*, Plasma Physics and Controlled Fusion **58**, 085005 (2016).

[97] A Gonoskov and M Marklund, *Radiation-dominated particle and plasma dynamics*, Physics of Plasmas **25**, 093109 (2018).

[98] S Augst, D D Meyerhofer, D Strickland, and S L Chin, *Laser ionization of noble gases by Coulomb-barrier suppression*, Journal of the Optical Society of America B **8**, 858–867 (1991).

[99] L Allen, M W Beijersbergen, R J C Spreeuw, and J P Woerdman, *Orbital angular momentum of light and the transformation of Laguerre-Gaussian laser modes*, Physical Review A **45**, 8185 (1992).

[100] A Jesacher, S Fürhapter, S Bernet, and M Ritsch-Marte, *Shadow Effects in Spiral Phase Contrast Microscopy*, Physical Review Letters **94**, 233902 (2005).

[101] C Maurer, A Jesacher, S Bernet, and M Ritsch-Marte, *What spatial light modulators can do for optical microscopy*, Laser & Photonics Reviews **5**, 81–101 (2011).

[102] H He, M E J Friese, N R Heckenberg, and H Rubinsztein-Dunlop, *Direct Observation of Transfer of Angular Momentum to Absorptive Particles from a Laser Beam with a Phase Singularity*, Physical Review Letters **75**, 826 (1995).

[103] D G Grier, *A revolution in optical manipulation*, Nature **424**, 810 (2003).

[104] A Mair, A Vaziri, G Weihs, and A Zeilinger, *Entanglement of the orbital angular momentum states of photons*, Nature **412**, 313 (2001).

[105] G Molina-Terriza, A Vaziri, J Řeháček, Z Hradil, and A Zeilinger, *Triggered Qutrits for Quantum Communication Protocols*, Physical Review Letters **92**, 167903 (2004).

[106] J P Torres and L Torner, *Twisted Photons: Applications of Light with Orbital Angular Momentum* (Wiley-VCH Verlag, Weinheim, Germany, 2011).

[107] J Vieira, R M G M Trines, E P Alves, R A Fonseca, J T Mendonça, R Bingham, P Norreys, and L O Silva, *Amplification and generation of ultra-intense twisted laser pulses via stimulated Raman scattering*, Nature Communications **7**, 10371 (2016).

[108] Y Shi, B Shen, L Zhang, X Zhang, W Wang, and Z Xu, *Light Fan Driven by a Relativistic Laser Pulse*, Physical Review Letters **112**, 235001 (2014).

[109] A Leblanc, A Denoeud, L Chopineau, G Mennerat, P Martin, and F Quéré, *Plasma holograms for ultrahigh-intensity optics*, Nature Physics **13**, 440 (2017).

[110] G Lehmann and K H Spatschek, *Plasma volume holograms for focusing and mode conversion of ultraintense laser pulses*, Physical Review E **100**, 033205 (2019).

[111] C Brabetz, S Busold, T Cowan, O Deppert, D Jahn, O Kester, M Roth, D Schumacher, and V Bagnoud, *Laser-driven ion acceleration with hollow laser beams*, Physics of Plasmas **22**, 013105 (2015).

[112] A Denoeud, L Chopineau, A Leblanc, and F Quéré, *Interaction of Ultraintense Laser Vortices with Plasma Mirrors*, Physical Review Letters **118**, 033902 (2017).

[113] J T Mendonça and J Vieira, *Donut wakefields generated by intense laser pulses with orbital angular momentum*, Physics of Plasmas **21**, 033107 (2014).

[114] G-B Zhang, M Chen, C B Schroeder, J Luo, M Zeng, F-Y Li, L-L Yu, S-M Weng, Y-Y Ma, T-P Yu, *et al.*, *Acceleration and evolution of a hollow electron beam in wakefields driven by a Laguerre-Gaussian laser pulse*, Physics of Plasmas **23**, 033114 (2016).

[115] G-B Zhang, M Chen, J Luo, M Zeng, T Yuan, J-Y Yu, Y-Y Ma, T-P Yu, L-L Yu, S-M Weng, *et al.*, *Acceleration of on-axis and ring-shaped electron beams in wakefields driven by Laguerre-Gaussian pulses*, Journal of Applied Physics **119**, 103101 (2016).

[116] H Saberi, J Vieira, and L O Silva, *Ponderomotive beatwave ion acceleration using twisted light*, Physics of Plasmas **24**, 103131 (2017).

[117] J Vieira and J T Mendonça, *Nonlinear Laser Driven Donut Wakefields for Positron and Electron Acceleration*, Physical Review Letters **112**, 215001 (2014).

[118] J T Mendonça and J Vieira, *High harmonic generation in underdense plasmas by intense laser pulses with orbital angular momentum*, Physics of Plasmas **22**, 123106 (2015).

[119] X Zhang, B Shen, Y Shi, X Wang, L Zhang, W Wang, J Xu, L Yi, and Z Xu, *Generation of Intense High-Order Vortex Harmonics*, Physical Review Letters **114**, 173901 (2015).

[120] J Vieira, R M G M Trines, E P Alves, R A Fonseca, J T Mendonça, R Bingham, P Norreys, and L O Silva, *High Orbital Angular Momentum Harmonic Generation*, Physical Review Letters **117**, 265001 (2016).

[121] Y Wu, L L Ji, X Geng, Q Yu, N Wang, B Feng, Z Guo, W Wang, C Qin, X Yan, *et al.*, *Polarized electron-beam acceleration driven by vortex laser pulses*, New Journal of Physics **21**, 073052 (2019).

[122] C Liu, B Shen, X Zhang, Y Shi, L Ji, W Wang, L Yi, L Zhang, T Xu, Z Pei, and Z Xu, *Generation of gamma-ray beam with orbital angular momentum in the QED regime*, Physics of Plasmas **23**, 093120 (2016).

[123] Y-Y Chen, J-X Li, K Z Hatsagortsyan, and C H Keitel, *γ-Ray Beams with Large Orbital Angular Momentum via Nonlinear Compton Scattering with Radiation Reaction*, Physical Review Letters **121**, 074801 (2018).

[124] X-L Zhu, M Chen, T-P Yu, S-M Weng, L-X Hu, P McKenna, and Z-M Sheng, *Bright attosecond γ-ray pulses from nonlinear Compton scattering with laser-illuminated compound targets*, Applied Physics Letters **112**, 174102 (2018).

[125] Y-Y Chen, K Z Hatsagortsyan, and C H Keitel, *Generation of twisted γ-ray radiation by nonlinear Thomson scattering of twisted light*, Matter and Radiation at Extremes **4**, 024401 (2019).

[126] L B Ju, C T Zhou, T W Huang, K Jiang, C N Wu, T Y Long, L Li, H Zhang, M Y Yu, and S C Ruan, *Generation of Collimated Bright Gamma Rays with Controllable Angular Momentum Using Intense Laguerre-Gaussian Laser Pulses*, Physical Review Applied **12**, 014054 (2019).

[127] P F Goldsmith, *Quasioptical Systems: Gaussian Beam Quasioptical Propagation and Applications* (IEEE Press, New York, 1998) p. 26 ff.

[128] N B Simpson, K Dholakia, L Allen, and M J Padgett, *Mechanical equivalence of spin and orbital angular momentum of light: an optical spanner*, Optics Letters **22**, 52–54 (1997).

[129] C Baumann and A M Pukhov, *Generation of attosecond electron packets in the interaction of ultraintense Laguerre–Gaussian laser beams with plasma*, Quantum Electronics **47**, 194 (2017).

[130] C Baumann and A Pukhov, *Electron dynamics in twisted light modes of relativistic intensity*, Physics of Plasmas **25**, 083114 (2018).

[131] L-X Hu, T-P Yu, Z-M Sheng, J Vieira, D-B Zou, Y Yin, P McKenna, and F-Q Shao, *Attosecond electron bunches from a nanofiber driven by Laguerre-Gaussian laser pulses*, Scientific Reports **8**, 7282 (2018).

[132] L-X Hu, T-P Yu, Y Lu, G-B Zhang, D-B Zou, H Zhang, Z-Y Ge, Y Yin, and F-Q Shao, *Dynamics of the interaction of relativistic Laguerre–Gaussian laser pulses with a wire target*, Plasma Physics and Controlled Fusion **61**, 025009 (2019).

[133] L-X Hu, T-P Yu, H-Z Li, Y Yin, P McKenna, and F Shao, *Dense relativistic electron mirrors from a Laguerre-Gaussian laser-irradiated micro-droplet*, Optics Letters **43**, 2615–2618 (2018).

[134] L B Ju, C T Zhou, K Jiang, T W Huang, H Zhang, T X Cai, J M Cao, B Qiao, and S C Ruan, *Manipulating the topological structure of ultrarelativistic electron beams using Laguerre–Gaussian laser pulse*, New Journal of Physics **20**, 063004 (2018).

[135] J X Wang, Y K Ho, Q Kong, L J Zhu, L Feng, S Scheid, and H Hora, *Electron capture and violent acceleration by an extra-intense laser beam*, Physical Review E **58**, 6575 (1998).

[136] J Pang, Y K Ho, X Q Yuan, N Cao, Q Kong, P X Wang, L Shao, E H Esarey, and A M Sessler, *Subluminous phase velocity of a focused laser beam and vacuum laser acceleration*, Physical Review E **66**, 066501 (2002).

[137] C Bula, K T McDonald, E J Prebys, C Bamber, S Boege, T Kotseroglou, A C Melissinos, D D Meyerhofer, W Ragg, D L Burke, *et al.*, *Observation of Nonlinear Effects in Compton Scattering*, Physical Review Letters **76**, 3116 (1996).

[138] D L Burke, R C Field, G Horton-Smith, J E Spencer, D Walz, S C Berridge, W M Bugg, K Shmakov, A W Weidemann, C Bula, *et al.*, *Positron Production in Multiphoton Light-by-Light Scattering*, Physical Review Letters **79**, 1626 (1997).

[139] T N Wistisen, A Di Piazza, H V Knudsen, and U I Uggerhøj, *Experimental evidence of quantum radiation reaction in aligned crystals*, Nature Communications **9**, 795 (2018).

[140] T N Wistisen, A Di Piazza, C F Nielsen, A H Sørensen, and U I Uggerhøj (CERN NA63), *Quantum radiation reaction in aligned crystals beyond the local constant field approximation*, Physical Review Research **1**, 033014 (2019).

[141] K Kirsebom, U Mikkelsen, E Uggerhøj, K Elsener, S Ballestrero, P Sona, and Z Z Vilakazi, *First Measurements of the Unique Influence of Spin on the Energy Loss of Ultrarelativistic Electrons in Strong Electromagnetic Fields*, Physical Review Letters **87**, 054801 (2001).

[142] A K Harding and D Lai, *Physics of strongly magnetized neutron stars*, Reports on Progress in Physics **69**, 2631 (2006).

[143] D A Uzdensky and S Rightley, *Plasma physics of extreme astrophysical environments*, Reports on Progress in Physics **77**, 036902 (2014).

[144] N B Narozhny, *Propagation of Plane Electromagnetic Waves in a Constant Field*, Soviet Physics JETP **28**, 371 (1969).

[145] V I Ritus, *Radiative Effects and Their Enhancement in an Intense Electromagnetic Field*, Soviet Physics JETP **30**, 1181 (1970).

[146] V I Ritus, *Radiative corrections in quantum electrodynamics with intense field and their analytical properties*, Annals of Physics **69**, 555–582 (1972).

[147] N B Narozhny, *Expansion parameter of perturbation theory in intense-field quantum electrodynamics*, Physical Review D **21**, 1176 (1980).

[148] A M Fedotov, *Conjecture of perturbative QED breakdown at $\alpha\chi^{2/3} \gtrsim 1$*, Journal of Physics: Conference Series **826**, 012027 (2017).

[149] T Podszus and A Di Piazza, *High-energy behavior of strong-field QED in an intense plane wave*, Physical Review D **99**, 076004 (2019).

[150] A Ilderton, *Note on the conjectured breakdown of QED perturbation theory in strong fields*, Physical Review D **99**, 085002 (2019).

[151] I Blumenfeld, C E Clayton, F-J Decker, M J Hogan, C Huang, R Ischebeck, R Iverson, C Joshi, T Katsouleas, N Kirby, *et al.*, *Energy doubling of 42 GeV electrons in a metre-scale plasma wakefield accelerator*, Nature **445**, 741 (2007).

[152] H4 beam line at the Super-Proton-Synchrotron North Area facility at CERN, https://cern.ch/sba.

[153] H Baer, T Barklow, K Fujii, Y Gao, A Hoang, S Kanemura, J List, H E Logan, A Nomerotski, M Perelstein, *et al.*, *The International Linear Collider Technical Design Report - Volume 2: Physics*, preprint arXiv:1306.6352 (2013).

[154] V Yakimenko, S Meuren, F Del Gaudio, C Baumann, A Fedotov, F Fiuza, T Grismayer, M J Hogan, A Pukhov, L O Silva, and G White, *Prospect of Studying Nonperturbative QED with Beam-Beam Collisions*, Physical Review Letters **122**, 190404 (2019).

[155] F Del Gaudio, T Grismayer, RA Fonseca, W B Mori, and L O Silva, *Bright γ rays source and nonlinear Breit-Wheeler pairs in the collision of high density particle beams*, Physical Review Accelerators and Beams **22**, 023402 (2019).

[156] A W Chao, *A summary of some beam-beam models*, AIP Conference Proceedings **57**, 42–68 (1980).

[157] R Hollebeek, *Disruption limits for linear colliders*, Nuclear Instruments and Methods **184**, 333–347 (1981).

[158] M Aicheler, P Burrows, M Draper, T Garvey, P Lebrun, K Peach, N Phinney, H Schmickler, D Schulte, and N Toge, *A Multi-TeV Linear Collider Based on CLIC Technology: CLIC Conceptual Design Report*, CERN Yellow Reports: Monographs (CERN, Geneva, 2012).

[159] P Chen, G Horton-Smith, T Ohgaki, A W Weidemann, and K Yokoya, *CAIN: Conglomerat d'ABEL et d'Interactions Non-lineaires*, Nuclear Instruments and Methods in Physics Research Section A: Accelerators, Spectrometers, Detectors and Associated Equipment **355**, 107–110 (1995).

[160] D Schulte, *Beam-Beam Simulations with GUINEA-PIG*, CERN-PS-99-014-LP (1999).

[161] K Yokoya and P Chen, *Beam-beam phenomena in linear colliders,* in Frontiers of Particle Beams: Intensity Limitations (Springer, Berlin, Germany, 1992) pp. 415–445.

[162] P Chen and V I Telnov, *Coherent Pair Creation in Linear Colliders*, Physical Review Letters **63**, 1796 (1989).

[163] C Baumann, E N Nerush, A Pukhov, and I Yu Kostyukov, *Probing non-perturbative QED with electron-laser collisions*, Scientific Reports **9**, 9407 (2019).

[164] D an der Brügge and A Pukhov, *Enhanced relativistic harmonics by electron nanobunching*, Physics of Plasmas **17**, 033110 (2010).

[165] A A Gonoskov, A V Korzhimanov, A V Kim, M Marklund, and A M Sergeev, *Ultrarelativistic nanoplasmonics as a route towards extreme-intensity attosecond pulses*, Physical Review E **84**, 046403 (2011).

[166] H Vincenti and F Quéré, *Attosecond Lighthouses: How To Use Spatiotemporally Coupled Light Fields To Generate Isolated Attosecond Pulses*, Physical Review Letters **108**, 113904 (2012).

[167] C Rödel, D an der Brügge, J Bierbach, M Yeung, T Hahn, B Dromey, S Herzer, S Fuchs, A G Pour, E Eckner, *et al.*, *Harmonic Generation from Relativistic Plasma Surfaces in Ultrasteep Plasma Density Gradients*, Physical Review Letters **109**, 125002 (2012).

[168] E G Gamaliy and R Dragila, *Interaction of ultrashort laser pulses at relativistic intensities with solid targets: Relativistic skin effect*, Physical Review A **42**, 929 (1990).

[169] C Baumann and A Pukhov, *Laser-solid interaction and its potential for probing radiative corrections in strong-field quantum electrodynamics*, Plasma Physics and Controlled Fusion **61**, 074010 (2019).

[170] E N Nerush and I Yu Kostyukov, *Laser-driven hole boring and gamma-ray emission in high-density plasmas*, Plasma Physics and Controlled Fusion **57**, 035007 (2015).

[171] I Yu Kostyukov and E N Nerush, *Production and dynamics of positrons in ultrahigh intensity laser-foil interactions*, Physics of Plasmas **23**, 093119 (2016).

[172] D Del Sorbo, D R Blackman, R Capdessus, K Small, C Slade-Lowther, W Luo, M J Duff, A P L Robinson, P McKenna, Z M Sheng, *et al.*, *Efficient ion acceleration and dense electron–positron plasma creation in ultra-high intensity laser-solid interactions*, New Journal of Physics **20**, 033014 (2018).

[173] T Schlegel, N Naumova, V T Tikhonchuk, C Labaune, I V Sokolov, and G Mourou, *Relativistic laser piston model: Ponderomotive ion acceleration in dense plasmas using ultraintense laser pulses*, Physics of Plasmas **16**, 083103 (2009).

[174] T G Blackburn, A Ilderton, M Marklund, and C P Ridgers, *Reaching supercritical field strengths with intense lasers*, New Journal of Physics **21**, 053040 (2019).

[175] A Di Piazza, T N Wistisen, M Tamburini, and U I Uggerhøj, *Testing Strong Field QED Close to the Fully Nonperturbative Regime Using Aligned Crystals*, Physical Review Letters **124**, 044801 (2020).

[176] I I Artemenko, M S Krygin, D A Serebryakov, E N Nerush, and I Yu Kostyukov, *Global constant field approximation for radiation reaction in collision of high-intensity laser pulse with electron beam*, Plasma Physics and Controlled Fusion **61**, 074003 (2019).

[177] E N Nerush, V F Bashmakov, and I Yu Kostyukov, *Analytical model for electromagnetic cascades in rotating electric field*, Physics of Plasmas **18**, 083107 (2011).

[178] M Tamburini and S Meuren, *Efficient High-Energy Photon Production in the Supercritical QED Regime*, preprint arXiv:1912.07508 (2019).

Acknowledgments

Finishing this thesis would not have been possible without the support and advice by many people.

First and foremost, I would like to thank Professor Dr Alexander Pukhov for giving me the opportunity to perform my PhD studies in his group. I am particularly thankful for the freedom in pursuing my own research interests, and for the various international conferences that I was able to attend.

I am grateful to Professor Dr Dr Carsten Müller for his readiness to be the second reviewer of this thesis and for all his advice in various questions. On a daily basis, I really appreciate him as a loyal Mensa companion.

A special thank you is reserved for Frau Elvira Gröters and Frau Ute Birkenkamp-Pickshaus. Their support in organizing questions enabled me the focus on physical problems rather than losing my mind in university-internal bureaucracy.

Of course, Eugen Braun should not be missing in this list. Spasiba for keeping our cluster round the clock alive; even if it was sometimes short to collapse.

Furthermore, I want to express my thanks to Dr Vitaly Yakimenko, Dr Sebastian Meuren, Fabrizio Del Gaudio, Dr Alexander Fedotov, Dr Frederico Fiúza, Dr Thomas Grismayer, Dr Mark Hogan, Professor Dr Luís O. Silva, and Dr Glen White for letting me be a part in the non-perturbative QED collaboration. My expression of gratitude also includes Dr Evgeny Nerush and Professor Dr Igor Kostyukov. Thank you for in- and constructive discussions during our collaboration.

A big word of thanks is addressed to all current and former members of our institute. Only the friendly atmosphere and a lot of constructive discussions about physics made fruitful outcome possible. At this point, I want to mention explicitly Dr Vural Kaymak for a vast number of discussions and all the funny moments, e.g. at various conferences; Dr Phuc Tanh-Luu for assisting me in my setting-in period at the institute and for the broad introduction into our simulation code; Dr John Farmer for regularly bringing to mind to have fun at work; Dr Götz Lehmann and Dr Johannes Thomas for inspiring discussions; and Lars Reichwein for his ever helping kind and for proofreading my thesis.

I also acknowledge financial support from the Heinrich Heine University Düsseldorf in regard of the payment of article publication charges.

Last but not least, I am deeply grateful for all the support from my family during my studies.

Eidesstattliche Erklärung

Ich versichere an Eides Statt, dass die Dissertation von mir selbständig und ohne unzulässige fremde Hilfe unter Beachtung der „Grundsätze zur Sicherung guter wissenschaftlicher Praxis an der Heinrich-Heine-Universität Düsseldorf" erstellt worden ist.

Düsseldorf, den

Unterschrift